



Unsteady-State Operation of a Fixed-Bed Recycle Reactor for the Methanation of Carbon Dioxide

DISSERTATION

to obtain the academic degree of

DOCTOR OF ENGINEERING (DR.-ING.)

of the Faculty of Engineering, Computer Science and Psychology of
Ulm University

submitted by

Steffi Theurich née Matthischke

from Dresden

| | |
|-------------------|---|
| Reviewer: | Prof. Dr.-Ing. Robert Güttel Prof. Dr.-Ing. Thomas Turek |
| Officiating Dean: | Prof. Dr.-Ing. Maurits Ortmanns |

Ulm, 11. April 2019

Zusammenfassung

Als eine Möglichkeit der Stromspeicherung von erneuerbaren Energien werden Power-to-X Prozesse diskutiert. Sie bieten vielfältige Einsatzmöglichkeiten zur Langzeitspeicherung von elektrischem Strom und koppeln dabei die Stromerzeugung direkt mit Energie verbrauchenden Sektoren (Sektorkopplung). Anwendungsfälle sind zum Beispiel die Wärmebereitstellung (Power-to-Heat) oder die Nutzung in der chemischen Industrie durch die Bereitstellung von Wasserstoff über eine Wasserelektrolyse. Beim Power-to-Gas (PtG) Verfahren wird der elektrolytisch produzierte Wasserstoff mit Kohlenstoffdioxid bzw. -monoxid gemischt und anschließend katalytisch in Methan umgewandelt (Methanisierung). Methan kann aufgrund der etablierten Infrastruktur im Erdgasnetz gespeichert, zur Wärme- und Stromproduktion eingesetzt oder für Erdgasfahrzeuge genutzt werden.

Im ersten Prozessschritt des PtG-Verfahrens wird die Elektrolyse aufgrund der stark schwankenden Strombereitstellung durch Sonnen- und Windenergie dynamisch betrieben. Durch einen ebenfalls dynamischen Betrieb der Methanisierung können die Kosten der Wasserstoffspeicherung deutlich reduziert werden. Jedoch wurden die unter instationären Bedingungen auftretenden Phänomene und angepasste Betriebsstrategien bisher nicht ausreichend untersucht. Daher ist es das Ziel dieser Forschungsarbeit, den instationären Betrieb der exothermen Methansynthese am Beispiel eines Festbett-Kreislaufreaktors zu untersuchen. Mit dem Konzept der Produktrückführung wurde bisher versucht, den Reaktor zu kühlen. In dieser Arbeit soll auch überprüft werden, ob sich die Produktrückführung als Regelgröße eignet, da es sich dabei um eine physikalische Rückkopplungsschleife handelt. Zusätzlich sollen die Ergebnisse hinsichtlich Lastflexibilität, Reaktordesign sowie Betriebs- und Regelungsstrategien zusammengefasst werden.

Dafür wurden Simulationsexperimente auf Basis eines dynamischen Reaktormodells (mehrphasig, 1D) und physikalische Experimente an einem Syntheseversuchsstand durchgeführt. Für beide Methodiken erfolgte im ersten Schritt eine Systemcharakterisierung und Validierung auf Basis von Experimenten mit zeitlich konstanten Eintrittsparametern. Dabei wurden die Reaktorkühlung (adiabat oder gekühlt), die Eintrittsparameter des Prozesses und das Rezirkulationsverhältnis variiert. Im zweiten Schritt wurden instationäre Experimente mit verschiedenen Lastrampen für den Eintrittsvolumenstrom allerdings noch ohne Produktrückführung durchgeführt. Dadurch war eine Bestimmung des dynamischen Verhaltens in Abhängigkeit von der Laständerungsgeschwindigkeit möglich. Abschließend wurde das instationäre Verhalten des Festbettreaktors mit Produktrückführung untersucht

und geprüft inwieweit das dynamische Verhalten durch die Änderung des Rezirkulationsverhältnisses beeinflusst werden kann.

Zu den wichtigsten Detailergebnissen der Arbeit gehören:

- Das Reaktordesign und die Reaktorkühlung beeinflussen die Lastflexibilität der Methanisierungsreaktoren deutlich.
- Hinsichtlich der Variation der Eintrittsparameter weisen gekühlte Reaktoren eine große Prozesssensitivität auf, die den Lastbereich einschränkt oder nur durch eine sehr schnell steuerbare Reaktorkühlung ausgeglichen werden kann. Da adiabate Reaktoren auch bei kurzen Reaktorlängen das chemische Gleichgewicht erreichen, besitzen sie eine große Lastflexibilität. Dafür müssen adiabate Reaktoren durch die Rezirkulation von Produktgas gekühlt werden.
- Die Analyse mit zeitlich schwankenden Eintrittsparametern hat gezeigt, dass dynamische Phänomene bei der Methanisierung in Festbettreaktoren und somit auch bei vergleichbaren Power-to-X Synthesen berücksichtigt werden müssen. Zum Beispiel, kommt es bei einer Reduktion des Eintrittsvolumenstromes im transienten Verlauf zu einem Absinken der Temperatur im Reaktor und somit zu einem kurzzeitlichen Maximum des Methangehaltes. Umgekehrt führt eine Erhöhung des Eintrittsvolumenstroms zu einem transienten Maximum der Gastemperatur und einem kurzzeitigen Absinken des Methangehaltes. Diese dynamischen Phänomene schwächen sich bei geringer werdender Laständerungsgeschwindigkeit ab.
- Für adiabate Reaktoren existiert ein optimales Rezirkulationsverhältnis. Bei gekühlten Reaktoren wirkt sich die Produktrückführung negativ auf dem Umsatz aus, hat aber einen positiven Einfluss auf die Reduktion der Prozesssensitivität.
- Bei adiabaten Reaktoren erreichen die transienten Extrema, die bei der Änderung der Eintrittsparameter auftreten, das Ende des Reaktors, so dass durch die Produktrückführung eine zusätzliche instationäre Rückkopplung auftritt. Durch eine Erhöhung des Rezirkulationsverhältnisses bis zum optimalen Wert, können die dynamischen Phänomene reduziert werden.

Die Produktrückführung ist somit eine wichtige Steuergröße zur Regelung des Reaktor im stationären und dynamischen Betrieb. Zudem liefert diese Arbeit in der Zusammenfassung viele Hinweise zum Reaktordesign für den dynamischen Betrieb im Power-to-Gas Verfahren. Weiterhin wurden Betriebsstrategien des Festbettreaktors unter instationären Bedingungen abgeleitet und Grundlagen für die Entwicklung einer Prozessregelung gelegt. Diese Arbeit konnte deutlich die Komplexität des dynamischen Betriebes hervorheben und liefert in vielerlei Hinsicht Ausgangspunkte für weitere Detailuntersuchungen.

Abstract

Power-to-X (PtX) processes are one of many potential options which allow the storage of fluctuating wind and solar energy. They enable the long-term energy storage and the coupling of the energy production with energy-consuming sectors (sector coupling). Examples include the production of heat (Power-to-Heat) or applications in the chemical industry by supplying hydrogen via water electrolysis. In the power-to-gas process (PtG) process, carbon oxides from various sources can be hydrogenated via electrolytically-produced hydrogen to methane (methanation). After a product gas refinement, the methane can be stored as synthetic natural gas (SNG) in the existing infrastructure, e.g. in the gas grid, and utilized on demand.

The first process step of the PtG process, the water electrolysis, operates under dynamic conditions due to the fluctuating electricity input. With the aim to reduce the costs of hydrogen storage by minimizing storage capacities, the unsteady-state operation of the methanation reaction is demanded as well. However, the occurring phenomena and operation strategies under dynamic conditions are not exhaustively addressed in scientific literature thus far. Therefore, this thesis focuses on the unsteady-state operation of the exothermic methanation of carbon dioxide in a fixed-bed recycle reactor. On the one hand, the reactor can be cooled with help of the product recirculation, being state-of-the-art for adiabatic methanation reactors during steady-state operation. On the other hand, fixed-bed reactors with the recirculation of product gas are recommended for the operation under unsteady-state conditions. Therefore, in this context the hypothesis is tested, if the product recirculation is beneficial for controlling the reactor dynamics as a physical feedback loop. Furthermore, the results shall be attributed to load flexibility, reactor design, as well as operation and control strategies.

Simulation experiments based on a dynamic (multiphase, 1D) reactor model and physical experiments at a lab-scale synthesis plant were conducted. In the first step, a system characterisation and a validation took place based on experiments with temporally constant inlet parameters. Reactor cooling, the recycle ratio, and inlet parameters were varied. In the second step, the dynamic behaviour was analysed in dependence of inlet load ramps without any product recirculation. Finally, it was proven how the product recirculation influences the dynamics of a fixed-bed reactor.

The main observations are:

- The reactor design and cooling influence the load flexibility of methanation reactors significantly. For example, on the one hand, the start-up time (until the steady

state is reached) is influenced by the reactor sizes and the existing thermal storage masses. On the other hand, the lower the steady-state temperature level, the lower the start-up time is. Thus, the start-up time of the cooled fixed-bed reactor is considerably faster compared to adiabatic reactors, because less energy has to be provided by reaction enthalpy to heat-up the reactor and to reach the steady state.

- Regarding the variation of inlet parameters, cooled reactors have a very high process sensitivity, which limits the load range and which can only be compensated by a fast and effective process control. Adiabatic reactors can be operated well with partial and excess load, because chemical equilibrium is reached by short reactor lengths. But they reach a high adiabatic temperature level and therefore have to be cooled by the recirculation of product gas.
- The experiments with temporally varying inlet parameters have shown that dynamic phenomena have to be considered for the methanation in fixed-bed reactors and consequently for similar syntheses in Power-to-X processes as well. Exemplary for the variation of the inlet flow rate, a reduction leads to a drop of the temperature in the reactor and a short-term maximum of the methane content. In contrast, an increase of the volumetric flow rate introduces a transient rise of the temperature and a reduction of the methane content. The intensity of dynamic phenomena can be reduced if the gradient of the load change is decreased.
- For adiabatic reactors, an optimal recycle ratio exists. Even though the product recirculation influences the conversion in cooled reactors negatively, it reduces the process sensitivity and thus the load range can be expanded.
- For unsteady operating adiabatic reactors, the transient extrema reach the reactor outlet. Therefore, the product recirculation leads to a dynamic feedback. By increasing the recycle ratio to the optimal value during the load ramp, the transient extrema can be lowered.

Hence, the product recirculation is an important control parameter for fixed-bed reactors during the steady-state and the unsteady-state operation. Additionally, this work summarises design criteria for methanation reactors in the PtG process and derives operation strategies under dynamic conditions as the basis of controller development. This thesis highlights the complexity of the unsteady-state operation and provides a starting point for further investigation.

Acknowledgements

I would like to express the deepest appreciation to Prof. Dr.-Ing. Robert Güttel (Professor for Chemical Engineering at Ulm University) for his review of the thesis, his sustained mentoring and supervision, and for our constructive discussions with a heap of productive feedback.

I was in the lucky situation to have two supervisors, because I have worked as a guest scientist at the DBFZ Deutsches Biomasseforschungszentrum gemeinnützige GmbH during the time spent working on my PhD. Prof. Dr.-Ing. Stefan Rönsch, the leader of the working group ‘Syngas Technologies’ and Professor at the Department of Industrial Engineering at the Ernst-Abbe-Hochschule Jena, supported this work from its genesis to the final thesis. Thank you very much!

Furthermore, I would like to thank Prof. Dr.-Ing. Thomas Turek (Professor of Chemical Process Engineering at TU Clausthal) for taking over the external review of the thesis.

In addition, I thank the members of the working group ‘Syngas Technologies’ and of the Professorship for Chemical Engineering for their scientific exchange. The practical work at the synthesis plant was, on one hand, supported by the technician Alexander Feist who had done essential work on the assembly, reconstruction, and automation of the plant; a big thank you for this. On the other hand, the initial parts of the experiments were performed by Raphael Krüger during his internship and Bachelor thesis. I would also like to thank the leaders of the Biorefineries Department, Dr.-Ing. Franziska Müller-Langer and Dr.-Ing. Michael Seiffert, who afforded me the opportunity and the freedom to work on the PhD project.

The PhD time was funded by a two year scholarship of the Reiner-Leomine-Stiftung, which was financed by the DBFZ to one third.

Finally, I must express my very profound gratitude my family for the support in all part of life and the everyday motivation by their smile.

Contents

| | | |
|----------|--|-----------|
| 1 | Introduction | 1 |
| 1.1 | Background | 1 |
| 1.2 | Problem statement and objectives | 2 |
| 1.3 | Thesis structure | 3 |
| 2 | Fundamentals | 7 |
| 2.1 | Methanation of carbon dioxide | 7 |
| 2.1.1 | Catalytic reaction | 7 |
| 2.1.2 | Reactor concepts | 10 |
| 2.2 | Fundamentals of fixed-bed reactors | 12 |
| 2.3 | Dynamics of fixed-bed reactors | 15 |
| 2.3.1 | Load flexibility | 15 |
| 2.3.2 | Dynamic phenomena | 16 |
| 2.3.3 | Prerequisites for dynamic phenomena | 19 |
| 2.3.4 | Influence of product recirculation | 20 |
| 2.4 | Unsteady operation of the methanation | 21 |
| 2.4.1 | Catalyst scale | 21 |
| 2.4.2 | Reactor scale for fixed-bed reactors | 22 |
| 3 | Modelling and simulation | 25 |
| 3.1 | Dynamic reactor model | 25 |
| 3.2 | Implementation and numerical solution | 29 |
| 3.3 | Simulation parameters | 31 |
| 4 | Experimental methods | 35 |
| 4.1 | Experimental set-up | 35 |
| 4.2 | Analytics and LabVIEW control program | 37 |
| 4.3 | Experimental procedure | 39 |
| 4.4 | Results evaluation | 41 |
| 5 | Simulation results and discussion | 45 |
| 5.1 | Sensitivity analysis to determine the load flexibility | 45 |
| 5.1.1 | Steady-state behaviour (base case) | 45 |
| 5.1.2 | Load range regarding the inlet parameters | 47 |

| | | |
|----------|--|------------|
| 5.2 | Load changes without product recirculation | 53 |
| 5.2.1 | Start-up behaviour | 55 |
| 5.2.2 | Dynamic behaviour of the adiabatic reactor | 56 |
| 5.3 | Product recirculation to control dynamic operation | 61 |
| 5.3.1 | Effect of product recirculation on load range | 62 |
| 5.3.2 | Control of dynamic operation | 65 |
| 5.3.3 | Adaptation of the recycle ratio | 68 |
| 6 | Experimental verification | 71 |
| 6.1 | Load changes without product recirculation | 71 |
| 6.1.1 | Slow load ramps | 71 |
| 6.1.2 | Fast load ramps | 73 |
| 6.2 | Product recirculation to control dynamic operation | 76 |
| 6.2.1 | Influence on the steady-state behaviour | 77 |
| 6.2.2 | Control of dynamic operation | 77 |
| 7 | Conclusion for unsteady operation | 81 |
| 7.1 | Load flexibility | 81 |
| 7.2 | Design criteria | 82 |
| 7.3 | Operation and control strategies | 83 |
| 7.4 | Application of the results | 84 |
| 8 | Summary and outlook | 87 |
| 8.1 | General conclusion | 87 |
| 8.2 | Future work | 88 |
| A | Fundamentals | 91 |
| A.1 | Calculation of equilibrium composition | 91 |
| A.2 | Model selection | 92 |
| B | Modelling and simulation | 95 |
| B.1 | Derivative of the velocity | 95 |
| B.2 | Model parameters | 98 |
| B.3 | Validation of the process sensitivity for cooled reactors | 102 |
| B.4 | Comparison of effectiveness and activity factor | 103 |
| C | Experimental methods | 107 |
| C.1 | Synthesis test facility | 107 |
| C.2 | Catalyst preparation | 110 |
| C.3 | Balance of the experimental results – theory of key components | 111 |
| | Nomenclature | 113 |
| | Bibliography | 119 |

List of publications **139**

Copyright notice **141**

1 Introduction

1.1 Background

Against the background of climate change and the aim of the United Nations to limit the “increase in the global average temperature [...] below 2 °C above pre-industrial levels” (United Nations 2016), the energy transition is pursued with ambitious goals for the reduction of greenhouse gas emissions, the improvement of energy efficiency, and the share of renewable energies at the energy consumption. The European Union aims at 27 % of the gross final energy consumption in 2030 (European Commission 2014a) and assumes 75 % in a positive scenario for 2050 (European Commission 2014b, scenario: high renewable energy sources (RES)). Nearly the same goals are proclaimed in the German energy concept (30 % of the gross final energy consumption in 2030 and 60 % for 2050, Bundesministerium für Wirtschaft und Technologie (BMWi) 2010). Due to the high ratios of fluctuating renewable energy, storage technologies are required to ensure the security of electricity supply (Ausfelder et al. 2017; Beck et al. 2013; Pregger et al. 2012) and to challenge the must-run basis of conventional power generation plants (Hack et al. 2013). Thema et al. (2016) prognosticated an annual energy surplus of 154 TWh in 2050 for 100 % RES in Germany. And vice versa, the storage of electricity supports the integration of renewable energies and reduces the fluctuation of the electricity prices (Agricola et al. 2012).

Storage technologies are classified amongst other criteria according to their storage time in long- (several days until years) and short-term (lasting up to one day) storages (Sterner et al. 2017; Zapf 2017). Long-term storage technologies are preferentially required after the year 2030 to store fluctuating renewable energies (Hack et al. 2013; Pregger et al. 2012). Technologies usable for long-term storage include the power-to-gas (PtG) process and pumped hydroelectric energy storages (PHESs)¹. Especially, PtG “might be more suitable for countries with an extensive gas network, and which are lacking the characteristics required for the application of PHES” (Boer et al. 2014), which is the case in Germany with only 0.05 TWh_{el} installed capacity of PHESs (Ess et al. 2012). Furthermore, “a long-term energy storage system [...] can reduce the levelised cost of electricity (LCOE) of the energy system” (Kötter et al. 2016). A comparison shows that long-term storage technologies are

¹<https://www.bmwi.de/Redaktion/DE/Textsammlungen/Energie/speichertechnologien.html> (accessed 15.07.2018)

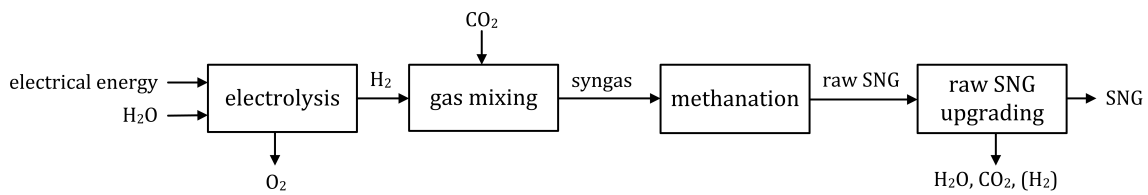


Figure 1.1: Flow diagram of the power-to-gas (PtG) process.

featured by high capacities, low self-discharge rates and medium efficiency (Belderbos et al. 2015; Hack et al. 2013).

The PtG process (Fig. 1.1) consists of two main process steps, the water electrolysis and the methanation, and was comprehensively reviewed by Ghaib et al. (2018), Götz et al. (2016) and Lehner et al. (2014) and Schiebahn et al. (2015). This concept first proposed by Hashimoto et al. (1999). In the first step, the fluctuating electrical energy produced by wind and solar power is used to operate a water electrolysis for the production of hydrogen. Oxygen is produced as a by-product. Downstream, the hydrogen is mixed with carbon dioxide (CO_2) or carbon monoxide (CO). Various sources of carbon oxide are discussed in industry and scientific literature, for example biogas (Jürgensen et al. 2015, Audi e-gas plant²), industrial flue gases (Bailera et al. 2017a; Iaquaniello et al. 2018; Lehner et al. 2017; Müller et al. 2013; Schöß et al. 2014), or atmospheric CO_2 (direct air capture (DAC), e.g. by Climeworks³ or Skytree^{®4}). In the second step, the mixed gas is catalytically converted to methane (methanation). After a product gas refinement, the synthetic natural gas (SNG) can be stored in the existing infrastructure, e.g. in the gas grid, and utilized on demand. The storage of the methane-rich SNG is favoured, because in comparison to hydrogen the energy density is tripled from 12.7 to 39.8 MJ m³ (STP) (Bajohr et al. 2011; Rachow 2017). Furthermore, gas reservoirs allow the storage of 232 TWh natural gas in Germany⁵. PtG-projects from lab to industrial scale are reviewed by Bailera et al. (2017b), and with special focus on hydrogen production by Buttler et al. (2018) and Gahleitner (2013) or on methanation by Ghaib et al. (2016) and Rönsch et al. (2016b). An overall process efficiency of 85.9% can be reached if the excess heat is used completely, and 54.3% if not (Frank et al. 2018).

1.2 Problem statement and objectives

The first process step for PtG (the water electrolysis) operates under dynamic conditions due to the fluctuating electrical input. The load can be reduced down to 20% for alkaline

²<https://www.audi-technology-portal.de/de/mobilitaet-der-zukunft/audi-future-lab-mobility/audi-future-energies/audi-e-gas> (accessed 23.05.2018)

³<http://www.climeworks.com/> (accessed 14.08.2018)

⁴<https://www.skytree.eu/> (accessed 14.08.2018)

⁵<https://agsi.gie.eu/#/historical//DE> (accessed 28.11.2017)

electrolysis (AEL) (Little et al. 2007) and to 5% for polymer electrolyte membrane electrolysis (PEM-EL) (Ulleberg et al. 2010), respectively. Overload operation is possible as well (Milanzi et al. 2018). Up to 8% of the total investment costs can be saved for a market-led operation of the second step, the methanation, (Aicher et al. 2014; Götz et al. 2016; Iglesias González et al. 2016b). Additionally, the operational costs for compressing the hydrogen can be reduced. However, the occurring phenomena and operation strategies under dynamic conditions are not exhaustively addressed in scientific literature thus far. Therefore, this thesis focuses on the unsteady-state operation of the exothermic methanation of carbon dioxide.

In detail, the unsteady-state operation of a fixed-bed recycle reactor is investigated. On the one hand, the reactor can be cooled with help of product recirculation, being state-of-the-art for adiabatic methanation reactors during steady-state operation mode. For cooled reactors, it is only applied for other synthesis reaction (e.g. the methanol synthesis (Bertau et al. 2014)). The recycle ratio (molar gas flow rate of the recycle related to the inlet of the system) is typically chosen in a range between 0.5 and 3.0 for methanation reactors (Gao et al. 2012; Er-Rbib et al. 2014). However, the product circulation causes higher operation costs for product separation, recycle compression and re-heating of the recycle stream (Eigenberger et al. 2012). On the other hand, fixed-bed reactors with the recirculation of product gas are recommended for the operation under unsteady-state conditions (Iglesias González et al. 2016a,b). Therefore, in this context the hypothesis is tested, if the product recirculation is beneficial for controlling the reactor dynamics as a physical feedback loop. Furthermore, the results shall be attributed to load flexibility, reactor design, as well as operation and control strategies. A detailed definition of the term ‘load flexibility’ will supply evaluation criteria, in turn allowing for the comparison of the unsteady-state operation of different reactor types.

The complete PtG process chain with auxiliary units (e.g. gas mixing or downstream gas conditioning) are not considered in this thesis. Thus, an economic evaluation of the unsteady-state operation was not conducted. The dynamic behaviour of the fixed-bed recycle reactor is researched from a reactor and systems perspective, meaning that the dynamic processes on a catalyst scale – including transient kinetics – were not in the focus of research.

1.3 Thesis structure

Initially, the 2nd chapter informs about fundamental aspects of the methanation reaction and the design of methanation reactors; followed by a characterization of fixed-bed reactors with emphasis on model approaches, their unsteady-state operation, and dynamic phenomena occurring for exothermic reactions. This chapter is completed with a definition of the term ‘load flexibility’ and a literature review for the unsteady-state operation of the methanation in fixed-bed reactors on reactor and catalyst scales.

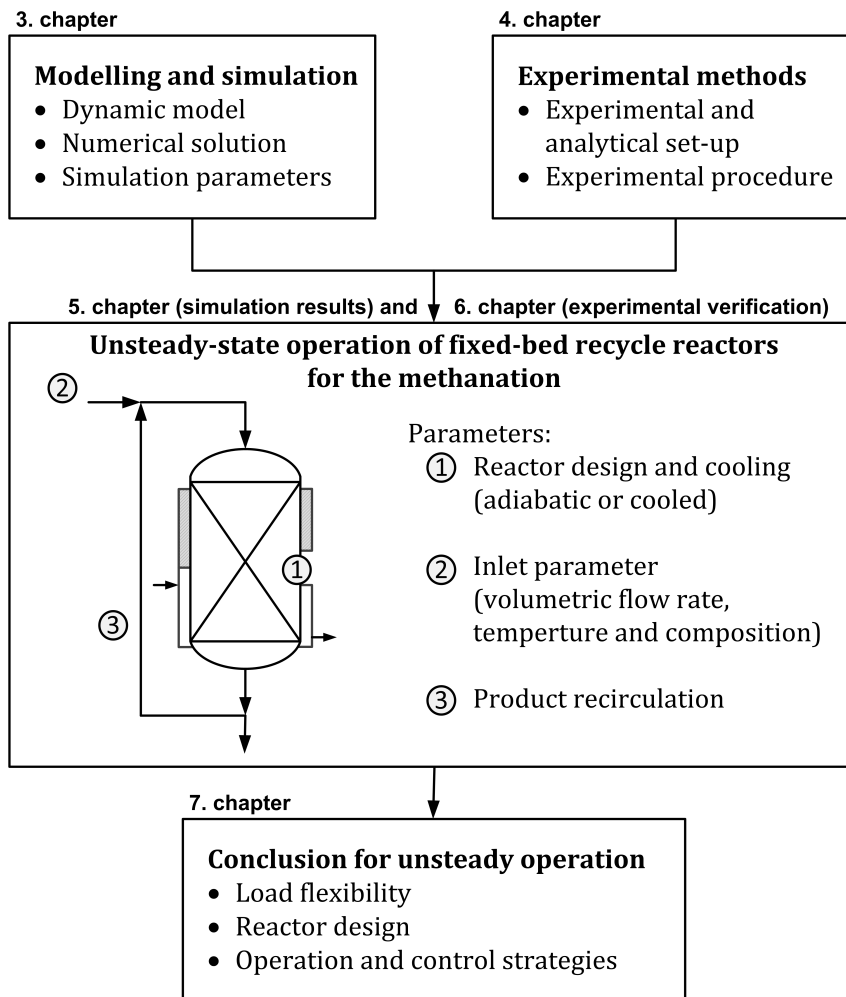


Figure 1.2: Thesis structure and task overview.

The further thesis structure is summarized in Figure 1.2. The unsteady-state operation of a fixed-bed recycle reactor is investigated by simulation experiments (chapter 3) and physical experiments (chapter 4). A dynamic (multiphase, 1D) fixed-bed reactor model, allowing the recirculation of product gas, was developed and numerically solved with MATLAB. For the lab-scale experiments, a test facility with a fixed-bed recycle reactor was built and commissioned. The lab-scale test facility was controlled by a LabVIEW program enabling the temporal adaptation of the parameter specification to fulfil load steps and ramps.

In the first step, a system characterisation with temporally constant inlet parameters based on simulation experiments (section 5.1), and with focus on the product recirculation (sections 5.3.1 and sections 6.2.1) took place. In the second step, the dynamic behaviour was analysed in dependence of load ramps at the systems inlet without any product recirculation (sections 5.2 and 6.1). In the third step, it was proven how the product

recirculation influences the dynamics of the fixed-bed recycle reactor (sections 5.3 and 6.2). Consequently, a conclusion for the unsteady operation of the fixed-bed recycle reactor is drawn, concerning the factors load flexibility, reactor design, as well as operation and control strategies (chapter 7). Finally, chapter 8 gives a summary and highlights suggestions for further research tasks.

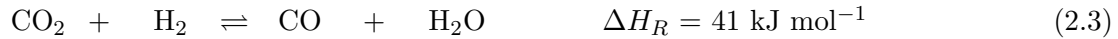
2 Fundamentals

2.1 Methanation of carbon dioxide

In 1902, the methanation of carbon oxides was discovered by Sabatier and Senderens (Sabatier et al. 1902a,b). The fundamental aspects of this heterogeneously-catalysed reaction, like reaction equations, chemical equilibrium, reaction mechanism, and kinetic models, are summarized in the subsection 2.1.1. Reactor concepts for the methanation of carbon dioxide are presented in subsection 2.1.2.

2.1.1 Catalytic reaction

The methanation of CO₂ (Eq. 2.1) can be described by a linear combination of CO methanation (Eq. 2.2) and reverse water–gas shift reaction (Eq. 2.3). Additionally, other reactions can occur between the participating species (Table 2.1).



The methanation of carbon dioxide is characterized by a significant heat release of 1.8 kW m_{SNG}⁻³ and a volumetric contraction of the reacting gases by 40 % (Rönsch et al. 2016b). In order to obtain a high methane yield, low temperatures and high pressures are favourable for thermodynamic reasons. Gao et al. (2012) and Sahebdehfar et al. (2015)

Table 2.1: Other possible reactions involved in the methanation of carbon oxides (Gao et al. 2012; Kiewidt 2017).

| No. | Name | Reaction | ΔH_R at 298 K kJ mol ⁻¹ |
|-----|---------------------------|---|---|
| 1 | methane dry-reforming | $\text{CO}_2 + \text{CH}_4 \rightleftharpoons 2\text{CO} + 2\text{H}_2$ | +247 |
| 2 | Boudourad reaction | $2\text{CO} \rightleftharpoons \text{C} + \text{CO}_2$ | -172 |
| 3 | methane cracking | $\text{CH}_4 \rightleftharpoons \text{C} + 2\text{H}_2$ | +75 |
| 4 | carbon monoxide reduction | $\text{CO} + \text{H}_2 \rightleftharpoons \text{C} + \text{H}_2\text{O}$ | -131 |
| 5 | carbon dioxide reduction | $\text{CO}_2 + 2\text{H}_2 \rightleftharpoons \text{C} + 2\text{H}_2\text{O}$ | -90 |

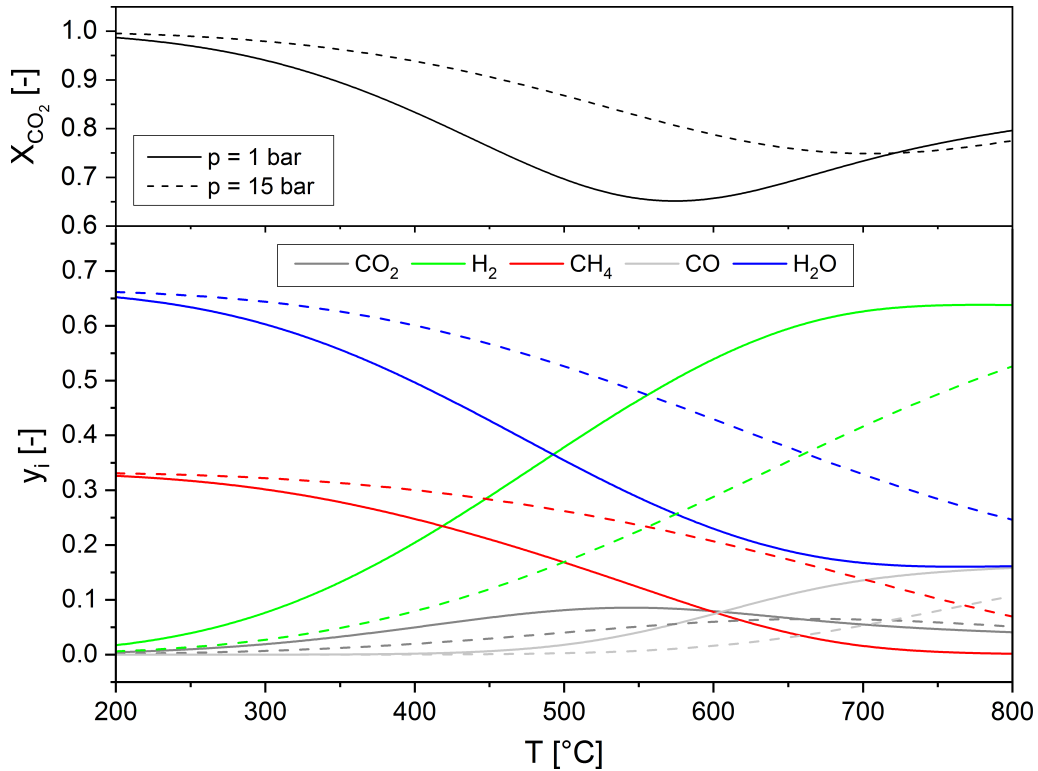


Figure 2.1: Pressure and temperature influence on the equilibrium conversion of carbon dioxide X_{CO_2} (top) and composition y_i (bottom) (educt gas composition: $y_{H_2} = 0.8$, $y_{CO_2} = 0.2$).

provide a comprehensive thermodynamic analysis of the methanation reactions of carbon oxides based on the Gibbs free energy minimization method. Similar results can be calculated with equilibrium constants published in literature (as described in appendix A.1). Figure 2.1 shows the carbon dioxide conversion and the gas composition in dependence of the temperature and the pressure (for 1 and 15 bar). At 1 bar, the conversion of carbon dioxide decreases at 570 °C to 65 %, since less carbon dioxide is converted to methane. At higher temperatures, the carbon dioxide conversion increases again as the reverse water-gas shift reaction is pronounced. For a pressure of 15 bar, the minimum carbon dioxide conversion occurs with 75 % at 700 °C. Thus, higher pressure extends the technically interesting operation range to higher reactor temperatures.

Eight electrons have to be transferred for the complete oxidization of carbon to methane being a high kinetic barrier (Kuznecova et al. 2017; Park et al. 2009). Therefore, group VIII metals are typically used as methanation catalysts (Frontera et al. 2017; Watson 1980; Weatherbee et al. 1981, 1984; Zhilyaeva et al. 2002), which are $Ru > Fe > Ni > Co > Mo$ in the order of their activity (Mills et al. 1974) and considering the metal's surface area (Vannice 1976). Where the order of selectivity is $Ni > Co > Fe > Ru$ (Schmidt et al.

Table 2.2: Overview of recent kinetic models for the CO₂ methanation on nickel catalysts.

| Catalyst (Ni wt%) | T [°C] | p_{max} [bar] | Rate equation r_j |
|--|-------------|--------------------|---|
| Koschany et al. 2016 Ni/Al ₂ O ₃ (19) | 180–340 | 15 | $r_{\text{CO}_2\text{-Meth.}} = \frac{k_1 p_{\text{H}_2}^{0.5} p_{\text{CO}_2}^{0.5} \left(1 - \frac{p_{\text{CH}_4} p_{\text{H}_2\text{O}}^2}{p_{\text{CO}_2} p_{\text{H}_2}^4 K_{\text{eq},1}} \right)}{\left(1 + K_{\text{OH}} p_{\text{H}_2\text{O}} p_{\text{H}_2}^{-0.5} + K_{\text{H}_2} p_{\text{H}_2}^{0.5} + K_{\text{mix}} p_{\text{CO}_2}^{0.5} \right)^2}$ |
| Lim et al. 2016 Ni/Al ₂ O ₃ (12) | 180–210 | 20 | $r_{\text{CO}_2\text{-Meth.}} = \frac{k_1 p_{\text{CO}_2}^{0.5} p_{\text{H}_2}^{0.5}}{\left(1 + K_1 p_{\text{CO}_2}^{0.5} p_{\text{H}_2}^{-0.5} + K_2 p_{\text{CO}_2}^{0.5} p_{\text{H}_2}^{0.5} + K_3 p_{\text{H}_2\text{O}} \right)^2}$ |
| Zhang et al. 2013 Ni/Al ₂ O ₃ (50) | 250–360 | 5 | $r_{\text{CO-Meth.}} = \frac{k_2 K_{\text{C}} K_{\text{H}}^2 p_{\text{CO}}^{0.5} p_{\text{H}_2}}{\left(1 + K_{\text{C}} p_{\text{CO}}^{0.5} + K_{\text{H}} p_{\text{H}_2}^{0.5} \right)^3}$ $r_{\text{rWGS}} = \frac{-k_3 p_{\text{H}_2}^{-1} (p_{\text{CO}} p_{\text{H}_2\text{O}} - p_{\text{H}_2} p_{\text{CO}_2} K_{\text{eq},3})}{\left(1 + K_{\text{CO}} p_{\text{CO}} + K_{\text{H}_2} p_{\text{H}_2} + K_{\text{H}_2\text{O}} p_{\text{H}_2\text{O}} p_{\text{H}_2}^{-1} \right)^2}$ |
| Rönsch et al. 2016a | | | $r_{\text{CO-Meth.}} = \frac{k_2 K_{\text{C}} K_{\text{H}}^2 p_{\text{CO}}^{0.5} p_{\text{H}_2} \left(1 - \frac{p_{\text{CH}_4} p_{\text{H}_2\text{O}}}{p_{\text{CO}} p_{\text{H}_2}^3 K_{\text{eq},2}} \right)}{\left(1 + K_{\text{C}} p_{\text{CO}}^{0.5} + K_{\text{H}} p_{\text{H}_2}^{0.5} \right)^3}$ |

2018). For technological applications, nickel catalysts are most commonly applied due to their high activity, the highest selectivity and their affordability (Su et al. 2016). In summary, nickel catalysts have the best performance-cost-ratio. Nickel catalyst loading is in the range of 10–40 wt% for commercial applications (Rachow 2017). Often nickel is supported by the γ -modification of Al₂O₃ (Gao et al. 2015), but SiO₂, TiO₂, ZrO₂, CeO₂, and zeolites are used as well (Li et al. 2018; Muroyama et al. 2016; Vance et al. 1983).

Two different kinds of reaction mechanisms are published in the literature (Miao et al. 2016). In the dissociative pathway the C–O bonds are broken before hydrogenation, meaning in detail that CO₂ dissociates to CO* and C* (Marwood et al. 1997; Peebles et al. 1983; Weatherbee et al. 1982). In the associative pathway the C–O bonds are broken by hydrogen atoms and formate species (HCOO[–]) are produced as an intermediate (and not CO) (Mills et al. 1974; Pan et al. 2014). Baraj et al. (2016) pointed out that the dissociative pathway is generally more accepted nowadays. Westermann et al. (2015) and Aldana et al. (2013) specified that basic sites are required for the associative pathway. This pathway “might be important in the formation of higher hydrocarbons in Fischer–Tropsch synthesis” (Araki et al. 1976; Rönsch et al. 2016b).

Katoufa et al. (2015) and Koschany et al. (2016), and Koytsoumpa et al. (2018) summarized kinetic models for the CO₂ methanation on nickel catalysts. Recent kinetic models were published by Koschany et al. (2016), Lim et al. (2016), and Rönsch et al. (2016a) (Table 2.2). The first two neglected the CO methanation due to the low conversion of the reverse water-gas shift reaction below 350 °C. But Koschany et al. (2016) assumed that formyl formation

is the rate-determining step (RDS) (associative pathway), whereat Lim et al. (2016) proclaimed that the dissociation of adsorbed CO is the RDS (dissociative pathway). Zhang et al. (2013) derived the CO₂ methanation kinetics as a linear combination of the rate equations for the CO methanation (Klose et al. 1984) and the reverse water-gas shift (Xu et al. 1989a), and carried out a new parameter fitting. Rönsch et al. (2016a) added the reverse reaction in the model of Zhang et al. (2013). Until 2016 “simulation models most frequently apply the Langmuir–Hinshelwood kinetics published by Xu et al. (1989a) and Kopyscinski (2010)” (the latter only for CO methanation) (Rönsch et al. 2016b, section 7.2). Hitherto, there was no kinetic model published in the literature considering the transient phenomena at the catalyst surface, which occur during the unsteady-state operation (cf. subsection 2.4.1). Thus, a steady-state kinetic model had to be integrated in the dynamic reactor model.

2.1.2 Reactor concepts

Fixed-bed, fluidized-bed, bubble column, and structured reactors (Rönsch et al. 2016b) are developed for the highly exothermic methanation typically operating in the range of 250–650 °C (Güttel 2013; Kopyscinski et al. 2010) (Table 2.3). Rönsch et al. (2016b) gave a comprehensive overview of established methanation configurations and technologies available on the market. Previous reviews about methanation technologies were published by Kopyscinski et al. (2010) and Rönsch et al. (2011), and Schildhauer et al. (2015). Due to the significant heat release, the temperature control is a key factor. To design an optimal temperature profile in dependence of temperature limits, Kiewidt et al. (2015) applied the Semenov number Se (Eq. 2.4) to find the best compromise between a fast reaction rate accelerated by the reaction heat and a minimization of the thermodynamic limitation afterwards. Additionally, Lazdans et al. (2016) published a general concept for designing the methanation process by answering decision questions, first, on the catalyst scale, and second, on the reactor scale.

$$\begin{aligned}
 Se &= \frac{\text{heat production rate}}{\text{cooling rate}} \\
 &= \underbrace{\frac{d_r}{4 h_{w,a}}}_{\text{thermal design}} \underbrace{\frac{\eta r_{\text{CO}_2\text{-Meth.,in}} \rho_c (-\Delta H_R)}{T_{in}} \frac{E_A}{R T_{in}}}_{\text{reaction and process conditions}} \quad (2.4)
 \end{aligned}$$

Fixed-bed reactors are designed either as adiabatic reactors or as cooled multitubular reactors. For both cases, the axial and radial heat transfer is limited and the pressure drop is comparably high. The methanation in fixed-bed reactors is conducted in multiple stages with intercoolers and condensation units. El-Sibai et al. (2015) and El-Sibai et al. (2017) optimized the reactor configuration of polytropic fixed-bed reactors. Schaaf et al. (2014)

Table 2.3: Properties of reactor concepts for the methanation (Rönsch et al. 2016b, TRL updated).

| Property / Concepts | Fixed-bed | | Fluidized-bed | Bubble column | Structured |
|---------------------|----------------------|--------------|-----------------------|---------------------|-----------------------|
| | adiabatic | cooled | | | |
| Operation mode | adiabatic | polytropic | isothermal | isothermal | polytropic |
| Temperature [°C] | 250–700 | 250–500 | 300–400 | 300–350 | 250–500 |
| Semenov number | $\rightarrow \infty$ | $0 - \infty$ | $\rightarrow 0$ | $\rightarrow 0$ | $0 - \infty$ |
| Reactor stages | 2–7 | 1–2 | 1–2 | 1–2 | 1–2 |
| Recirculation | usually | sometimes | sometimes | none | none |
| Catalyst | packed | packed | fluidized | suspended | coated |
| Particle size | millimetres | millimetres | 100–500 μm | < 100 μm | 100–500 μm |
| Mechanical stress | low | low | high | medium | low |
| Thermal stress | high | medium | low | low | medium |
| GHSV | medium–high | high | medium–high | low–medium | medium |
| TRL | 9 | 9 | 8 | 4–5 | 8–9 |

GHSV – gas hourly space velocity, TRL – technology readiness level

and Türks et al. (2017) arranged multi-beds in the reactor (cf. section 2.2). Additionally, the recirculation of product gas or the injection of steam can be applied for reactor cooling, which dilutes the inlet gas stream and prevents catalyst deactivation by thermal sintering. An industrial molten-salt-cooled multitubular reactor operates in Wertle, known as the Audi e-gas plant and engineered by MAN (Specht et al. 2016). Further information about the dynamic of fixed-bed methanation reactors will be given in section 2.4.

The furthered development of fluidized-bed methanation was taken on, in large proportion by the Paul-Scherrer Institute (Schildhauer et al. 2016). Prototype demonstrations were carried out in a 1000 hour test for the direct methanation of raw biogas¹ and at the 1 MW_{SG} plant in Güssing for the CO methanation combined with a biomass gasifier. Fluidized-bed reactors have a good heat transfer characteristic allowing the reactor to operate nearly isothermally and be built in a one-stage process design. However, pronounced catalyst attrition is introduced by the fluidization.

Based on former developments, the application of bubble-column-reactors for methanation is forced by the DVGW Research Centre at Engler-Bunte-Institute of Karlsruhe Institute of Technology (Götz et al. 2013; Lefebvre et al. 2015, 2018). The three-phase reactors have low operating and maintenance costs (Kumar et al. 2012). The intensified heat transfer characteristic allows a nearly isothermal operation and an effective controlling of the temperature. On the other hand, drawbacks include the additional gas-liquid mass transfer resistance, as well as the decomposition and evaporation of the heat transfer liquid (Rönsch et al. 2016b).

Structured reactors for the methanation of carbon dioxide are very intensively investigated at the time of writing. Recent results were published amongst others by Belimov et al. (2017), Bengaouer et al. (2018), Biegger et al. (2018), Engelbrecht et al. (2017), Gruber

¹<http://www.sccer-biosweet.ch/power-to-gas-1000-hour-field-test-at-werdholzli/> (accessed: 25.05.2018)

et al. (2018) and Neubert et al. (2018), or Vázquez et al. (2018). On the basis of the high surface-to-volume ratio, structured reactors with microchannels have an improved “heat and mass transfer rate by one to two orders of magnitude” (Tonkovich et al. 2004) and a low pressure drop. Furthermore, they are easy to scale-up by modularization. The company ATMOSTAT sells the METHAMOD[®] reactor to the market, based on a compact exchanger-reactor technology with alternating micro-channel plates². The INERATEC GmbH produces microstructured reactors for the commercial market using the PtG process and other PtX technologies³. Besides the structuring of the reactor design, structured catalyst arrangements are discussed as well. For example, foams were investigated due their low pressure drop and improved radial heat transport (Frey et al. 2016; Kiewidt 2017).

2.2 Fundamentals of fixed-bed reactors

Fundamentally for the further thesis parts, hereinafter design criteria and the modelling of catalysed, gas-phase reactions in fixed-bed reactors are described.

Design criteria

Fixed-bed reactors (FBRs) with immobile and compact packed-beds are widely adopted for heterogeneously catalysed gas-phase reactions. The fundamentals of fixed-bed reactors were summarized by Andrigo et al. (1999) and Eigenberger et al. (2012), and Froment (1974). As shown in Fig. 2.2, fixed-bed reactors are distinguished by the arrangement of the catalyst bed and the reactor cooling in adiabatic reactors, multi-bed reactors, and multitubular reactors. The temperature increases linearly with the achieved conversion X for adiabatic reactors, if a constant reaction enthalpy ΔH_R , specific heat capacity $c_{p,g}$, and density ρ_g are assumed (Eq. 2.5, Eigenberger et al. 2012).

$$\Delta T_{ad} = \frac{-\Delta H_R c_{in}}{\rho_g c_{p,g}} X \quad (2.5)$$

Industrial synthesis processes in fixed-bed reactors operate generally under stationary conditions to keep the desired conversion constant (Andrigo et al. 1999; Eigenberger et al. 2012). The reactor’s dimensions and the process parameters are optimized for the stationary operation. But an unsteady-state operation is unavoidable during the start-up, shutdown, or in the case of automatic control actions. A variation of the inlet concentration – especially for natural feedstocks and unexpected disturbances (due to equipment failures) – lead to an unsteady-state operation as well (Dissinger et al. 1980). Moreover, the effectiveness of

²<https://www.atmostat-alcen.com/en/products/methanation-methamodr> (accessed: 25.05.2018)

³<http://ineratec.de/technologien/?lang=en> (accessed: 25.05.2018)

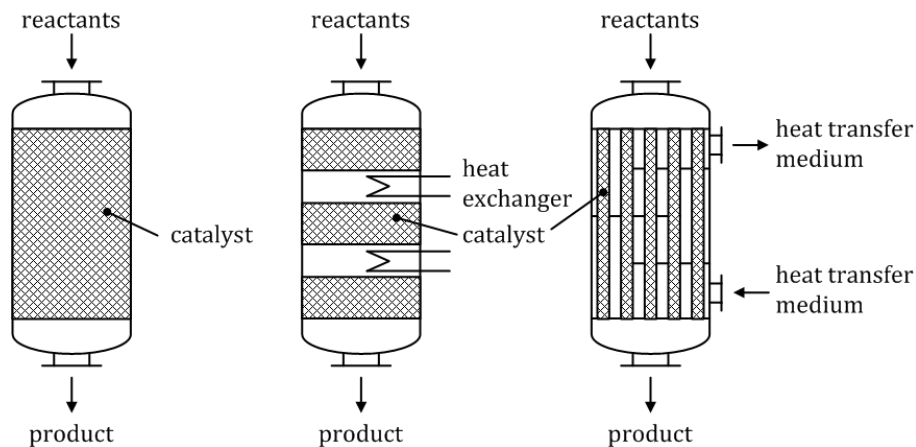


Figure 2.2: Design of fixed-bed reactors – adiabatic reactor (left), multi-bed reactor (middle), multitubular reactor (right); according to Eigenberger et al. (2012) and Jakobsen (2014).

process control systems can only be evaluated under unsteady-state conditions (Dissinger et al. 1980; Doesburg et al. 1976a).

Modelling

The fixed-bed reactor consists of multi-scale subsystems (Emig 1986), which can be modelled in different complexities in accordance to the aim of simulation. The smallest scale, at which the reaction takes place, are the active sites of the catalyst, where the molecules adsorb before, and desorb afterwards. These reaction steps are summarised in the micro kinetic model. In the next level, the transport processes in the catalyst particle and at the interphase are included; followed by the simulation of the fixed-bed in a single reactor tube where the fluid flow might consider axial and radial dispersion. At the largest scale, a multitubular reactor including the cooling medium can be modelled.

According to their modelling methodology, fixed-bed reactor models are divided in different categories (Figure 2.3). At the first level, predictive and learning models with neural networks are distinguished. Predictive models can be either deterministic or stochastic. Purely stochastic models are rarely used, because of their high computational-costs and the requirement for sufficient statistical information (Mederos et al. 2009). More common is the combination of a deterministic model with stochastic sub-models e. g. for the particle arrangement or the fluid flow (Adler 2000a,b). Deterministic models are either discrete models like cell models consisting of a network of stirred tank reactors (Iordanidi 2002) or the most widely-used continuum-models, which base on differential equations with one or more independent variables (Mederos et al. 2009).

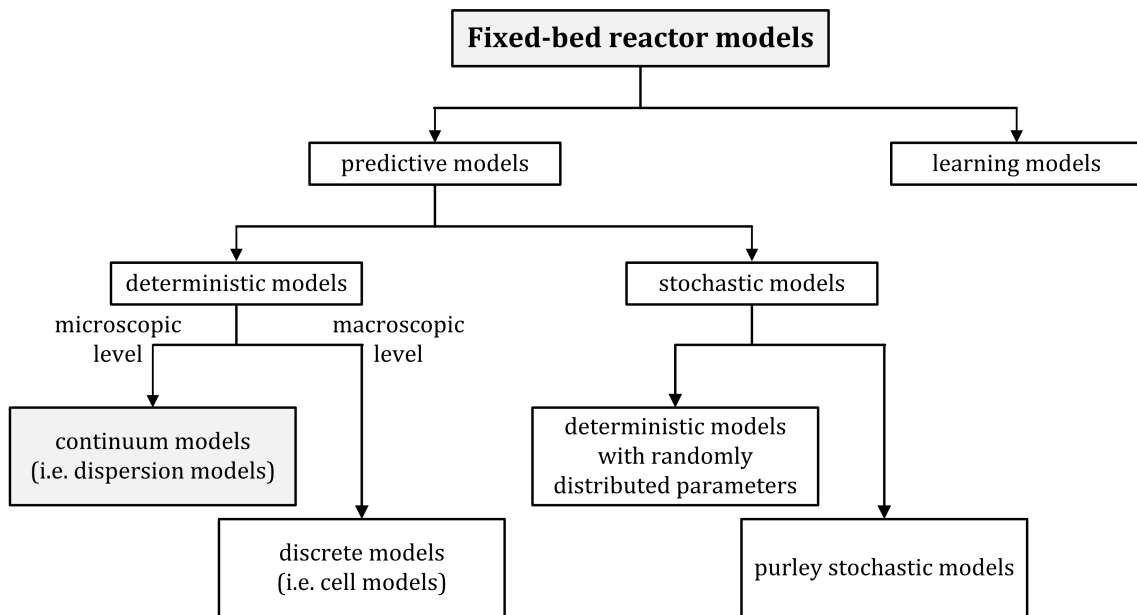


Figure 2.3: General classification of fixed-bed reactor models (Mederos et al. 2009).

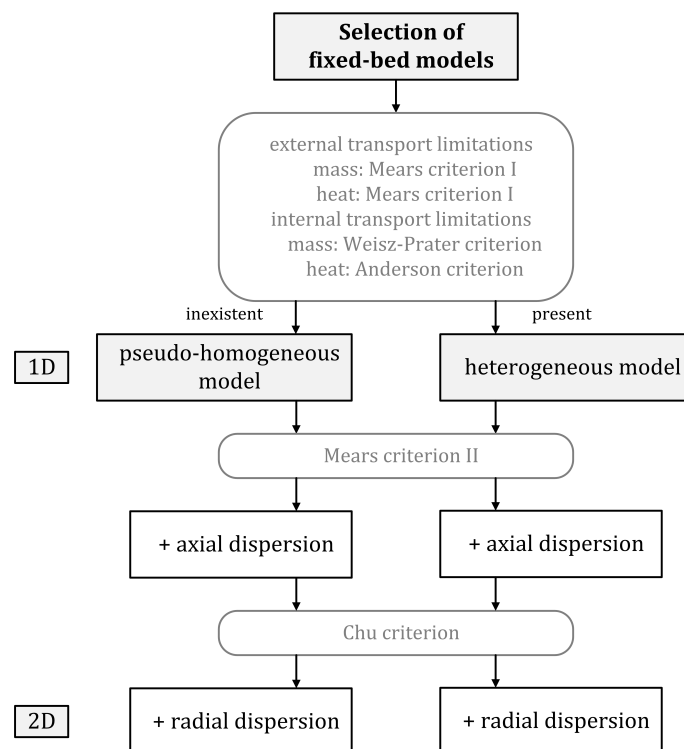


Figure 2.4: Classification of continuum fixed-bed reactor models and selection criteria (equations in appendix A.2).

The model complexity should be selected according to the purpose of investigation and the need for prediction capability (Mederos et al. 2009). Furthermore, the level of sophistication for modelling the fluid flow and mixing should be kept in relation to the understanding of the kinetics (Duduković et al. 2002). Different criteria can be found in the literature to estimate the required model complexity for continuum models (Fig. 2.4, equations are summarised in appendix A.2). This classification of continuum models (Froment 1974) does not include the temporal behaviour distinguished between steady state and unsteady state. If internal and external transport limitations for the heat and mass are not present, the phases can be summarized in an isotropic continuum (pseudohomogeneous model). Otherwise, the phases have to be considered separately with different temperatures and concentrations in the gas phase and at the surface of the catalyst (heterogeneous model) (Mederos et al. 2009). The flow pattern can be either considered as plug flow, without backmixing or any radial dependencies, being the simplest option. Otherwise, axial and radial dispersion, respectively, can be included in the flow pattern. In the latter case, the fixed-bed model is then two-dimensional. Thus, the differential equations for continuum models of fixed-bed reactors can be derived like a modular construction system (Table 2.4, Emig 1986). Nowadays, computational fluid dynamics (CFD) are applied for a more detailed, mostly 3D modelling of fixed-bed reactors (e.g. Wehinger et al. (2017a,b)). However, it requires a significant higher effort in methodology development and computation time.

This modelling methodology of fixed-bed reactors is applied to the methanation with the scope of process design, evaluation, optimization, and adaptation (Rönsch et al. 2016b). Furthermore, they have only distinguished between the reactor modelling and the modelling of the methanation as part of a SNG plant. Models of a single fixed-bed reactor are preferential one-dimensional, pseudohomogeneous continuum models, since they allow analysing qualitative trend with low computational effort.

2.3 Dynamics of fixed-bed reactors

At first, the term ‘load flexibility’ is defined in this section to derive evaluation criteria for unsteady-state operation (subsection 2.3.1) and next, dynamic phenomena are described in detail, because they might cause problems during the unsteady-state operation (subsection 2.3.2).

2.3.1 Load flexibility

The term ‘Load flexibility’ quantifies the potential of processes or reactors for transient operation between different steady states in a wide operating-window without imperilling the process safety (adapted definition from Effenberger (2000)). The four aspects of the load flexibility are the load range, the start-up and shutdown times, the load change

Table 2.4: Terms of continuum models for fixed-bed reactors (Emig 1986, symbols adapted).

| Term | Material | Heat |
|------------------------------------|--|--|
| reaction and deactivation | $\varrho_c r(c_c, T_c) \eta$ | $\varrho_c r(c_c, T_c) \eta (-\Delta_R H)$ |
| transport in the catalyst particle | $\frac{D_{eff}}{\xi^2} \frac{d}{d\xi} \left(\xi^2 \frac{dc_c}{d\xi} \right)$ | $\frac{\lambda_{eff}}{\xi^2} \frac{d}{d\xi} \left(\xi^2 \frac{dT_c}{d\xi} \right)$ |
| transport through phase boundaries | $k a_{v,gc} (c_g - c_{c,sur})$ | $h_{cg} a_{v,gc} (T_{c,sur} - T_g)$ |
| accumulation | $\frac{\partial c_g}{\partial t}$ | $\rho_g c_p \frac{\partial T_g}{\partial t}$ |
| convection | $u_s \frac{\partial c_g}{\partial z}$ | $u_s \rho_g c_p \frac{\partial T_g}{\partial z}$ |
| radial mixing | $D_{e,rad} \left(\frac{\partial^2 c_g}{\partial r^2} + \frac{1}{r} \frac{\partial c_g}{\partial r} \right)$ | in the fluid: $\lambda_{e,rad,g} \left(\frac{\partial^2 T_g}{\partial r^2} + \frac{1}{r} \frac{\partial T_g}{\partial r} \right)$ in the solid: $\lambda_{e,rad,c} \left(\frac{\partial^2 T_c}{\partial r^2} + \frac{1}{r} \frac{\partial T_c}{\partial r} \right)$ |
| axial mixing | $D_{e,ax} \frac{\partial^2 c_g}{\partial z^2}$ | $\lambda_{e,ax} \frac{\partial^2 T_g}{\partial z^2}$ |
| heat transfer at the reactor wall | | in the fluid: $h_{wg} a_{v,wg} (T_w - T_g)$ in the solid: $h_{wc} a_{v,wc} (T_w - T_c)$ |

D_e and λ_e – dispersion coefficients

D_{eff} – effective diffusion coefficient, λ_{eff} – effective thermal conduction coefficient

velocity, and the limitations of load changes (Figure 2.5). The load range is limited by engineering constraints to process variables, such as the maximum operating temperature of the catalyst or the pressure drop, which are affected by the load. Due to the complex interactions between load and reactor performance, in most cases, an optimal load for designing the steady state operation exists. The start-up and shutdown times specify the time duration, which is needed to change from one steady state to another (with the own detailed definitions as follows). Thereby, a ‘cold start’ means that the initial reactor temperature is below the operation temperature and the reactor is purged with inert gas during the heating process. For a ‘warm start’, the reactor temperature is raised, while the reactants are fed (start-up of the reaction). A ‘hot start’ occurs when the reactor operates at operation temperature and the reactants are fed again after a short interruption. The load change velocity specifies the time gradient of the load change. The last aspect covers limitations of the load flexibility, such as the total number of tolerated changes, the change frequency, or its shape.

2.3.2 Dynamic phenomena

Fixed-bed reactors operating under non-isothermal conditions can encounter dynamic (differential flow instability, DIFI) and static (parametric sensitivity, PS) instabilities. Both

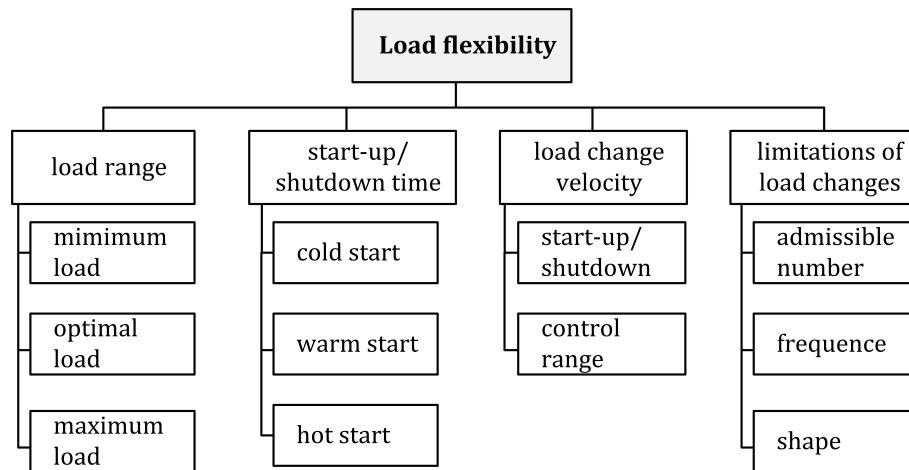


Figure 2.5: Aspects of the load flexibility (Effenberger 2000, reprinted and adapted with permission by Springer Nature).

amplify external perturbations and may result in reactor temperatures causing product deterioration, selectivity loss, or a thermal runaway (Yakhnin et al. 2015).

The parametric sensitivity (PS) means that “small changes in one or more of the reactor input parameters lead to much larger changes in the output variables” (Morbidelli et al. 1986). Multiple steady states can be expected in the PS regime (Puszyński et al. 1981) known from the ignition and extinction behaviour attributed to polytropic, back-mixed reactors. The resulting hysteresis loop should be calculated by a general model including axial and radial dispersion (Puszyński et al. 1981).

A differential flow arises when two or more distinct, interactive species move in a homogeneous flow-field with their individual flow velocity, which changes the dynamics of the system dramatically allowing differential flow instability (DIFI) to occur (Menzinger et al. 1995). Detailed information about the prerequisites of the DIFI are explained in subsection 2.3.3. The dynamic phenomena introduced by the DIFI include the wrong-way behaviour, moving hot-spots, and extinction-waves as shown in Figure 2.6. These effects are comparable and caused by inlet disturbances, which can lead to a temperature rise higher than the adiabatic temperature (Menzinger et al. 2004).

The **wrong-way behaviour** describes the temporary increase of reactor temperature, due to a sudden and permanent drop of the feed temperature and vice versa (Luss 1997; Yakhnin et al. 2004). The maximum temperature rise can be noticeably higher than the adiabatic temperature rise (Kulkarni et al. 1996). Doesburg et al. (1976a) pointed out that disturbance of feed temperature is the common type in practice, which appears for example if the pre-heater has a failure (Yakhnin et al. 2004). If feed temperature is decreased abruptly and permanently, the temperature front moves slowly downstream and thus the reaction rate decreases upstream. Consequently, a front with an elevated

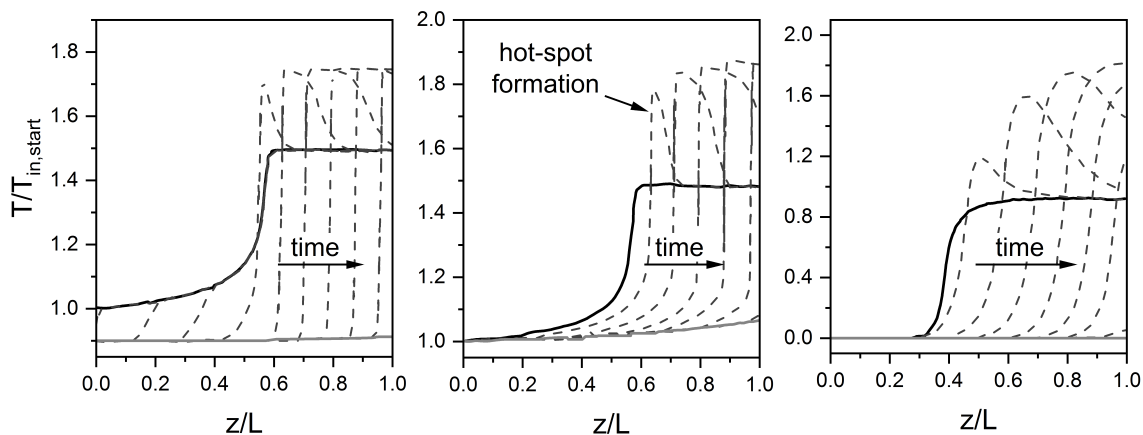


Figure 2.6: Dynamic phenomena of fixed-bed reactors: wrong-way behaviour (left), moving hot-spots (middle), and extinction-waves (right) (according to Yakhnin et al. 2004).

reactant concentration reaches the hotter part of the reactor and a hot-spot is formed by the heat release of the excess reactants (Yakhnin et al. 2004). The hot-spot temperature is influenced by the rate of heat transfer between the gas and the solid phase, the step height of the inlet temperature change, the heat of reaction, and the sensitivity of the reaction rate to the temperature, as well as the thermal heat capacity of the phases (Kulkarni et al. 1996). Furthermore, the adsorption of the reactants on the catalyst support reduces the transient temperature fronts (Il'in et al. 1992).

Moving hot-spots are usually induced by a variation of the feed-flow rate. For an increase, a localized and narrow hot-spot forms near the steady-state reaction zone (Yakhnin et al. 2004) and creeps downwards, thus shifting the reaction zone towards the outlet. The hot-spot broadens due to the differences in propagation velocity of the leading convective and the trailing dispersion front (Eigenberger et al. 2007). The concept of moving hot-spots is used in flow reversal reactors (Boreskov et al. 1983).

The **ignition and extinction processes** typically occur during the start-up and the shutdown of the synthesis reactor. If the inlet temperature rises, the activation energy of the catalyst is supplied and the reaction starts. The reaction zone is formed in the centre of the reactor and moves upstream to the reactor entrance caused by axial heat conduction (Gilles 1977). The heat accumulation at the reactor entrance leads to a high temperature peak. If the inlet temperature is lowered the reaction becomes extinct. Then the reaction zone moves downstream with increasing speed at a constant height and leaves the reactor. Depending on the flow-rate and on the inlet conditions, the reaction zone can be stopped at any location within the reactor (Gilles 1977).

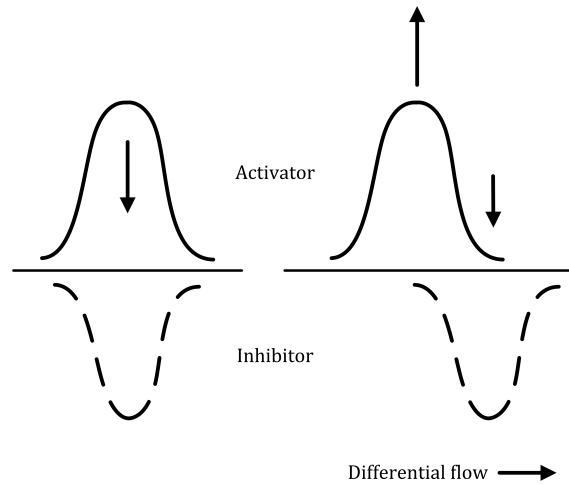


Figure 2.7: Activator-inhibitor system without (left) and with (right) differential flow (Yakhnin et al. 2004, reprinted with permission by De Gruyter).

Extinction waves are the result of a fast and local catalyst deactivation or reactant inhibited-processes. Therefore, it is expected that they play a minor role in methanation reactors.

2.3.3 Prerequisites for dynamic phenomena

The concept of the differential flow instability was developed by Rovinsky et al. (1992) and adapted to fixed-bed reactors by Yakhnin et al. (1995b). In fixed-bed reactors with exothermic reactions the interactive species represent an activator-inhibitor system, with the reaction heat – as an activator – having the tendency to grow (positive feedback) and with the extent of the reaction, which leads to a depletion of the reactants, as well as the heat dispersion as inhibitors (Menzinger et al. 2004; Yakhnin et al. 1995b). The reactor is stable if the inhibitor can balance local activator fluctuations (Yakhnin et al. 2004), but a sufficiently large differential flow moves the activator and the inhibitor against each other causing the DIFI as illustrated in Fig. 2.7. In fixed-bed reactors the packed-bed stores the heat and provides thermal inertia slowing down the transport of heat in the axial direction and leading to the inherent possibility of the DIFI formation (Yakhnin et al. 1995b).

The potential of self-acceleration can be identified by the axial temperature profile at steady state or by the temperature balance equation, where the second spatial derivation of the temperature has to be large ($\partial^2 T / \partial z^2 = T_{zz} > 0$) (Yakhnin et al. 2004, Fig. 2.8). The modified Peclet number Pe^* is calculated by the ratio of the length of the reaction zone L_{rct} to the particle size d_c and utilised as a stability criterion. If $Pe^* < 10$, meaning the reaction zone is comparably short, the system is dynamically stable (Yakhnin et al. 2004). The self-acceleration potential can be adjusted by the catalyst activity, the dilution

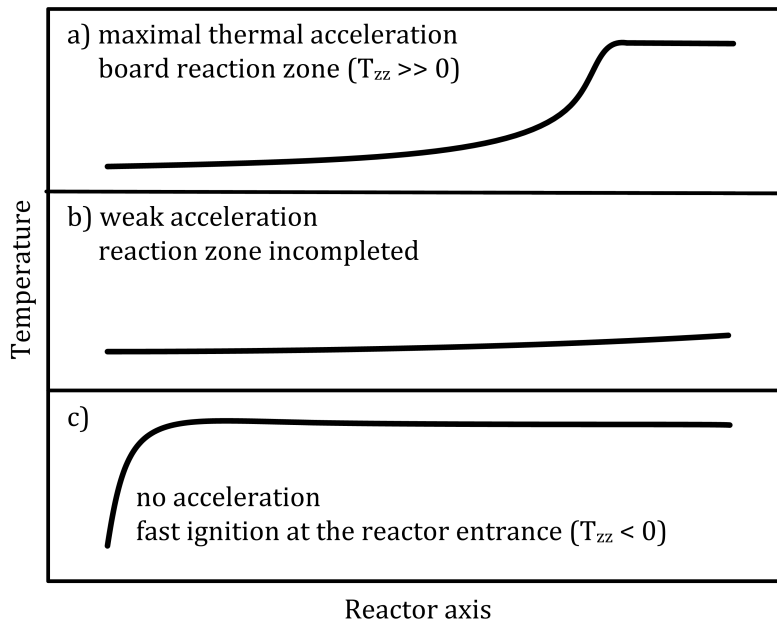


Figure 2.8: Steady-state axial temperature profiles with different degrees of thermal self-acceleration (Yakhnin et al. 2004).

of the bed, as well as the feed and cooling parameters, which mainly affect the length of the reaction zone (L_{rct}). Furthermore Pe^* can be influenced by the particle size, but larger catalyst particles reduce the effectiveness factor. Another approach to stabilize adiabatic fixed-bed reactors is the choice of a multi-bed reactor with interstage cooling.

Numerous other runaway criteria for fixed-bed reactors can be found in literature. However, their communicability is limited (Eigenberger et al. 2012), due to the peculiarities involving individual design configurations (such as tube diameters) being rarely taken into account.

2.3.4 Influence of product recirculation

Fixed-bed reactors can be designed with a recirculation of heat, mass, or with both (Li et al. 2013). A heat recirculation is integrated when the cold inlet stream is heated up by the hot outlet stream of the reactor. The recycle of mass is applied when the product gas is partially recycled, which is often combined with a separation of product components (Jones et al. 1998). The recycle of unreacted educts allow increasing the overall conversion. Gilles (1968) showed that the recirculation of an unreacted component could lead to a dynamic unstable behaviour despite constant input parameters, because the recycle of the educts results in higher reaction rates and thus higher reactor temperatures. Simultaneously, the product recirculation cools the reactor and limits the self-acceleration of the exothermic reaction. Additionally, the external recirculation causes a re-injection of the above described dynamic phenomena, namely **circulating waves** (Sheintuch et al. 2004) or **sustained**

moving hot-spots (Yakhnin et al. 2004). A stability analysis by Yakhnin et al. (1995a) showed that the re-injection of amplified perturbation can be unstable depending on the degree of recycling and on the differential flow.

2.4 Unsteady operation of the methanation

Solid catalysts are labile components and they are sensitive to the variation of fluid conditions (Boreskov et al. 1983). Thus, “it is possible to attain such a state, composition, and structure that would allow a noticeable increase in the selectivity and productivity of a process” (Boreskov et al. 1983). Recently, Kalz et al. (2017) underlined again the importance of understanding the heterogeneously catalysed reaction under dynamic conditions due to the dynamic structure of the catalyst. On the reactor scale, temperature and product distribution can be optimized by the modulation of the input parameters (Bunimovich et al. 2008). Therefore, Stankiewicz et al. (1995) suggested to develop reliable models for a deeper understanding of unsteady-state processes and to analyse the dynamic catalyst’s behaviour. The literature already focusing on the unsteady-state operation of the methanation is firstly presented on a catalyst scale, mainly for Ni/Al₂O₃ catalyst (subsection 2.4.1) and secondly, on a reactor scale in the case of fixed-bed reactors (subsection 2.4.2).

2.4.1 Catalyst scale

The most comprehensive research for the CO₂ methanation of Ni/Al₂O₃ under unsteady-state feed compositions was performed by Mutz et al. focusing on deactivation processes. The oxidation of Ni in a pure carbon dioxide environment was investigated (Mutz et al. 2016; Mutz et al. 2015, 2017) which should be prevented, since inactive NiO and Ni₃O₄ were formed. The initial reduced state could only be reached by the reactivation with hydrogen, and not in the stoichiometric reaction medium. Therefore, the reactor should be kept in a reducing atmosphere, or purged with inert gas during the stand-by operation. Additional to the oxidation of Ni, carbon can deposit on the catalyst limiting the catalytic activity. This case occurred only when pure methane was fed to the reactor, but not for mixtures of methane with H₂ and CO₂, or pure carbon dioxide (Mutz et al. 2018). Thus, the industrial methanation can be applied with biogas in the feed and with the recirculation of product gas.

Furthermore, unsteady-state catalyst experiments can be used for mechanistic studies as done by Marwood et al. for the CO₂ methanation on Ru/TiO₂ and on Ru/Al₂O₃ (Marwood et al. 1994a, 1996, 1997, 1994b). Klusáček et al. (1995) and Stuchly et al. (1993) and Friedland et al. (2016, 2017) investigated the storage behaviour of different reaction intermediates on Ni/SiO₂ and on Ni/Al₂O₃, respectively, for the CO methanation. CO blocks the adsorption of H₂ leading to an increased time-average reaction rate if CO-rich

and CO-lean mixtures are switched periodically, since carbonaceous reaction intermediates stored at the surface can be hydrogenated (Klusáček et al. 1995; Stuchly et al. 1993).

2.4.2 Reactor scale for fixed-bed reactors

Without product recirculation: The unsteady-state methanation was initially investigated by Doesburg et al. (1976a,b). The authors studied disturbances of the feed temperature and concentration for binary (H_2 and either CO or CO_2) as well as ternary (H_2 , CO, and CO_2) inlet gas mixtures. The results comprise the inhibition of the carbon dioxide methanation in the presence of carbon monoxide and a fast responding concentration compared to a slow temperature response. In addition, the wrong-way behaviour was discussed. Güttel (2013) simulated the periodic operation of the carbon monoxide methanation. In the study, the inlet composition was varied between stoichiometric and equimolar cases. A self-stabilizing system behaviour, also called relaxed steady-states (Kreitz et al. 2018; Meyer et al. 2017), was observed for high switching frequencies. Additionally, the dynamics of methanation reactors under model conditions were researched by Friedland et al. (2016) and Meyer et al. (2017). Further unsteady-state scenarios were exemplary simulated for biogas-upgrading with electrolytically-produced hydrogen (Jürgensen et al. 2015), for SNG production of coal syngas (Dissinger et al. 1980) and for life-support-systems using metabolic carbon dioxide in a space station (Lunde 1974).

Bremer et al. (2017) optimized the start-up behaviour of the CO_2 methanation in a cooled fixed-bed reactor, which was controlled by the cooling temperature of the reactor jacket. On the basis of a 2D reactor model the authors proved the feasibility that the reactor is controllable during unsteady-state operation. Additionally, it was pointed out that multiple steady states (Lee et al. 1987) have to be considered. Furthermore, the existence of a bistability region for the ignition and extinction of the exothermic methanation reaction in a cooled fixed-bed reactor was reported, which is characterized by a hysteresis between the ignition and extinction temperature of approximately 20 K (Sun et al. (2017b), cf. parametric sensitivity in subsection 2.3.2). Bremer et al. (2017) discussed reactor control strategies to operate at the unstable working point for a cooled methanation reactor requiring very fast changes of the coolant temperature.

The dynamics of cooled fixed-bed reactors for the CO_2 methanation were investigated either on the basis of a one-dimensional, pseudohomogeneous model using Matlab (Sun et al. 2017a,b) or a two-dimensional, heterogeneous one using COMSOL (Try et al. 2018) both including axial mass and heat dispersion. These simulation studies show that dynamic phenomena have to be considered for the methanation, as presented for generic cases in exothermic fixed-bed reactors by Yakhnin et al. (2004). For example, Sun et al. (2017a) demonstrated moving thermal fronts propagating upstream in the reactor after a stepwise increase of the inlet temperature by 40 K and vice-versa for an inlet temperature decrease by 60 K. Try et al. (2018) investigated steps of the inlet temperature (up to ± 20 K) and

detected the wrong-way behaviour comparable to findings of Doesburg et al. (1976a). Also, the formation of travelling hot-spots for a decrease of the coolant temperature by 20 K is reported, which also occurred for a pressure decrease at the reactor inlet of 0.15 MPa. Flow rate steps led to overshooting of the maximal gas temperature for a positive step and undershooting for a negative step. Rönsch et al. (2017) analysed the cool-down behaviour of an isolated fixed-bed reactor, which was purged with nitrogen and closed to stop the convection. The simulated reactor was able to store sufficient heat to allow a warm start after 4 h in the stand-by mode.

With product recirculation: Rönsch et al. (2014) showed that a disproportional adaptation of the recycle flow-rate is required to prevent the overheating of an adiabatic fixed-bed reactor. The results are in agreement with the experiences of the ADAM I pilot plant (Harms et al. 1980), where SNG is produced by the TREMP process consisting of three adiabatic fixed-bed reactors with intermediate cooling and a product recirculation after the first reactor. Harms et al. (1980) found out that unexpected process disturbances and the load changes of the syngas from 100 to 50 % could be handled by an extensive process control system at the TREMP process. Li et al. (2013) analysed the stability of a cooled fixed-bed reactor with mass recycle via the recirculation of product gas and heat recycle by preheating the coke oven gas upstream the methanation. The reactor system needed approximately 1 h to reach a new steady-state reactor temperature, if the inlet molar fraction of carbon monoxide was varied stepwise up to 2 mol% only. Additionally, the authors used a linearised simulation model to prove that the system stability is lowered by the recirculation of heat, mass, or both at the same time.

Especially, in the recent literature, various aspects of the unsteady-state methanation were investigated, but a comprehensive analysis of the load flexibility and the process control by product recirculation is missing thus far. The unsteady-state operation in fixed-bed reactors with and without product recirculation was examined for other synthesis reactions, like Fischer-Tropsch (Iglesias González et al. 2016a) or methanol synthesis (Abrol et al. 2012; Shahrokhi et al. 2005).

3 Modelling and simulation

The fixed-bed recycle reactor (FBRR) consists of the fixed-bed reactor, the product recirculation, and the gas mixing (Figure 3.1). At the system inlet, the inlet gas containing hydrogen and carbon dioxide is supplied and mixed with the recycle stream. The mixed gas is fed into the fixed-bed reactor. The product gas stream at the reactor outlet is split in the recycle stream and the outlet stream without considering product separation. A deterministic continuum model (cf. subsection 2.2) was deduced for the fixed-bed reactor as explained in section 3.1 and appendix B. Following, the implementation and the numerical solution with MATLAB is described (section 3.2). At the end of this chapter the simulation parameters are summarized in section 3.3.

3.1 Dynamic reactor model

The fixed-bed reactor is described by a one-dimensional, pseudohomogeneous model, considering the catalyst and reactor wall as well as gas-phase containing the components $i = \text{H}_2, \text{CO}_2, \text{CO}, \text{CH}_4, \text{H}_2\text{O}, \text{N}_2$. Ideal gas behaviour and plug-flow are assumed. The catalyst bed is formed by spherical, isothermal particles with uniform size d_c and constant bulk porosity over the whole reactor ε_{bed} . The diffusion limitations inside the catalyst particle are evaluated via constant activity factors. This simplification is reasoned by the reduction in computation time by one order of magnitude and only minor differences among different model complexities. Wesenberg et al. (2007) have shown that a heterogeneous, a pseudohomogeneous model with a variable effectiveness factor, and a pseudohomogeneous model with a constant activity factor deliver approximatively the same results for steam reforming (the reverse reaction of the methanation). This simplification induces imprecisions for an extensive hot-spot formation in the catalyst bed, since the effectiveness factor decreases significantly for high catalyst temperatures (Schlereth et al. 2014). As presented in appendix B.4, the influence of the effectiveness factor depending on gas temperature and composition over the reactor length is illustrated, supporting the assumption of a constant activity factor. The heat capacity c_p and the density ρ of the solid phases (catalyst and reactor wall) are assumed to be independent of the temperature. According to the Anderson criteria (cf. section A.2), it can be simplified that the catalyst particles are isothermal inside. The axial dispersion was neglected in the plug-flow model as proven by the Mears' criterion (Mears 1971). The suitability of a one-dimensional model, i.e. absence

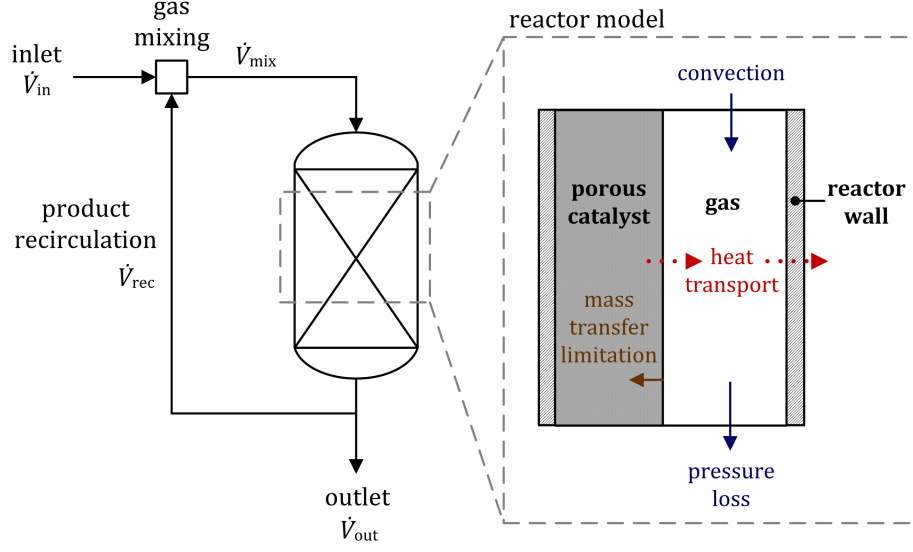


Figure 3.1: Fixed-bed recycle reactor (FBRR) including a schematic drawing of the reactor model.

of radial gradients, was proven in literature for comparable conditions (Parlikkad et al. 2013; Schlereth et al. 2014).

The material balance (Eq. 3.1) and the energy balances (Eqs. 3.3–3.5) are summarized in the following. While the material balance bases on a homogeneous approach, the separate consideration of the phases in energy balances allows for the investigation of different heat-storage-capacities effects on the reactor dynamics (Adler 2000a). The reactor cooling is simplified by a constant heat transfer coefficient between gas phase and coolant h_{wa} and a constant temperature of the cooling medium T_a . For the simulation, the material balance is transferred to partial pressures p_i as the balance variable (Eq. 3.2).

Material balance:

$$\varepsilon_{bed} \frac{\partial c_i}{\partial t} = - \frac{\partial (u_s c_i)}{\partial z} + (1 - \varepsilon_{bed}) \cdot r_i \quad [\text{mol m}^{-3} \text{ s}^{-1}] \quad (3.1)$$

$$\text{with } r_i = \rho_c \sum_j (\eta_j \nu_{i,j} r_j)$$

$$\begin{aligned} \frac{\partial p_i}{\partial t} = & \frac{p_i}{T_g} \frac{\partial T_g}{\partial t} - \frac{p_i}{\varepsilon_{bed}} \frac{\partial u_s}{\partial z} - \frac{u_s}{\varepsilon_{bed}} \frac{\partial p_i}{\partial z} + \frac{u_s p_i}{T_g \varepsilon_{bed}} \frac{\partial T_g}{\partial z} \\ & + \frac{(1 - \varepsilon_{bed})}{\varepsilon_{bed}} \rho_c r_i R T_g \quad [\text{Pa s}^{-1}] \end{aligned} \quad (3.2)$$

Energy balances of the phases: gas g , catalyst c and wall w [W m^{-3}]

$$\varepsilon_{bed} \frac{\partial(\rho_g c_{p,g} T_g)}{\partial t} = - \frac{\partial(u_s \rho_g c_{p,g} T_g)}{\partial z} - h_{gw} a_{v,wi} (T_g - T_w) + h_{gc} a_{v,gc} (T_c - T_g) \quad (3.3)$$

$$\rho_c c_{p,c} \frac{\partial T_c}{\partial t} = - \frac{h_{gc} a_{v,gc}}{1 - \varepsilon_{bed}} (T_c - T_g) + \rho_c \sum_j -\Delta_R H_j \eta_j r_j \quad (3.4)$$

$$\rho_w c_{p,w} \frac{\partial T_w}{\partial t} = \frac{h_{gw} a_{v,wi}}{\varepsilon_w} (T_g - T_w) - h_{wa} a_{v,wa} (T_w - T_a) \quad (3.5)$$

The superficial velocity of the gas phase u_s is calculated by the continuity equation (Eq. 3.6), where the reactor inlet ($z = 0$ m) is chosen for the reference conditions (index 0). The superficial velocity is changed by the non-equimolar reactions, the pressure loss, and the exothermic heat-up. It is confirmed by calculating the Mach number (Ma) that the fluid flow can be assumed as incompressible ($\partial u_s / \partial z = 0$), as derived in the appendix B.1. Furthermore, it is assumed that gradients of the gas properties density and heat capacity can be neglected. They are calculated for each space and time step with the state variables of the previous step. As a result, the balance equations of the gas phase can be simplified (Eqs. 3.7 and 3.8).

$$u_s(z) = u_{s,0} \frac{\rho_0}{\rho(z)} \quad (3.6)$$

$$\frac{\partial p_i}{\partial t} = \frac{p_i}{T_g} \frac{\partial T_g}{\partial t} - \frac{u_s}{\varepsilon_{bed}} \frac{\partial p_i}{\partial z} + \frac{u_s p_i}{T_g \varepsilon_{bed}} \frac{\partial T_g}{\partial z} + \frac{(1 - \varepsilon_{bed})}{\varepsilon_{bed}} \rho_c r_i R T_g \quad (3.7)$$

$$\varepsilon_{bed} \rho_g c_{p,g} \frac{\partial T_g}{\partial t} = -u_s \rho_g c_{p,g} \frac{\partial T_g}{\partial z} - h_{gw} a_{v,wi} (T_g - T_w) + h_{gc} a_{v,gc} (T_c - T_g) \quad (3.8)$$

The pressure loss is described by the Ergun equation (Eq. B.31, Ergun 1952) with the parametrisation of Hicks (1970). The selection of the parametrisation is explained in appendix B.2. The volume specific surface areas a_v and the volume fraction of the reactor wall ε_w are calculated according to Eq. 3.9 on the basis of reactor inner diameter d_r , catalyst particle diameter d_c , reactor wall thickness s , and bed porosity ε_{bed} .

$$a_{v,wi} = \frac{4}{d_r}; \quad a_{v,gc} = (1 - \varepsilon_{bed}) \frac{6}{d_c}; \quad a_{v,wa} = \frac{(d_r + 2s)}{s(d_r + s)}; \quad \varepsilon_w = \frac{4s(d_r + s)}{d_r^2} \quad (3.9)$$

The kinetics are taken from Koschany et al. for the methanation of CO_2 in a moderate temperature range (Eq. 3.10, Koschany et al. 2016), since it agrees well with the absence of significant reverse water-gas shift reaction activity observed in own experiments (chapter 6). The reaction rate constant was calculated by the Arrhenius equation (Eq. 3.11) and the adsorption constant by the van't Hoff equation (Eq. 3.12). The equilibrium constant was originally published by Aparicio (1997) (Eq. 3.13). The values for the kinetic parameters

Table 3.1: Parameters of the reaction rate by Koschany et al. (2016) ($T_{ref} = 555$ K).

| Parameter | Value | Unit |
|--|----------------------|---|
| Reaction rate coefficient of CO ₂ methanation | | |
| $k_{0,1}$ | $3.46 \cdot 10^{-4}$ | $\text{mol bar}^{-1} \text{g}_{cat}^{-1} \text{s}^{-1}$ |
| $E_{A,1}$ | 77.5 | kJ mol^{-1} |
| Adsorption constants | | |
| $K_{0,OH}$ | 0.5 | $\text{bar}^{-0.5}$ |
| $\Delta H_{Ads,OH}$ | 22.4 | kJ mol^{-1} |
| K_{0,H_2} | 0.44 | $\text{bar}^{-0.5}$ |
| $\Delta H_{Ads,H_2}$ | -6.2 | kJ mol^{-1} |
| $K_{0,mix}$ | 0.88 | $\text{bar}^{-0.5}$ |
| $\Delta H_{Ads,mix}$ | -10.0 | kJ mol^{-1} |

are summarized in Table 3.1. The calculation of all other model parameters is presented in appendix B.2.

$$r_{CO_2-Meth.} = \frac{k_1 p_{H_2}^{0.5} p_{CO_2}^{0.5} \left(1 - \frac{p_{CH_4} p_{H_2O}^2}{p_{CO_2} p_{H_2}^4 K_{eq,1}}\right)}{\left(1 + K_{OH} \frac{p_{H_2O}}{p_{H_2}^{0.5}} + K_{H_2} p_{H_2}^{0.5} + K_{mix} p_{CO_2}^{0.5}\right)^2} \quad (3.10)$$

$$k_j = k_{0,j} \exp \left[\frac{E_{A,j}}{R} \left(\frac{1}{T_{ref}} - \frac{1}{T} \right) \right] \quad (3.11)$$

$$K_i = k_{0,i} \exp \left[\frac{\Delta H_{Ads,i}}{R} \left(\frac{1}{T_{ref}} - \frac{1}{T} \right) \right] \quad (3.12)$$

$$K_{eq,1} = 137 \cdot T^{-3.998} \exp \left(-\frac{158.7 \text{ kJ mol}^{-1}}{R T} \right) \left[\text{bar}^{-2} \right] \quad (3.13)$$

The product recirculation is defined by two parameters: the recycle ratio and the residence time of the recycle stream (also denoted as time delay). The recycle ratio is defined by the ratio of the molar flow rates of the gas streams, in the recycle \dot{n}_{rec} and at the system inlet \dot{n}_{in} (Eq. 3.14 and Figure 3.1). The residence time in the recycle is caused by the included equipment, such as heat exchangers, pumps, and piping. It is set to zero, since a generic case focusing on the reactor is studied in this thesis, rather than one specific configuration. The negligence of the residence time leads to an instantaneous feedback of the concentration. Furthermore, the temperature of the recycle stream is set equal to the inlet stream temperature ($T_{rec} = T_{in} = T_{mix}$) neglecting the temperature feedback. Finally, no separation of a product gas component is performed prior to the recirculation.

$$Rec = \frac{\dot{n}_{rec}}{\dot{n}_{in}} \quad (3.14)$$

3.2 Implementation and numerical solution

The model of the FBRR is implemented in the software MATLAB (version: R2012a). The structure of the simulation program is shown Figure 3.2. At first, the parameters are defined. This comprises the definition of constant parameters (e. g. physical constants, constant material parameters, or polynomial coefficients to calculate the gas parameters) and variable parameters for the reactor and the process, which are often changed during the simulation. The parameters are collected in *structure arrays*, for example “var.” summarises all variables. This procedure allows structuring the MATLAB code and fast inserting varied parameter sets. Furthermore, the simulation parameters “simpar.” are determined including the definitions of the grid, the finite difference matrix and the Jacobi pattern. Based on the parameter definition, the ramps can be defined for the process parameter at the inlet, and the boundary conditions for all time steps “bc.” are specified. The model selection criteria can be calculated for a specific time step to prove the model assumptions (cf. subsection 2.2 and appendix A.2). In the next step, the initial conditions of the reactor are set-up. Therefore, different options are possible. For example the reactor can be purged with inert gas or the reactants, the temperature can respectively be set to a cold, warm, or hot start (cf. section 2.3.1), or the results of a previous simulation can be imported, if the number of axial grid points are equal. For the simulation routine, the model of the fixed-bed recycle reactor is solved temporally step-wise, which allows for the calculation of the gas mixing upstream the reactor and the definition of the boundary conditions at the reactor entrance $X(t^*, z=0)$ for each time step t^* . The solver calculated the reactor model including the space-dependent model parameters (as gas properties or reaction kinetics), and the balance equations. The results of the differential equation system for each time step $Y(t^*, z)$ are returned and afterwards, the pressure drop and the change of the velocity field is determined. Finally, time- and space-dependent results $Y(t, z)$ are plotted and saved.

The method of lines (MOL) is applied to solve the partial differential equations (PDEs) in two steps (Schiesser 1991). The spatial derivatives are approximated algebraically, and the resulting system is integrated in the initial value variable (time). For the first step, a five-point biased upwind differentiation is chosen (Eq. 3.15, Vande Wouwer et al. 2004), since it is useful for the approximation of strong convective terms due to their efficiency and stability by avoiding spurious oscillations (Vande Wouwer et al. 2004, 2005). For the second step, the ode15s solver is selected, due to it being a variable-step, variable-order (VSVO) solver¹ for stiff differential equations. A time step of 1 s and a maximal axial step of 0.01 m are chosen for the differentiation grid. The axial step-size is refined up to 0.0025 m for the dynamic simulations of load steps and ramps. The step-sizes are verified

¹<https://de.mathworks.com/help/matlab/ref/ode15s.html> (accessed 17.06.2018)

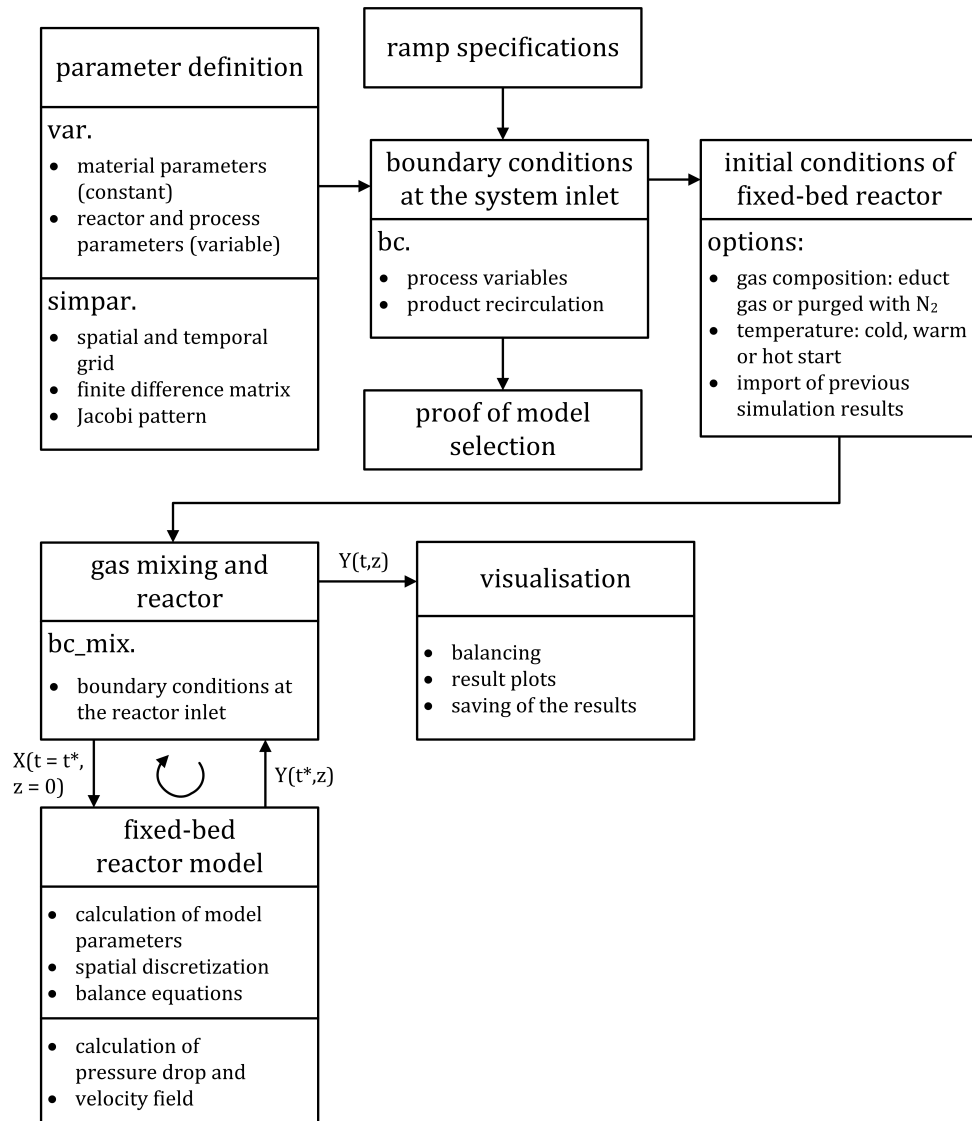


Figure 3.2: Structure of the simulation program for the fixed-bed recycle reactor.

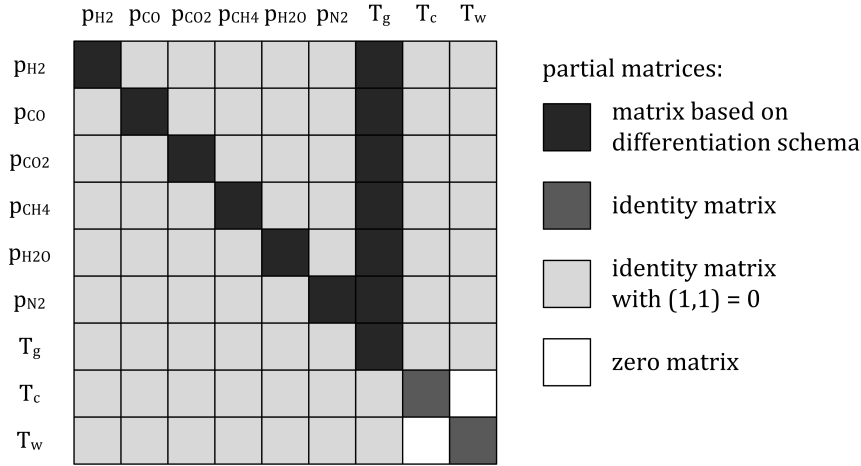


Figure 3.3: Jacobian pattern for all balance variables φ assembled by partial matrices.

in terms of computation time and negligible influence on the result accuracy. Due to the size limitations of MATLAB for saving the results in Excel files, the amount of axial steps has to be limited to 201.

$$\left. \frac{\partial \varphi}{\partial z} \right|_{z_i} = \frac{-\varphi(z_{i-3}) + 6\varphi(z_{i-2}) - 18\varphi(z_{i-1}) + 10\varphi(z_i) + 3\varphi(z_{i+1})}{12\Delta z} \quad (3.15)$$

The numerical simulation is accelerated by defining the Jacobian pattern of the PDE system, improving the solver efficiency. The Jacobian pattern is derived from the balance equations and contains a ‘one’ when the spatial derivation exists, resulting in a square matrix with the size of $m \times \sum \varphi$ (number of axial grid points multiplied by the number of balance variables). The pattern is shown in Fig. 3.3, with a partial matrix size of $m \times m$. The most complex partial matrix contains a ‘one’ where an entry in the differentiation scheme (Eq. 3.15) exists. Additionally, a ‘one’ is inserted in this matrix at the entry (3,3) and the entries in the first row from the second to the last column are set ‘zero’. The Jacobian pattern is compared to the numerically derived pattern by MATLAB.

3.3 Simulation parameters

The properties of the fixed-bed reactor, catalyst, and inlet stream used for simulation are summarized in Table 3.2. The process conditions represent a typical power-to-gas process. The chosen parameters aim for representing a pilot scale reactor and providing a basis of comparison between the adiabatic and the cooled reactor, simultaneously. The residence times are nearly similar in both reactors. These simulation parameters describe the base case, which is partially varied in the sensitivity analysis and as follows. For the

Table 3.2: Properties of the base case for the fixed-bed reactors, catalyst, and inlet stream.

| Parameter | Symbol | Value | Unit | Assumption |
|--|---------------------|----------------------|----------------------------------|--|
| Adiabatic reactor | | | | |
| length | L | 1 | m | const. inlet parameters |
| | | 0.5 | m | unsteady inlet parameters |
| diameter | d_r | $5 \cdot 10^{-2}$ | m | inner diameter |
| recycle ratio | Rec | 1 | – | |
| Cooled reactor | | | | |
| length | L | 2 | m | |
| diameter (inner) | d_r | $2.54 \cdot 10^{-2}$ | m | typical tube of a multitubular reactor |
| heat transfer coefficient | $h_{w,a}$ | 2000 | $\text{W m}^{-2} \text{K}^{-1}$ | molten-salt cooling, Schlereth et al. (2014) |
| cooling temperature | T_a | 290 | $^{\circ}\text{C}$ | |
| recycle ratio | Rec | 0 | – | |
| Reactor wall (steel 1.4301) for both reactors | | | | |
| wall thickness | s | $3 \cdot 10^{-3}$ | m | industrial pipe |
| heat capacity | $c_{p,w}$ | 560 | $\text{J kg}^{-1} \text{K}^{-1}$ | VDI D |
| density | ρ_w | 7980 | kg m^{-3} | VDI D |
| Catalyst | | | | |
| diameter | d_c | $3 \cdot 10^{-3}$ | m | Meth134 catalyst |
| bed porosity | ε_{bed} | 0.39 | – | for equal spheres, VDI M |
| heat capacity | $c_{p,c}$ | 1107 | $\text{J kg}^{-1} \text{K}^{-1}$ | Oliveira et al. (2010) |
| density | ρ_c | 1475 | kg m^{-3} | Meth134 catalyst |
| activity factor | η | 0.1 | – | Schlereth et al. (2014), Wesenberg et al. (2007) |
| Inlet conditions | | | | |
| volumetric flow rate | \dot{V}_{in} | 10 | $\text{m}^3 \text{h}^{-1}$ (STP) | |
| temperature | T_{in} | 280 | $^{\circ}\text{C}$ | Try et al. (2018) |
| pressure | p | $15 \cdot 10^5$ | Pa | typical for PtG process |
| molar ratio | y_{H_2}/y_{CO_2} | 4 | – | stoichiometric |
| dilution | y_{N_2} | 0.75 | – | if $Rec = 0$ during adiabatic operation |
| | y_{N_2} | 0 | – | otherwise |

VDI – (Verein Deutscher Ingenieure 2006), with chapter names

simulations with unsteady-state inlet parameters, the adiabatic reactor length was reduced to 0.5 m, since a finer axial step-size was required and the chemical equilibrium had already been reached in the first fifth of the reactor (cf. Fig. 5.1). The inlet gas was diluted with nitrogen to limit the temperature increase, if no gas was recycled in the adiabatic case.

4 Experimental methods

Two experimental series were conducted for the validation of the simulation results with different nickel catalysts and reactors as described in detail in section 4.1. Furthermore, the set-up of the synthesis test facility, the gas analysis devices (section 4.2), and the experimental procedure (section 4.3) is presented. At last, the results evaluation is explained in section 4.4.

4.1 Experimental set-up

Catalysts

For the first experimental series, the commercial catalyst Meth134, 20Ni/5CaO/75Al₂O₃, was used. This catalyst was manufactured by C&CS (Clariant) as spherical pellets with a diameter range of 3–6 mm and a bulk density of 900 kg m⁻³. Meth134 contains CaO as a structural promoter increasing the dispersion of Ni and stabilizing it against sintering, without influencing the conversion of carbon dioxide or the selectivity to methane (Su et al. 2016). The temperature of the Meth134 catalyst should be limited to 510 °C for long term operation and to 700 °C for short term operation. 1 g of the ground and sieved fraction of 0.5 to 1.0 mm was utilized undiluted for the first experimental series. For the second experimental series, 16.96 g of a non-commercial 5 wt% Ni-catalyst was used, allowing its operation with undiluted inlet gas due to the decreased nickel content. Its preparation procedure is described in appendix C.2, which was conducted by Jens Friedland at Ulm University. The non-commercial catalyst is supported on Al₂O₃ spheres with a bulk density of 790 kg m⁻³, but with a lower average diameter of 820 μm in comparison to the Meth134, making crushing unnecessary. The composition determined by an analysis of major and minor elements as well as the results of the physical adsorption measurement for both catalysts are summarized in Table 4.1.

To reduce the nickel oxide, the catalysts were activated with an inlet gas composition of 10 vol% H₂ in N₂ and a constant flow rate of 1 L min⁻¹ (STP). Thereby, the fixed-bed was heated up to 480 °C with a ramp of 3 K min⁻¹ and held isothermal for another 4 h. An activation temperature of 480 °C allows the reduction of Ni₂O₃, α- and β₁-NiO, which prevents a further activation during operation (Schlüter et al. 2017). After the activation, the reactor was kept inert by purging with nitrogen. In a continuous test for more than

Table 4.1: Catalyst characterisation by an analysis of major and minor elements as well as BET measurement.

| Parameter | Unit | Meth134 0.5–1 mm | 5 wt% Ni-catalyst |
|---------------------------------|-----------------------------|---------------------|-------------------|
| Ni content | wt% | 18.0 | 4.89 |
| Al content | wt% | 19.1 | 52.3 |
| Ca content | wt% | 2.04 | 0 |
| BET surface A_{BET} | $\text{m}^2 \text{g}^{-1}$ | 86.1 | 168.3 |
| total pore volume $V_{p,total}$ | $\text{cm}^3 \text{g}^{-1}$ | 0.27 | 0.44 |
| average pore diameter d_p | nm | 12.4 | 9.4 |

8 h, the stability of the catalytic activity was confirmed by constant outlet concentrations as well as a constant temperature profile in the reactor of both catalysts.

Reactor designs and fixed-bed arrangements

The experiments were conducted with two different reactor designs shown in appendix C.1. In the first experimental series, an axial moveable thermocouple with a protection tube (outer diameter of 3 mm) was placed in the centre of the reactor (internal diameter of 13 mm). The axial position of the thermocouple is specified along the gas-flow direction through the fixed-bed with a value of zero at the beginning of the catalytic bed according to the drawing (appendix C.1). The undiluted catalyst bed of the commercial Meth134 catalyst had a height of 1.2 cm and was placed 14.2 cm downstream the reactor inlet to allow for sufficient gas pre-heating in this reactor design. In the second experimental series, a multiple-thermocouple arrangement with a protection-tube (outer diameter 6 mm) was placed in the centre of a larger reactor (internal diameter 18 mm). The first measurement point of the multiple-thermocouple was located 15 mm upstream the catalyst bed. Seven measurement points were placed in the catalyst bed at $z = 0, 5, 10, 15, 30, 45, 75$ mm and two measurement points followed downstream at $z = 105$ and 125 mm. The undiluted catalyst bed of the non-commercial 5 wt% Ni-catalyst had a height of 10 mm in this reactor design. Aluminium oxide with a particle diameter of 1 to 3 mm was used as inert material. A blank experiment with inert material only was performed to rule out blind activity of the system.

Synthesis test facility

Figure 4.1 shows the lab-scale test facility, as well as the measured (white background) and controlled (grey background) process variables. A detailed process flow sheet is presented in appendix C.1. The inlet gas mixture (N_2 , H_2 and CO_2) was generated by mass-flow controllers (El-Flow[®] from Bronkhorst) having an average precision of ± 0.9 %.

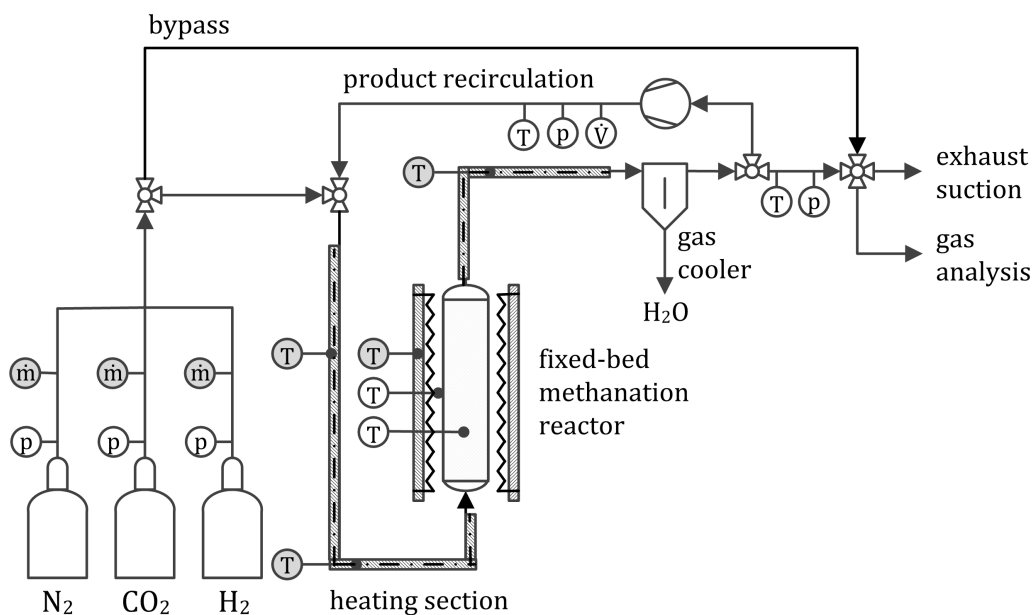


Figure 4.1: Flow sheet of the lab-scale test facility with the evaluated process values.

Subsequently, the educt gas was pre-heated between 220 and 300 °C prior to entering the reactor, which was heated by a split-tube furnace (VST 200/ E301 from Carbolite). Downstream the methanation reactor, water was separated from the gas stream in a gas cooler at a temperature of 3 °C (SCC-C from ABB Automation). The product gas was partially recycled by a compressor (HMZ 030 from K-Engineering). The recycle flow rate was determined by a volumetric flow meter (vane wheel FA Di 9.7 from Höntzsch) calibrated with nitrogen. The bypass allowed the direct analysis of the feed-gas composition without passing the reactor.

4.2 Analytics and LabVIEW control program

In the first experimental series, the dry product-gas stream was analysed by a micro gas-chromatograph (GCM[®] Micro-Box II from Elster, μ GC) with a column for permanent gases (Carbosphere HT) and a thermal conductivity detector. The analysis method started at 50 °C and carried out a temperature ramp of 3 °C s⁻¹ up to 280 °C. The concentrations of N₂, H₂, CO₂, CO, and CH₄ of the dry gas were detected, and argon was used as an internal standard. The calibration of the μ GC was daily verified by five test gas measurements¹. The time for a measurement cycle of 4 min \pm 3 s limited the detection precision for steep inlet gradients. The uncertainties of the μ GC results are in a range of \pm 0.5 vol%.

¹composition of the test gas: 34.96 vol% N₂, 19.02 vol% H₂, 15.00 vol% CO₂, 20.00 vol% CO, 5.01 vol% CH₄, 3.01 vol% C₂H₆, and 3.01 vol% C₂H₄.

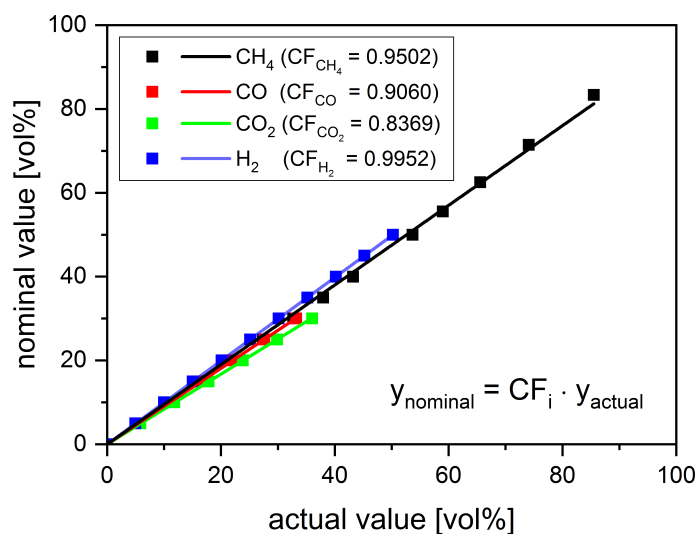


Figure 4.2: Determined correction factors CF_i for the continuous gas-analyser EasyLine EL3020 from ABB.

Furthermore, a continuous gas-analyser (EasyLine EL3020 from ABB) was installed for the second experimental series. This analyser contained an infrared photometer (Uras26) for the measurement of the infrared-active gas components (CO_2 , CO , and CH_4) and a thermal conductivity analyser for the measurement of binary gas-mixtures with different thermal conductivity (H_2 in N_2). The response time was lower than 2 s. All gas components were measurable from 0 vol% and to the upper measurement limits of 30 vol% for CO_2 and CO , 80 vol% for CH_4 , and 100 vol% for H_2 . The uncertainties of the results were lower than 0.5 % of the span for Uras26 analyser and 1 % of the span for Caldos27 analyser, respectively. The continuous gas-analyser was calibrated daily using pure gas streams of N_2 and H_2 with 500 mL min^{-1} . Two internal testing cuvettes for CO_2 and CO in combination as well as for CH_4 have simplified the calibration. Both gas analysers in the continuous gas-analyser had cross-sensitivities reduced by correction factors. Therefore, the measurement range for each gas was systematically scanned in steps of 50 mL min^{-1} and 100 mL min^{-1} for CH_4 , respectively. Figure 4.2 shows the resulting correction factors. The applicability of the correction factors was validated by the measurement of various gas mixtures (Table 4.2).

The entire test facility was controlled with a LabVIEW program (LabVIEW 2014 from National InstrumentsTM), which logged the data and allowed the definition of a recipe as a series of set points for the unsteady-state experiments. This schedule allowed specifying the set points of mass-flow controllers, back pressure regulator, and the recycling compressor. The set-points were updated every 2 s for the faster load changes with a ramp time up to 2 min and every 15 s for slower load changes, respectively. The mass-flow controllers,

Table 4.2: Application of correction factors CF_i on various gas mixtures for the continuous gas-analyser with $y_{i,corr} = CF_i \cdot y_{i,act}$.

| Number | Value | N ₂ | H ₂ | CO ₂ | CH ₄ | CO | Error amount |
|--------|--------------|----------------|----------------|-----------------|-----------------|------|---------------------------------------|
| | | | | [vol%] | | | $\sum_i y_{i,nom} - y_{i,act/corr} $ |
| 1 | $y_{i,nom}$ | 0.0 | 80.0 | 20.0 | 0.0 | 0.0 | |
| | $y_{i,act}$ | -3.7 | 80.6 | 23.1 | 0.0 | 0.0 | 7.4 |
| | $y_{i,corr}$ | 0.5 | 80.2 | 19.4 | 0.0 | 0.0 | 1.3 |
| 2 | $y_{i,nom}$ | 28.6 | 57.1 | 14.3 | 0.0 | 0.0 | |
| | $y_{i,act}$ | 25.4 | 57.7 | 16.8 | 0.0 | 0.0 | 6.3 |
| | $y_{i,corr}$ | 28.5 | 57.4 | 14.1 | 0.0 | 0.0 | 0.6 |
| 3 | $y_{i,nom}$ | 54.5 | 36.4 | 9.1 | 0.0 | 0.0 | |
| | $y_{i,act}$ | 52.6 | 36.7 | 10.7 | 0.0 | 0.0 | 4.0 |
| | $y_{i,corr}$ | 54.5 | 36.5 | 9.0 | 0.0 | 0.0 | 0.4 |
| 4 | $y_{i,nom}$ | 0.0 | 14.3 | 14.3 | 57.1 | 14.3 | |
| | $y_{i,act}$ | -5.3 | 14.0 | 16.0 | 60.5 | 14.8 | 11.1 |
| | $y_{i,corr}$ | 1.8 | 13.9 | 13.4 | 57.5 | 13.4 | 4.3 |

nom – nominal, *act* – actual, *corr* – corrected

which communicated via the Flow-Bus system, were able to follow these fast set point changes with a minimal time delay (Figure 4.3).

4.3 Experimental procedure

To summarize, the first experimental series were conducted with the Meth134 catalyst in a short fixed-bed bed with a moveable thermocouple in the middle and with a discontinuous gas analysis by the μ GC. The second experimental series was carried out with the non-commercial 5 wt% Ni-catalyst, arranged in a longer fixed-bed with a multiple-thermocouple arrangement for the axial temperature measurement and the continuous gas-analyser. Nevertheless, the experimental procedure for both experimental series was similar and provided a distinction between the operation with constant inlet parameters and dynamic inlet parameters.

For steady-state experiments with constant inlet parameters, the inert reactor was heated up to a catalytic bed temperature of 280–300 °C without gas flow. The furnace set point temperature was not changed during the experiment. Afterwards, the inlet gas with stoichiometric composition ($y_{H_2}/y_{CO_2} = 4$) was continuously fed to the reactor. For the different experiments, the inlet flow rate was varied between 0.5 and 2.50 L min⁻¹ (STP). 40 minutes were necessary to obtain steady-state conditions with a constant temperature

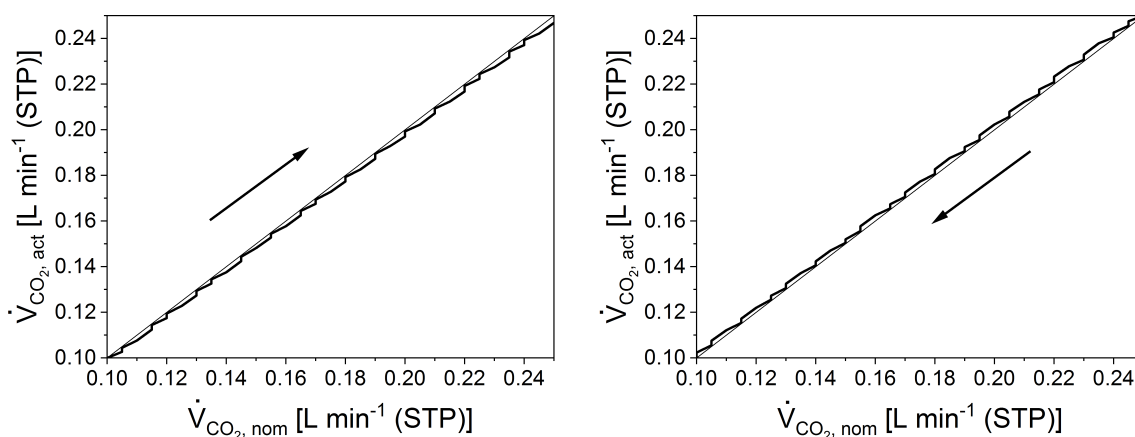


Figure 4.3: Comparison between the nominal (*nom*) and the actual (*act*) value of the CO_2 mass-flow controller tracked every second during the load ramp between $0.1 - 0.4 \text{ L min}^{-1}$ within 60 s; increase (left) and reduction (right).

profile in the fixed-bed and a constant outlet gas composition. The steady state was kept for another 50 minutes, before the reactor was purged with nitrogen.

The transient variation during the unsteady-state experiments was started after the methanation reaction had reached the steady state. After the load change, the inlet parameters were kept constant again until the new steady state was achieved. To synchronize the unsteady load change with the μGC measurement cycle, the ramps were started after the μGC pump took a gas sample. Therefore, the first sample was taken 3.5 min after the ramp was started, and the subsequent ones every 4 min. The moveable thermocouple was positioned at the hottest point of the fixed-bed, which was measured at the steady state before the ramp was started. A comparable synchronisation was not required for the unsteady-state experiments with continuous gas-analyser.

For experiments with product recirculation the aim was to generate a stable recirculation by controlling the voltage of the compressor. Thus, the steady-state experiments were conducted amongst others to determine operation points for the unsteady experiments. On the one hand, if the compressor voltage was insufficient, the reactor temperature and the product gas composition would have strongly varied and a steady state could not have been reached. On the other hand, had the compressor voltage been set too high, the conversion would subsequently have decreased, since the methanation reaction was limited by the kinetics.

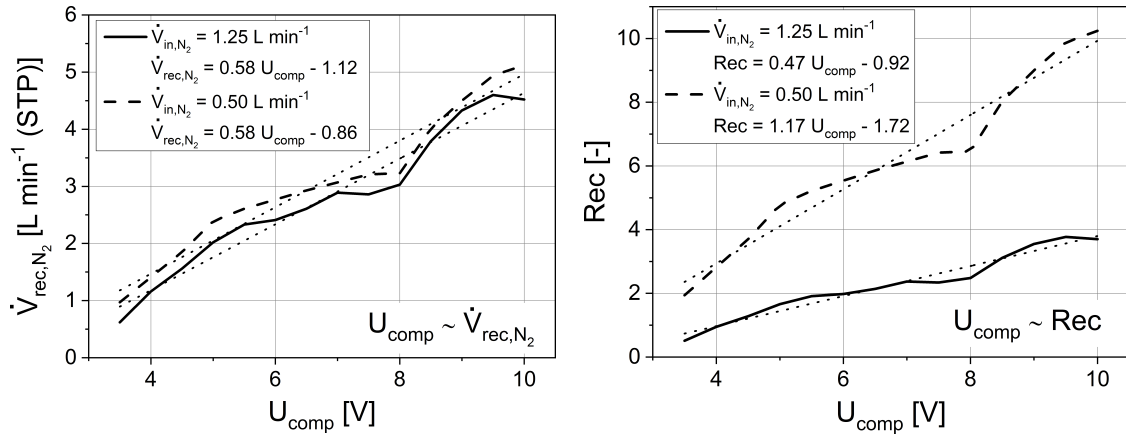


Figure 4.4: Determining the volumetric flow rate of the product recirculation \dot{V}_{rec} (left) and the recycle ratio Rec (right) with nitrogen in dependency of the compressor voltage U_{comp} for the second experimental series.

4.4 Results evaluation

For the evaluation of the experimental results, it was important to determine the recycle ratio, the mass balance of the involved components, and the further parameters for the unsteady-state experiments.

Determination of the recycle ratio

Additionally to the flow meter in the product recirculation, the flow rate of the recycle \dot{V}_{rec} was determined with pure nitrogen. Therefore, an additional mass-flow meter was installed directly behind the gas cooler for measuring the volumetric flow rate of the mixed stream \dot{V}_{mix} . Furthermore, the lab-scale test facility was heated-up and the reactor was filled equal to the experimental settings. According to Eq. 4.1 the flow rate in the recycle was measured in dependence of the inlet flow rate \dot{V}_{in} and the compressor voltage U_{comp} used in the experiments. The results for the second experimental series are shown in Figure 4.4 allowing a rough estimation of the recycle ratio.

$$\dot{V}_{rec} = \dot{V}_{mix} - \dot{V}_{in} \quad (4.1)$$

Balancing of the experimental results

The outlet flow rates of all components were calculated with the material balance, whereas the molar flow rate of nitrogen as an inert component was assumed to be constant at the system inlet and outlet ($\dot{n}_{N_2,in} = \dot{n}_{N_2,out}$). If the educt gases were supplied undiluted, the

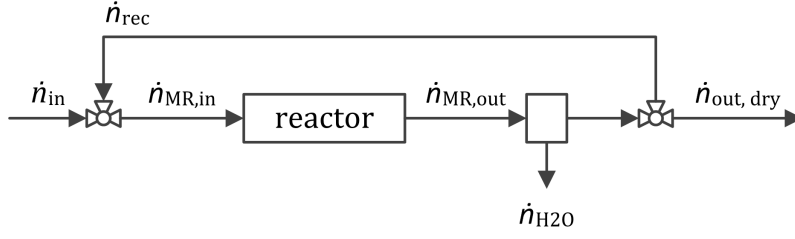


Figure 4.5: Stream names of the fixed-bed reactor concept with product recirculation (*MR* – methanation reactor).

molar flow rate of the dry product gas was calculated by the carbon balance (Eq. 4.2). The ratio of the molar flow rates of the dry product gas $\dot{n}_{out,dry}$ and inlet gas \dot{n}_{in} is designated as volume-reduction factor VF (Eq. 4.3). Assuming that no carbon deposits on the catalyst and that water is separated only in the condensation trap, the volume-reduction factor can be calculated according to Equation 4.4 proven by the stoichiometric analysis with respect to the key components (appendix C.3). The indices ‘*in*’ and ‘*out*’ refer to the inlet and outlet of the system as illustrated at Fig. 4.5. The inlet stream and outlet stream of the methanation reactor are indexed additionally with ‘*MR*’. All gas components are simplified as ideal gases. The effective residence-time of the gas in the catalytic fixed-bed $\bar{t}_{bed,eff}$ was defined by Eq. 4.5.

$$0 = \dot{n}_{CO_2,in} - \dot{n}_{CO_2,out} - \dot{n}_{out,dry} (y_{CH_4,out,dry} + y_{CO,out,dry}) \quad (4.2)$$

$$VF = \frac{\dot{n}_{out,dry}}{\dot{n}_{in}} \quad (4.3)$$

$$VF = \frac{y_{CO_2,in}}{y_{CH_4,out,dry} + y_{CO,out,dry} + y_{CO_2,out,dry}} \quad (4.4)$$

$$\bar{t}_{bed,eff} = \frac{V_{bed,void}}{\dot{V}_{MR,in}(\bar{T}_{bed}, p)} \quad (4.5)$$

$$(4.6)$$

The overall (external) carbon dioxide conversion X_{CO_2} and methane yield $Y_{CH_4,(CO_2)}$ are determined with the substance-specific molar flow rates \dot{n}_i at the inlet and outlet of the system (Eqs. 4.7 and 4.8). In contrast, the internal conversion per pass $X_{i,int}$ can be calculated by Eq. 4.9.

$$X_{CO_2} = \frac{\dot{n}_{CO_2,in} - \dot{n}_{CO_2,out}}{\dot{n}_{CO_2,in}} \quad (4.7)$$

$$Y_{CH_4,(CO_2)} = \frac{\dot{n}_{CH_4,out} - \dot{n}_{CH_4,in}}{\dot{n}_{CO_2,in}} \cdot \frac{|\nu_{CO_2}|}{\nu_{CH_4}} \quad (4.8)$$

$$X_{i,int} = \frac{\dot{n}_{i,MR,in} - \dot{n}_{i,MR,out}}{\dot{n}_{i,MR,in}} \quad (4.9)$$

Unsteady-state experiments

The ramp time t_{ramp} defines the time in which the load is varied from the start ($t = 0$ s) to the end of the ramp. For the unsteady-state experiments, the time scale t was normalized with ramp time t_{ramp} (Eq. 4.10). Thus, in order to improve the comparability of the results, all ramps start at a normalized time of 0 and end at a normalized time of 1, independent of the gradient. The gradient of linear load ramps, called load change velocity $v_{\dot{V}}$, is calculated by dividing the difference of the inlet volumetric flow rate before and after the ramp $\Delta \dot{V}_{in}$ by the ramp time (Eq. 4.11).

$$t_{norm} = \frac{t}{t_{ramp}} \quad (4.10)$$

$$v_{\dot{V}} = \frac{\Delta \dot{V}_{in}}{t_{ramp}} \quad (4.11)$$

For the experiments with unsteady-state inlet parameters, an experiment-specific dead-time t_d was determined to quantify the temporal shift between change at the inlet molar and the corresponding response at the outlet. Therefore, the time difference between the start of the educt gas at the mass flow controllers and the first detection of CO_2 at the continuous gas-analyser was used (Eq. 4.12). Correspondingly, the calculation of the volume-reduction factor was adapted (Eqs. 4.13 and 4.14).

$$t_d = |t_{start,ed} - t_{det,CO_2}| \quad (4.12)$$

$$VF(t) = \frac{\dot{n}_{out,dry}(t)}{\dot{n}_{in}(t - t_d)} \quad (4.13)$$

$$VF(t) = \frac{y_{CO_2,in}(t - t_d)}{y_{CH_4,out,dry}(t) + y_{CO,out,dry}(t) + y_{CO_2,out,dry}(t)} \quad (4.14)$$

5 Simulation results and discussion

The simulation results presented in this chapter are based on the dynamic model of the fixed-bed recycle reactor and the simulation parameters, which are described in chapter 3.

5.1 Sensitivity analysis to determine the load flexibility

The sensitivity analysis is used to determine the load flexibility of the adiabatic reactor with a constant recycle ratio ($Rec = 1$) and for the cooled reactor without product recycle. The aim is to present and to compare the influence of the reactor cooling in the load flexibility. Therefore, the axial profiles of the steady states are analysed focusing on the base case (subsection 5.1.1) and the variation of the inlet parameters (subsection 5.1.2). The inlet parameters were varied for both reactor types to provide a basis of understanding needed for the investigation of dynamic changes of the inlet stream (section 5.2). The influence of the recycle ratio on the load range is analysed in subsection 5.3.1. For the sensitivity analysis, a warm start was performed for each parameter change during simulations.

5.1.1 Steady-state behaviour (base case)

The steady-state axial profiles for the adiabatic reactor with a constant recycle ratio ($Rec = 1$) and the cooled reactor without product recycle are presented in Fig. 5.1. The adiabatic reactor shows a steep increase in temperature and methane fraction. The chemical equilibrium is reached within the first fifth of the reactor, which is denoted as reaction zone being highlighted by the grey-marked area. Downstream from this position, the reactor behaviour is stable. This means that the outlet conditions under dynamic operation can easily be predicted on the basis of thermodynamics. For instance, the equilibrium state only depends on the adiabatic temperature rise in a first-order approximation, which is independent of the volumetric flow rate. In principle, this offers a broad range of flow rates and thus a high load flexibility. However, the significant temperature rise ($T_{g,max} = 644$ °C) can induce thermal deactivation of the catalyst.

The cooled reactor exhibits the typical hot-spot at a dimensionless length of about 0.2 and approaches the temperature of the coolant asymptotically. The methane fraction strongly increases with temperature, due to the positive effect of increasing temperature on the reaction rate. Downstream from the hot-spot, the rising of the conversion decreases, due

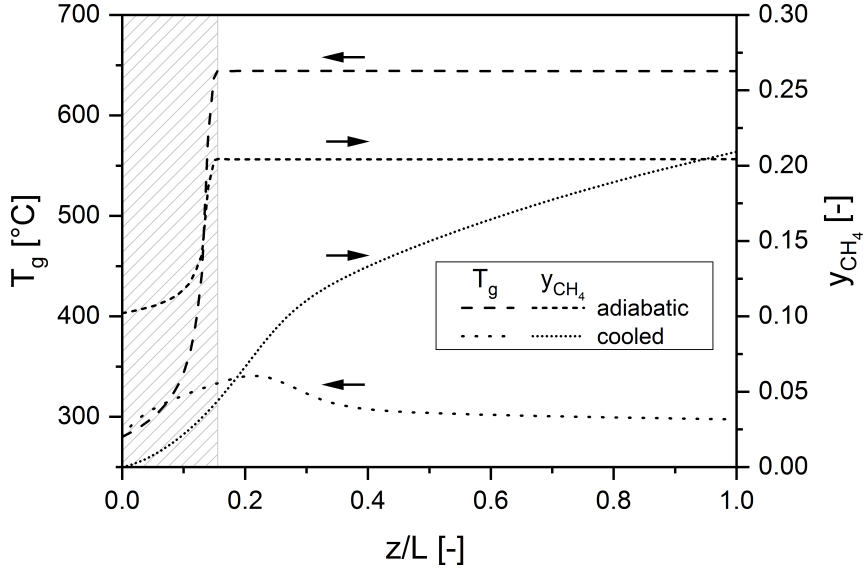


Figure 5.1: Steady-state axial profiles of the gas temperature T_g and the methane content y_{CH_4} for both reactor types (dashed: adiabatic reactor with the grey-marked reaction zone, dotted: cooled reactor).

to the virtually constant temperature. The chemical equilibrium is not reached under the considered conditions, which comprise in particular the reactor length, the catalyst activity and the cooling potential. Nevertheless, in comparison to the adiabatic reactor, the cooled reactor achieves a higher methane content and a lower maximum temperature but also requires a significantly higher residence time. The maximum of the gas temperature is used as a characteristic value for cooled reactors below. A detailed analysis of a cooled fixed-bed reactor for the PtG process was conducted by Molina et al. (2016).

Due to heat transfer from the reaction zone towards the cooling medium and the reactor outlet, the different phases in the reactor exhibit different temperatures. Fig. 5.2 illustrates the temperature differences between catalyst and gas phase ΔT_{c-g} , as well as gas phase and reactor wall ΔT_{g-w} . For the adiabatic reactor, the highest temperature difference between gas phase and catalyst ΔT_{c-g} is observed in a narrow region near the end of the reaction zone, while the difference between the gas phase and the reactor wall ΔT_{g-w} is small. In contrast, the temperature difference between catalyst and gas phase ΔT_{c-g} in the cooled reactor is small, while it is significant between the gas phase and the reactor wall ΔT_{g-w} over the whole reactor length with a pronounced maximum at the hot-spot. Thus, the catalyst temperature can be significantly higher than the gas temperature especially during the unsteady-state operation. If only the gas temperature is measured, it can be concluded that a safety factor is required, regarding the maximum temperature of the catalyst.

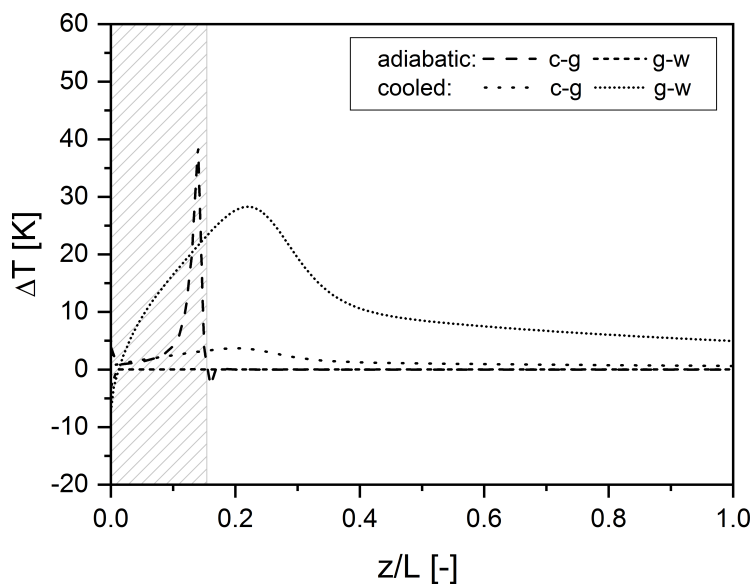


Figure 5.2: Steady-state axial profiles of the temperature differences ΔT between catalyst and gas phase (c-g) as well as gas phase and reactor wall (g-w) for both reactor types (dashed: adiabatic reactor with the grey-marked reaction zone, dotted: cooled reactor).

These steady-state results of the FBRR were further validated with the parameters of Schlereth et al. (2014) (appendix B.3) verifying the parametric sensitivity of the cooled fixed-bed reactor. Moreover, the steady-state temperature profile of the adiabatic reactor indicates that the potential of self-acceleration and thus the formation of dynamic phenomena are present (cf. Figure 2.8 in subsection 2.3.3).

5.1.2 Load range regarding the inlet parameters

For chemical reactors the load is defined by the inlet stream with its physical properties (volumetric flow rate, temperature, pressure, and composition). The influence of these physical properties on the load range is presented for the adiabatic reactor with a constant recycle ratio ($Rec = 1$) and for the cooled reactor without product recycle. The pressure is excluded from these studies, due to its negligible effect on the chemical equilibrium at evaluated pressure. Again the axial profiles at the steady state are analysed.

Adiabatic recycle reactor

For the adiabatic reactor the *volumetric flow rate* at the system inlet was varied corresponding to a *superficial velocity* at the reactor entrance between 0.19 and 1.94 m s⁻¹. With increasing flow rate the reaction zone is moving downstream (Fig. 5.3), which can be

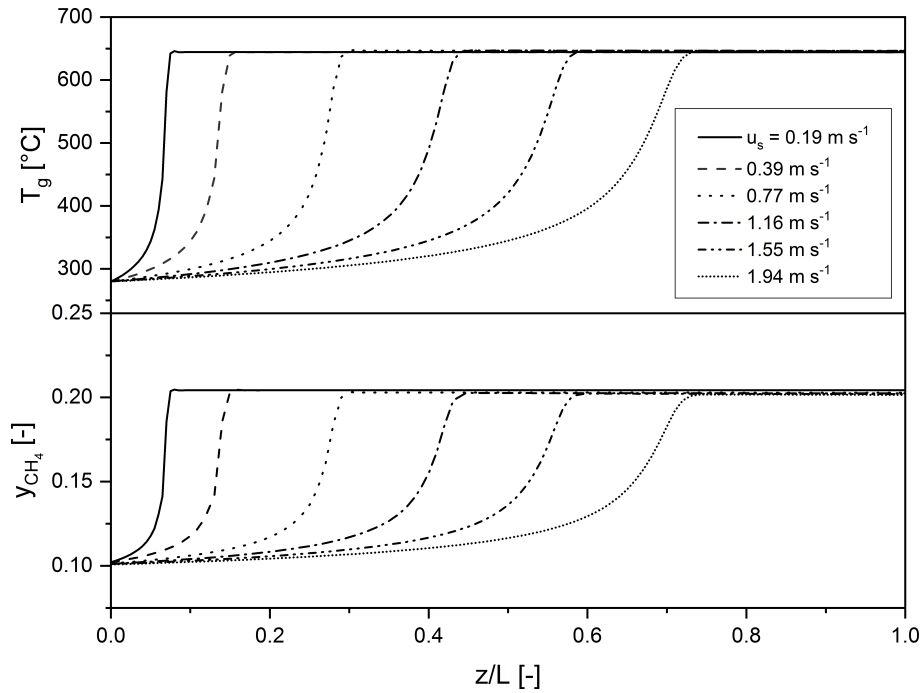


Figure 5.3: Steady-state axial profiles of the gas temperature T_g (top) and the methane content y_{CH_4} (bottom) in the adiabatic reactor ($Rec = 1$) for different superficial velocities u_s .

concluded from a shift of the temperature and methane content profile. The maximum of the methane content (corresponding to an overall CO_2 conversion of 73 %) and the temperature is only slightly affected by the superficial velocity, since the equilibrium is reached inside the reactor. This means that the load range of the adiabatic reactor is broad and could be even further extended, as long as the equilibrium conditions are met at the outlet. However, the maximum flow rate is limited by the related increase in pressure drop. In the presented example, the pressure drop normalized by the system pressure is 6 % for the highest superficial velocity. Conversely, low superficial velocities cause an increase in start-up time (2 567 s for 0.19 m s^{-1} and 347 s for 1.94 m s^{-1}), since the heat flow induced by the chemical reaction is proportional to the volumetric flow rate at constant conversion (cf. Eq. 2.5 in subsection 2.2).

Additionally, the *inlet temperature* was varied between 220 and 300 °C, corresponding to a slight variation of the superficial velocity between 0.35 and 0.42 m s^{-1} (Figure 5.4). A reduction of the inlet temperature from 300 to 220 °C leads to a decrease of the maximal gas temperature by about 47 K, the conversion is reduced to 76.7 %, and the steady state is reached 389 s later. The reaction zone is shifted downstream. Therefore, the inlet temperature has to be selected in coordination with the activity of the catalyst and the

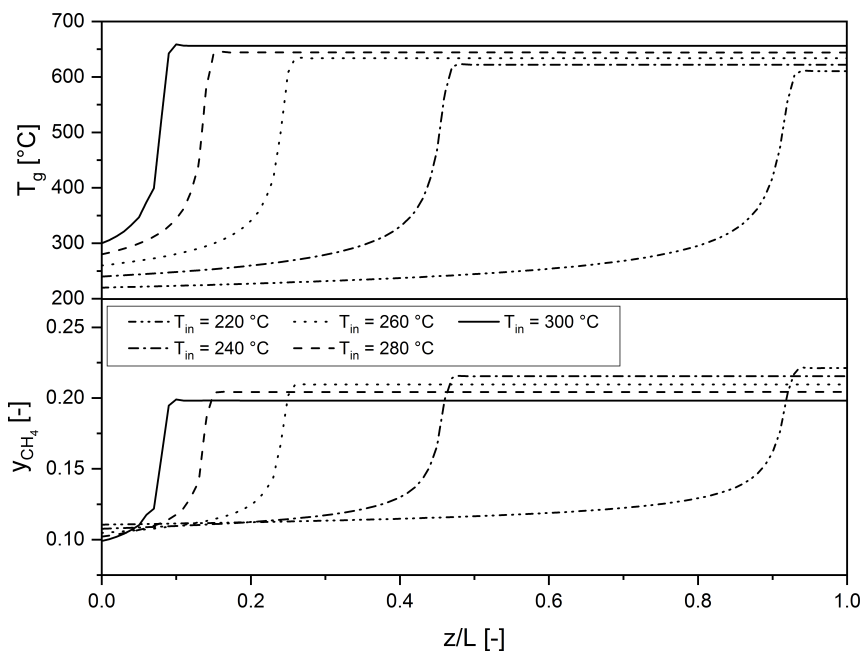


Figure 5.4: Steady-state axial profiles of the gas temperature T_g (top) and the methane content y_{CH_4} (bottom) in the adiabatic reactor ($Rec = 1$) for different inlet temperatures T_{in} .

reactor length. Otherwise, the inlet temperature can be used to control the position of the reaction zone.

Figure 5.5 shows the sensitivity of the maximal gas temperature at steady state $T_{g,ss,max}$ on volumetric flow rate and inlet temperature. If the ‘adiabatic temperature maximum’ is reached, the maximal gas temperature is only moderately influenced by the inlet temperature in the adiabatic reactor (cf. Fig. 5.4 for $10 \text{ m}^3 \text{ h}^{-1}$ (STP)). However, if the reactor is ‘kinetically-limited’, the maximal gas temperature increases by the magnitude of several hundred Kelvin (e. g. by 184 K for T_{in} from 200 to 220 °C for $\dot{V}_{in} = 10 \text{ m}^3 \text{ h}^{-1}$ (STP)). The volumetric flow rate determines the inlet temperature, at which the adiabatic reactor switches from ‘kinetically-limited’ to the ‘adiabatic temperature maximum’. To guarantee a load-flexible operation, the catalyst with its maximal operation temperature should be selected according to the adiabatic temperature maximum. This means that the load flexibility is determined, on the one hand, by the operation restrictions of the catalyst and, on the other hand, by the reactor design as well as by the operation parameters. To limit the maximal gas temperature at steady state $T_{g,ss,max}$, the inlet gas can be diluted.

In comparison to cooled reactors (Sun et al. 2017b), neither hysteresis nor multiple steady-states were detected between the ignition and the extinction (cf. Fig. 5.5 for $40 \text{ m}^3 \text{ h}^{-1}$ (STP)). Therefore, the inlet temperature was increased from 200 °C and

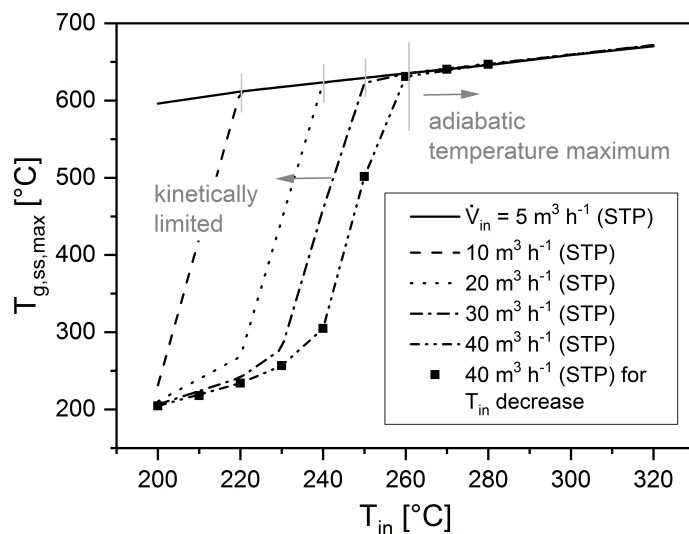


Figure 5.5: Sensitivity of the maximal gas temperature at steady state $T_{g,ss,max}$ on inlet temperature T_{in} and volumetric flow rate \dot{V}_{in} for the adiabatic reactor ($Rec = 1$).

decreased from 280 °C, respectively, to the new set point. The same steady states are reached independently of the initial steady state.

If the *composition of the inlet gas* is not chosen in a stoichiometric ratio, the maximal gas temperature decreases and the conversion of carbon dioxide increases with the rising H_2/CO_2 -ratio. As an example, if the inlet gas is diluted with methane similar to an increase of the methane content by product recirculation (cf. Fig. 5.6), the maximal gas temperature decreases (by about 127.7 K for y_{dil} from 0 to 0.3, cf. Ghaib (2016)) and the overall conversion increases from 73 for $y_{dil} = 0$ to 79% for $y_{dil} = 0.3$. Furthermore, the reaction zone is slightly extended, due to the mitigated temperature rise. The start-up time is slightly accelerated from 24 min at 0 vol% to 21 min at 30 vol% methane in the inlet gas.

Cooled reactor

For the cooled reactor, the *superficial velocity* was varied between 0.6 and 1.5 $m\ s^{-1}$ at a constant temperature for the cooling medium of 290 °C (note that the cooled reactor is operated without product recycle). Fig. 5.7 shows the derived profiles for gas temperature and methane content. With decreasing superficial velocity, an increasing overall carbon dioxide conversion up to 91.7% is observed due to the enlargement of the residence time. However, a distinct hot-spot formation occurs at low velocities, since the convective heat removal and the radial heat transfer coefficient are reduced simultaneously. For a reduction of the superficial velocity from 0.75 to 0.60 $m\ s^{-1}$ the maximal value of the reaction rate

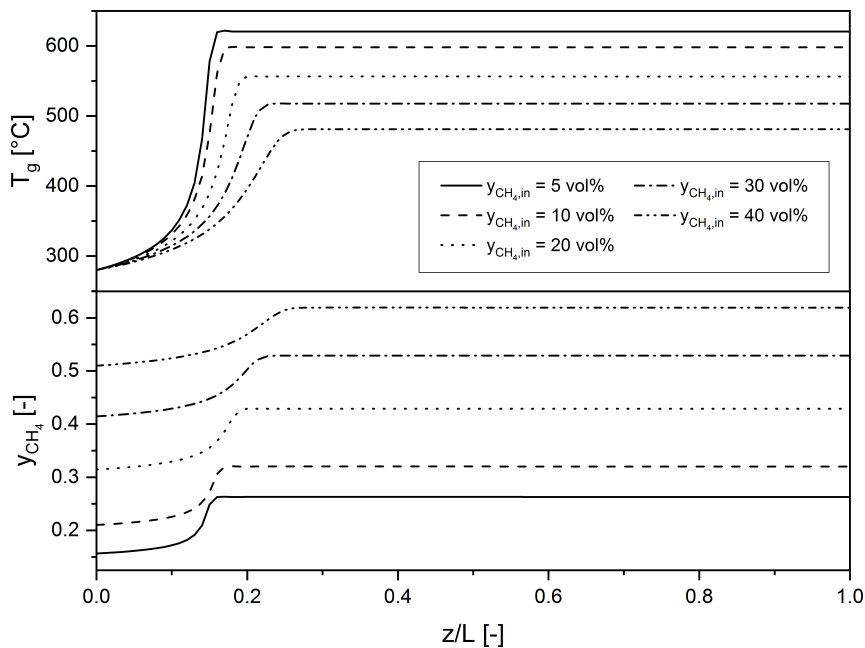


Figure 5.6: Steady-state axial profiles of the gas temperature T_g (top) and the methane content y_{CH_4} (bottom) in the adiabatic reactor ($Rec = 1$) for different inlet concentrations of methane $y_{CH_4,in}$.

increases from 0.57 to $5.16 \text{ mol kg}_{cat}^{-1} \text{ s}^{-1}$, corresponding to a temperature rise up to $598 \text{ }^\circ\text{C}$ for a superficial velocity of 0.60 m s^{-1} .

The sensitivity of the hot-spot formation (run-away) on the temperature of the coolant and the superficial velocity is shown in Fig. 5.8. Obviously, an increase of the superficial velocity reduces the maximum temperature, since the heat removal by axial gas convection increases. With decreasing temperature of the coolant, the maximum temperature also decreases, due to the improved radial heat removal at almost constant heat transfer coefficients. The sensitivity of the maximum temperature on both parameters is pronounced. The lower the superficial velocity at the reactor entrance is, the lower the temperature of the coolant should be.

It thus turned out that the temperature of the coolant and superficial velocity (in relation to the residence time) are the key parameters affecting the load range of the cooled reactor, since they allow an effective removal of the reaction heat. This reduces a pronounced hot-spot formation and thus decelerates the average reaction rate, which in turn leads to lower CO_2 conversion.

Consequently, the load range of the cooled reactor is narrow – compared to that of the adiabatic reactor. Furthermore, the very sensitive behaviour facilitates a high controlling effort as well as an in-depth understanding of the interaction between heat and mass transfer with the reaction kinetics. Additionally, the specific reactor design, including the

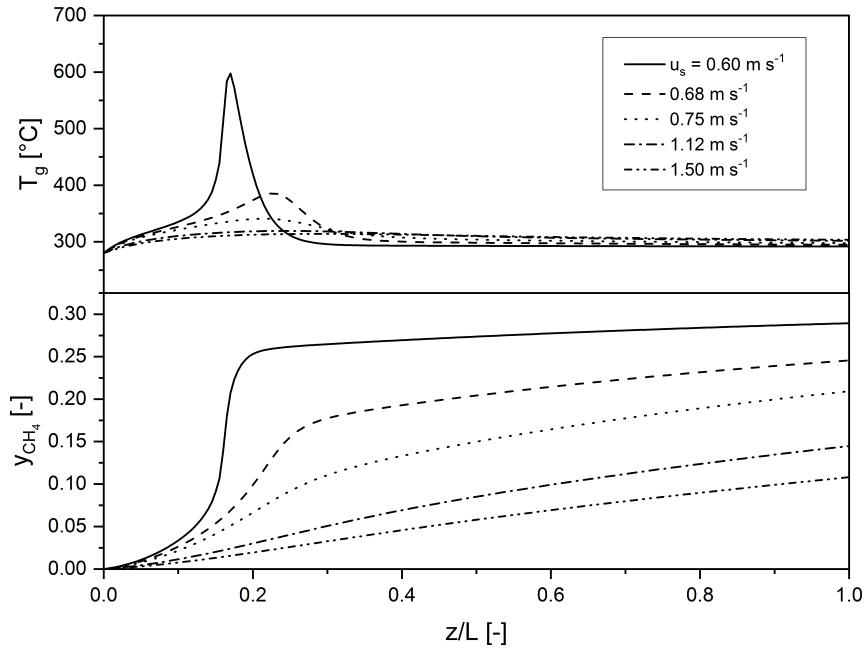


Figure 5.7: Steady-state axial profiles of the gas temperature T_g (top) and the methane content y_{CH_4} (bottom) in the cooled reactor ($T_a = 290 \text{ }^\circ\text{C}$, $Rec = 0$) for different superficial velocities u_s .

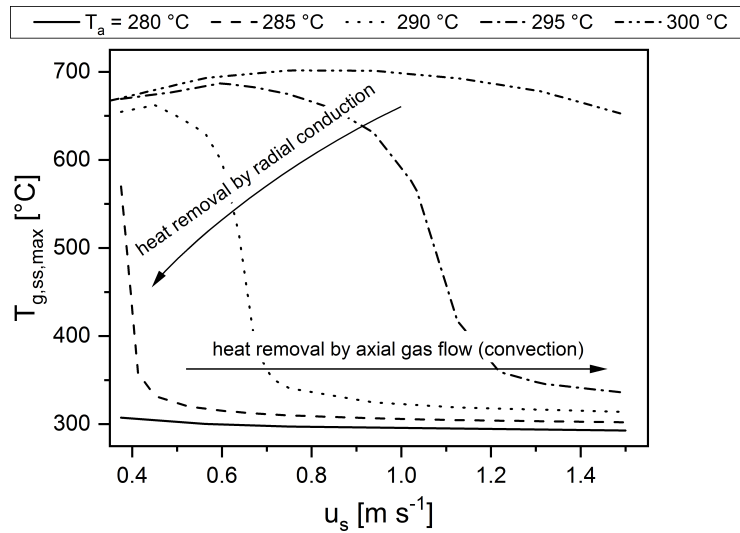


Figure 5.8: Sensitivity of the maximal gas temperature at steady state $T_{g,ss,max}$ on superficial velocity u_s and temperature of the coolant T_a for the cooled reactor ($Rec = 0$).

packed-bed and the cooling concept, has to be considered properly for dynamic operation. However, the maximum temperature in a cooled reactor is about 303 K smaller compared to that of the adiabatic reactor, which reduces catalyst deactivation and the demands for the materials used in reactor construction.

At next, the *inlet temperature* was varied between 220 and 320 °C, corresponding to a slight variation of the superficial velocity between 0.67 and 0.80 m s⁻¹ at the reactor inlet. Figure 5.9 shows that an increase of the inlet temperature leads to an increase of the hot-spot temperature. For example, the hot-spot temperature is only 337.9 °C for $T_{in} = 220$ °C, but raises up to 672.1 °C for the highest inlet temperature ($T_{in} = 320$ °C). The Semenov number (calculated according to Eq. 2.4 with an activation energy of 70.52 kJ mol⁻¹ (Kiewidt et al. 2015)) is only 0.04 for 220 °C, but increases to 1.02 for an inlet temperature of 320 °C, which verifies the hot-spot formation as well. In the example simulations, a significant hot-spot is formed, when the inlet temperature is higher than the temperature of the coolant. Then, the reaction rate and the conversion increased similar to an adiabatic reactor ($r_{max} = 12.13$ mol kg_{cat}⁻¹ s⁻¹ and $X_{CO_2} = 90.8$ % for $T_{in} = 320$ °C). The outlet temperature is almost independent of the inlet temperature, due to the radial heat transfer to the cooling medium. Figure 5.10 shows the sensitivity towards the inlet flow rate and the volumetric flow rate at the same time. In a safe operation range, the maximal gas temperature is determined by the volumetric flow rate and its influence on the efficient radial heat transfer. Hence, the inlet temperature cannot be used for process control or to extend the load range. But cooled reactors are load-flexible due to the inlet temperature in the ‘safe operation range’ meaning that the inlet temperature is lower than the temperature of the coolant. In this range, the maximal gas temperature does not exceed the typical operation limits of methanation catalysts for sufficient high volumetric flow rates.

5.2 Load changes without product recirculation

Load changes occur during the start-up, the shutdown, and the operation. The start-up behaviour is presented in subsection 5.2.1. Load changes of the volumetric flow rate are analysed in detail in subsection 5.2.2 for the adiabatic reactor only, because the dynamics of the cooled reactor are presented in the literature by Try et al. (2018) and Sun et al. (2017b).

The steady-state time t_{ss} is reached if the difference of the gas temperature at the reactor outlet is smaller than 0.001 K between two successive time steps (a time step of 1 s was chosen for the simulations, cf. section 3.2). To analyse the dynamics of the load ramps, the global maximum is characterized by its value and the time of appearance after the start of the ramp. The value of the maximum is determined in relation to the steady-state value at the reactor outlet prior to the ramp for the gas temperature ΔT_g (Eq. 5.1) and the methane content Δy_{CH_4} (Eq. 5.2).

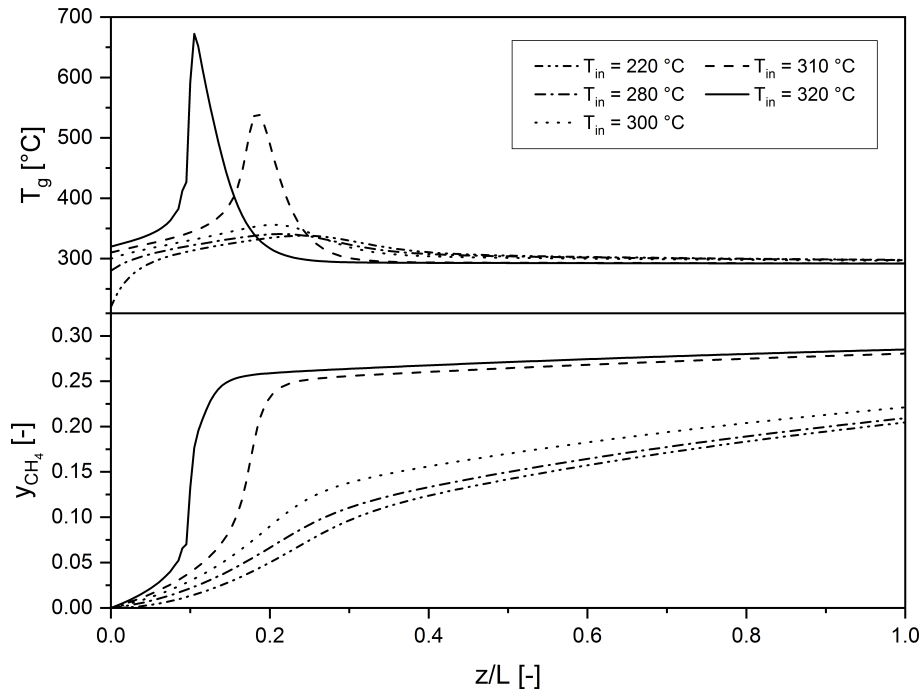


Figure 5.9: Steady-state axial profiles of the gas temperature T_g (top) and the methane content y_{CH_4} (bottom) in the cooled reactor ($T_a = 290$ °C, $Rec = 0$) for different inlet temperatures T_{in} .

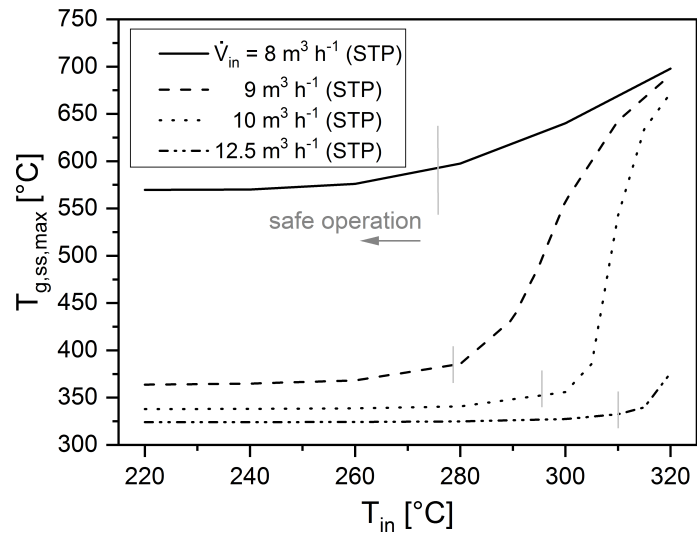


Figure 5.10: Sensitivity of the maximal gas temperature at steady state $T_{g,ss,max}$ on inlet temperature T_{in} and volumetric flow rate \dot{V}_{in} for the cooled reactor ($Rec = 0$).

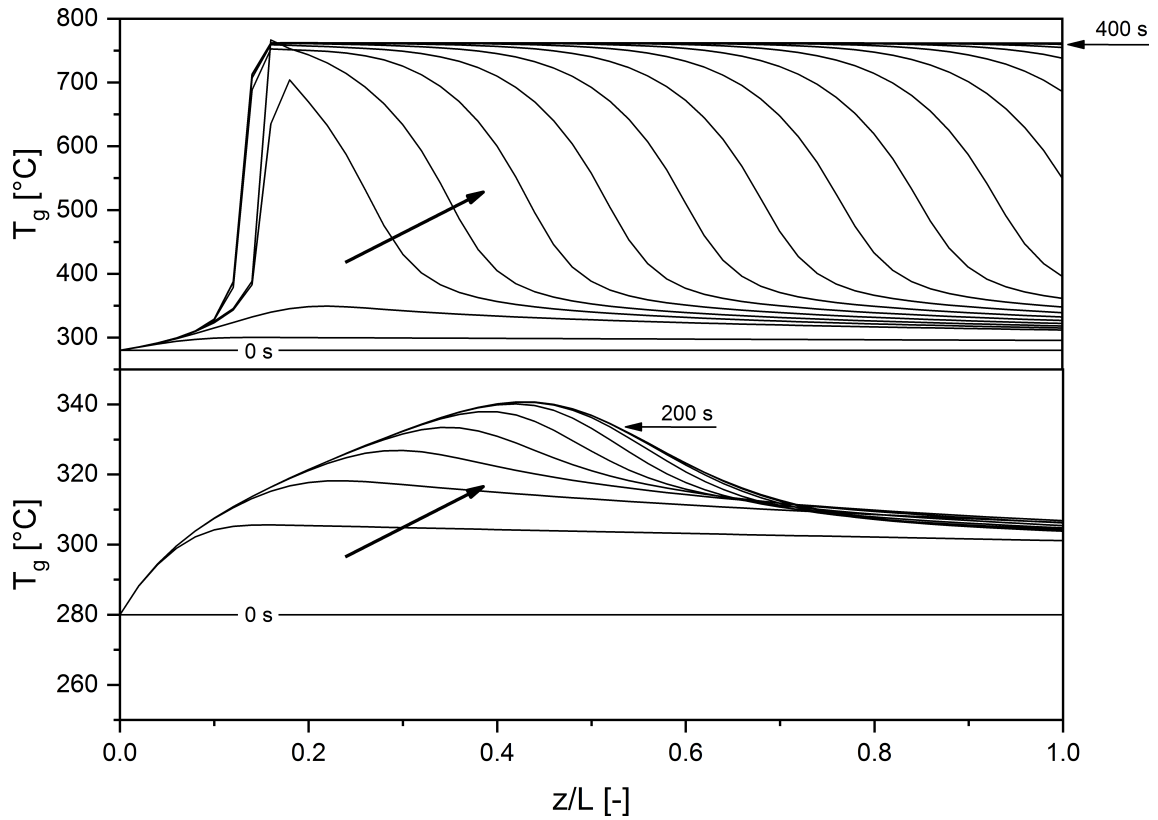


Figure 5.11: Time-dependent temperature profiles of the gas phase T_g for the adiabatic reactor (top) and the cooled reactor (bottom), line interval for both reactors 20 s (conditions deviating from Table 3.2: $L = 1$ m, $d_r = 2.54$ cm, $Rec = 0$.)

$$\Delta T_g = T_{g,max} - T_g(t = 0 \text{ s}, z = L) \quad (5.1)$$

$$\Delta y_{CH_4} = y_{CH_4,max} - y_{CH_4}(t = 0 \text{ s}, z = L) \quad (5.2)$$

5.2.1 Start-up behaviour

Primarily, the start-up behaviour is studied to determine time required for a warm start to reach steady state. An equal reactor size was chosen for the comparison of the start-up behaviours between the adiabatic and the cooled reactor ($L = 1$ m, $d_r = 2.54$ cm, $Rec = 0$, leading to $\bar{t} = 1.33$ s). For the warm start, the initial temperature for the catalyst, gas phase and the reactor wall was set to 280 °C throughout the reactor. This corresponds to the ignition temperature for methanation on the basis of own experimental results and literature results e. g. by Try et al. (2018).

The temporal development of the gas temperature profile along the reactor is shown for the adiabatic reactor and the cooled reactor without product recirculation in Fig. 5.11. The cooled reactor reaches the steady state after 197 s, while the adiabatic reactor requires 392 s. The steady state temperature level of the adiabatic reactor is higher, meaning that more energy has to be provided by the reaction enthalpy to heat-up the reactor and to reach steady state, which takes longer time. It was also observed that the heat-storage capacity of the reactor wall is a significant factor affecting the transient behaviour. For illustration, the characteristic time for the temperature increase t_{th} puts the heat-storage capacity of the reactor (numerator) in relation to the heat capacity stream at the reactor inlet (denominator) (Eq. 5.3). The mass of the gas inside the reactor was considered to be negligible, compared to the masses of the catalyst and the reactor wall. The resulting characteristic time is 434 s with the thermal inertia of the reactor wall (numerator: $m_c c_{p,c} + m_w c_{p,w}$) and 129 s without (numerator: $m_c c_{p,c}$), respectively. Thus, the characteristic time for the temperature increase considers the reactor wall and provides a good estimation for time to reach the steady state in the adiabatic reactor. The observations underline the importance of considering all heat-storage capacities in the system appropriately for dynamic simulations.

$$t_{th} = \frac{m_r c_{p,r}}{\dot{m}_{g,in} c_{p,g,in}} = \frac{m_c c_{p,c} + m_w c_{p,w}}{\dot{m}_{g,in} c_{p,g,in}} \quad (5.3)$$

Figure 5.12 shows steady-state time t_{ss} depending on the wall thickness for the full-scale adiabatic reactor (conditions according to Table 3.2: $L = 1$ m, $d_r = 5$ cm, $Rec = 1$). This figure highlights the almost linear relationship between the thickness of the reactor wall and the start-up time, which is included in the calculation of the characteristic time for the temperature increase as well. The offset of 710 s for a very small reactor wall thickness of 0.01 mm, indicates the start-up time required for heating up the catalyst mass, which was held constant.

5.2.2 Dynamic behaviour of the adiabatic reactor

For the case without gas recycle the volumetric flow rate of the diluted inlet gas with $y_{N_2} = 0.75$ was halved to $5 \text{ m}^3 \text{ h}^{-1}$ (STP) ($u_s = 0.19 \rightarrow 0.10 \text{ m s}^{-1}$ at the reactor inlet) and doubled to $20 \text{ m}^3 \text{ h}^{-1}$ (STP) ($u_s = 0.19 \rightarrow 0.39 \text{ m s}^{-1}$) during the load changes taking place within 1 s (step) and up to 600 s (ramps). The reactor was shortened to 0.5 m, since a finer axial step-size was required and the chemical equilibrium had already been reached in the first fifth of the reactor (cf. Fig. 5.1).

Flow rate steps

Fig. 5.13 shows the axial profiles of the gas temperature (top) and the methane content (bottom) for the load change corresponding to a step ($t_{ramp} = 1$ s). The steady-state

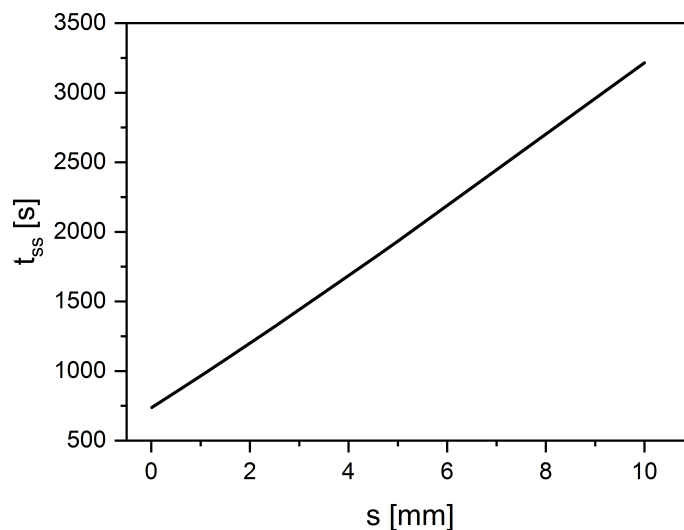


Figure 5.12: Steady-state time t_{ss} depending on the wall thickness s for the adiabatic reactor (conditions according to Table 3.2: $L = 1$ m, $d_r = 5$ cm, $Rec = 1$).

profile before the ramp starts is marked with a bold black line and the new steady state afterwards with a bold grey line. The axial profiles in-between transitions are coloured.

If the volumetric flow rate drops to $5 \text{ m}^3 \text{ h}^{-1}$ (STP), the temperature front shifts upstream, since the gas is heated-up earlier in the reactor, affirmed by comparing both steady-state profiles. This induces a minimum in the temperature profile during the transient transition phase. Since the reactor is operated adiabatically, heat is neither removed nor supplied to the catalyst bed via the reactor wall and can thus only be transported by axial convection. Consequently, the cold portion of the catalyst bed between both steady states has to be heated during the transient phase, which induces a local temperature minimum moving wave-like downstream until the new steady state is reached. In contrast to polytropically operated reactors (Try et al. 2018), the minimum reaches the reactor outlet. The shape of the temperature profile also broadens whilst moving towards the reactor outlet, even though axial dispersion was not considered directly in the heat and material balance. This is caused by the temporary storage of heat in the reactor wall. Due to the coupling between the temperature and composition via the chemical equilibrium, a global maximum is formed for the methane content. An increase in volumetric flow rate to $20 \text{ m}^3 \text{ h}^{-1}$ (STP) exhibits the opposite behaviour. The higher amount of unreacted gas encountering the hot part of the reactor forms a steep gradient in the reaction zone. The resulting temperature maximum (56 K difference to steady state) also moves wave-like downstream to the reactor outlet, where the hot-spot reduces to 26 K.

In accordance with the literature, changes of the flow rate lead to moving hot-spots (Yakhnin et al. 2004). The global maximum of the methane content for a flow rate reduction and the global maximum of the gas temperature for the flow rate increase are picked out

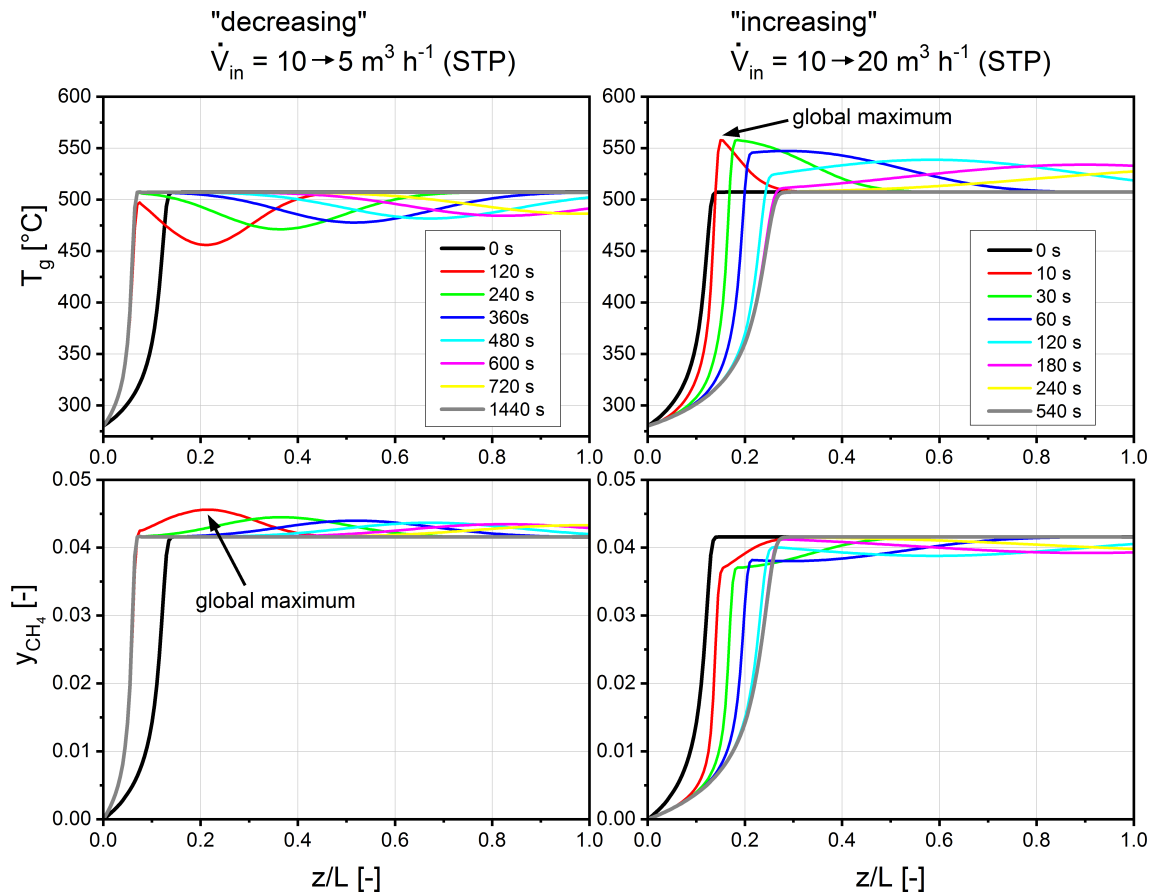


Figure 5.13: Axial profiles of the gas temperature T_g (top) and the methane content y_{CH_4} (bottom) in the adiabatic reactor ($Rec = 0$) since the step started (0 s), for positive (right) and negative (left) flow rate step ($t_{ramp} = 1$ s).

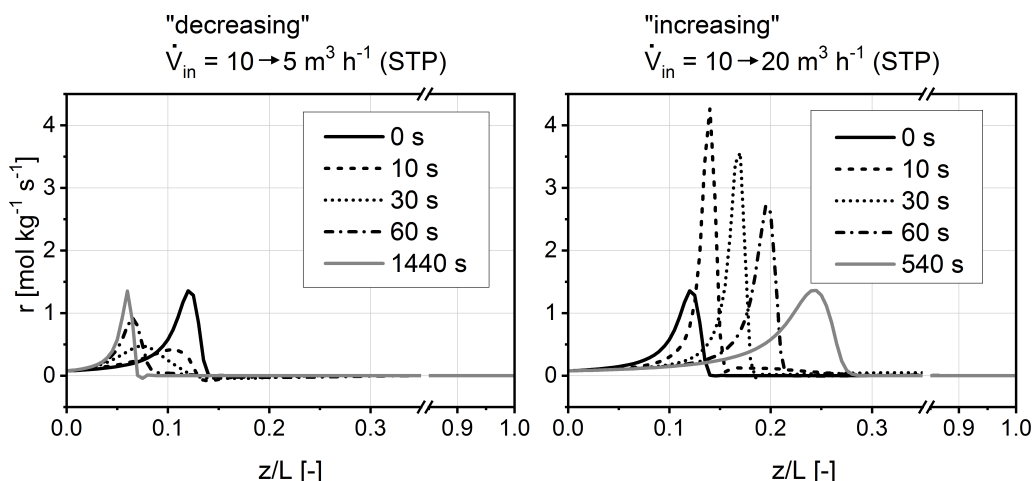


Figure 5.14: Axial profiles of the reaction rate r in the adiabatic reactor ($Rec = 0$) since the step started (0 s), for positive (right) and negative (left) flow rate step ($t_{ramp} = 1$ s).

for further analyses. From a practical point of view, the temporary hot-spot formation is disadvantageous, since it can lead to thermal instabilities, a run-away, and catalyst deactivation.

For a deeper understanding of the moving hot-spots during the load ramp, Fig. 5.14 shows the axial profiles of the reaction rate. During the initial steady state (at 0 s) the reaction rate increases, reaches a maximum, and drops sharply. The temperature increase is responsible for the increasing branch, and the consumption of the reactants causes the decrease afterwards. Obviously, a reaction zone exists, which is followed by a region with a constant reaction rate close to zero, indicating that equilibrium conditions have been reached.

If the volumetric flow rate is decreased to $5 \text{ m}^3 \text{ h}^{-1}$ (STP), the peak value of the reaction rate is first reduced from 1.36 to $0.40 \text{ mol kg}_{cat}^{-1} \text{ s}^{-1}$ and broadens, followed by an increase of the reaction rate maximum and its shift towards the reactor inlet. This is in agreement with the local minimum of the gas temperature in Fig. 5.13 during the transient period, since heat production is proportional to the reaction rate for an adiabatic reactor. The phase of the decelerated reaction rate can be explained by its non-linear dependence on the reduced temperature according to Arrhenius law. The broadening of the reaction rate profile is caused by the almost constant methane content at the reactor outlet during the transient phase. Thus, the integrated area below the reaction rate curve has to be constant at each time step, which requires broadening to compensate a reduced maximum-value. Negative rate values correspond to the reverse reaction of the CO_2 methanation (steam reforming), which can be explained by numerical issues regarding the simulation. However, the influence is negligible in comparison to the peak of the reaction rate ($r_{min} = -0.03 \text{ mol kg}_{cat}^{-1} \text{ s}^{-1}$).

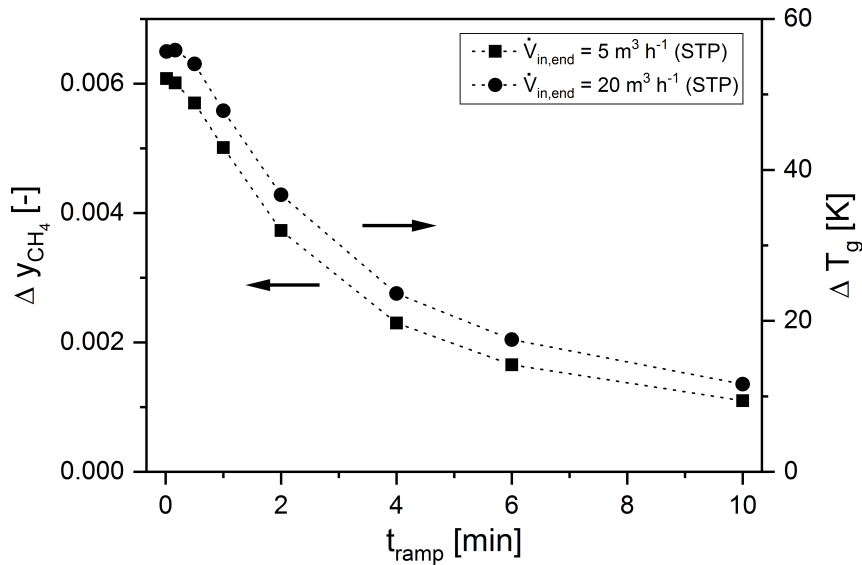


Figure 5.15: Global maxima in dependence of the ramp time t_{ramp} for the reduction (Δy_{CH_4} , left y-axis) and for the increase of the volumetric flow rate (ΔT_g , right y-axis) in the adiabatic reactor ($Rec = 0$).

If the volumetric flow rate is increased to $20 \text{ m}^3 \text{ h}^{-1}$ (STP), the peak value of the reaction rate increases up to $4.42 \text{ mol kg}_{cat}^{-1} \text{ s}^{-1}$, which corresponds to the gas temperature transition discussed in Fig. 5.13. The reaction is accelerated temporarily and the axial position of the reaction rate peak moves downstream whilst decreasing. Furthermore, the profile sharpens during the transient phase, because the reaction front moves faster (left side of the peak) compared with the thermal front (right side) (Eigenberger et al. 2007). Thus, the increase and decrease in volumetric flow rate exhibit opposing effects on the axial reaction rate profiles.

Effect of the ramp time

The ramp time has no influence on the axial profile of the new steady state, which will be reached after the ramp. However, the height of the global maximum (Fig. 5.15) and the dynamics of the transition (Fig. 5.16) are influenced. Fig. 5.15 shows that an increase of the ramp time (corresponding to a reduction of the load change gradient) leads to a significant reduction of the global maximum – irrespective of whether or not the volumetric flow rate is increased or decreased during the load ramp – which can be explained as follows. A ramp with a minor gradient can be regarded as a sequence of several successive steps with smaller step-size. Thus, each individual step induces a less pronounced transient behaviour as discussed above, which is superimposed with prior and the following step responses. As a consequence, the reduced maximum is caused by constructive and destructive interference

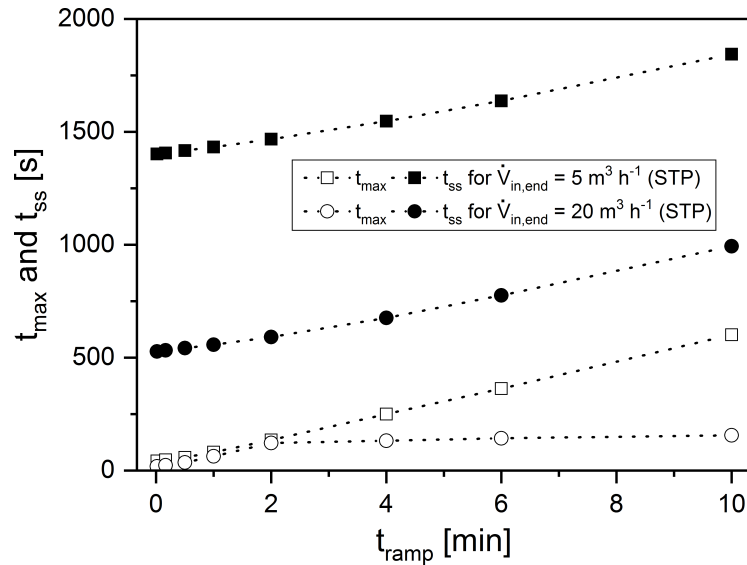


Figure 5.16: Steady-state times t_{ss} as well as the time steps for the global maxima t_{max} in dependence of ramp time t_{ramp} in the adiabatic reactor ($Rec = 0$).

of the travelling waves. Hence, from an industrial point-of-view, the maximum temperature tolerated by the catalyst limits the maximum gradient of the volumetric flow rate ramp.

If the ramp time is increased, the time-period until reaching the global maximum and the steady state raises nearly linear (Fig. 5.16). However, if the volumetric flow rate is doubled during the load ramp, the time-period for reaching the global maximum increases slightly and approaches a small value asymptotically. This can be explained by moving hot-spots discussed above, which induces the immediate ignition of the reaction, followed by the dispersion of the released heat by temporary storage in the thermal inertia. Consequently, the reaction rate profiles exhibit the global maximum immediately following the step change (after 10 s in Fig. 5.14). With a decreasing ramp gradient, the apparent moving hot-spot is induced by the interference of the successive travelling waves, leading to a less pronounced global maximum appearing later after starting the ramp.

5.3 Product recirculation to control dynamic operation

In this section, the effects of product recirculation on load range are analysed in the first subsection 5.3.1 by means of the steady-state axial profiles for the adiabatic and cooled fixed-bed reactor. In the subsequent subsections, it is investigated for the adiabatic reactor only, how the product recirculation influences the dynamics of the fixed-bed reactor during load ramps (subsection 5.3.2) and how the dynamics can be influenced by an adaptation of the recycle ratio (subsection 5.3.3).

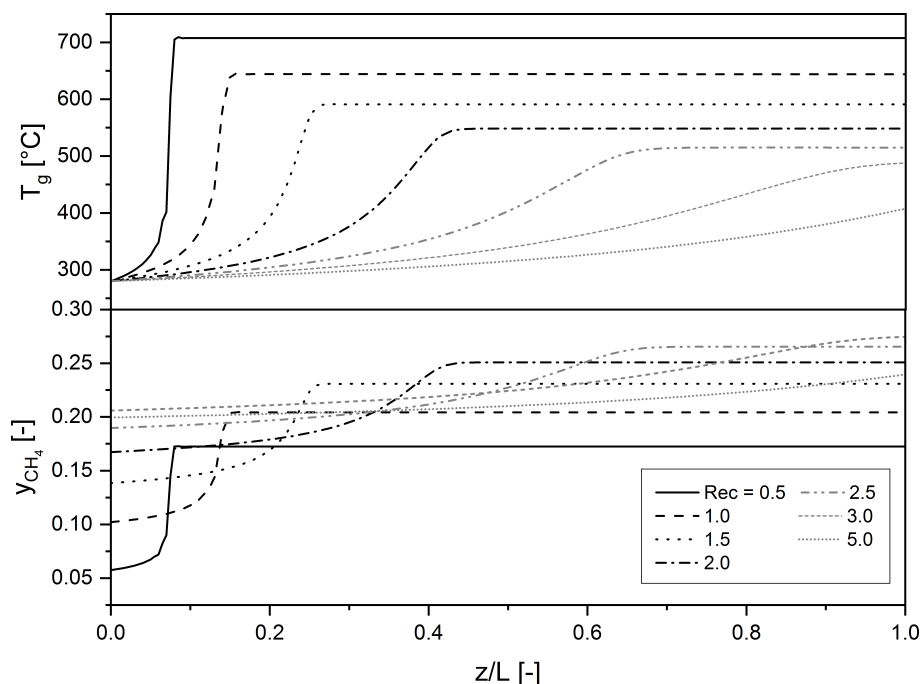


Figure 5.17: Steady-state axial profiles of the gas temperature T_g (top) and the methane content y_{CH_4} (bottom) in the adiabatic reactor for different recycle ratios Rec (superficial velocity increases from 0.19 to 2.13 m s^{-1} with increasing recycle ratio).

5.3.1 Effect of product recirculation on load range

Fig. 5.17 shows the variation of the recycle ratio for the adiabatic reactor with a constant flow rate at the system inlet, which relates to a variation of the superficial velocity in the reactor. With increasing recycle ratio, the reaction zone (defined as the part of the reactor, where equilibrium is not yet achieved) is extended and the adiabatic temperature increase is reduced simultaneously. This is caused by the smaller fraction of educt gases and a higher content of reaction products at the reactor inlet. Note that a separation of reaction products is not included prior to the recirculation. The maximal value of the reaction rate is reduced from $10.6 \text{ mol kg}_{cat}^{-1} \text{ s}^{-1}$ for a recycle ratio of 0.5, to $0.27 \text{ mol kg}_{cat}^{-1} \text{ s}^{-1}$ for a recycle ratio of 5. The overall carbon dioxide conversion (cf. Eq. 4.7) increases with the recycle ratio and reaches a maximum of 88.7% for $Rec = 3$, followed by a decrease to 81.0% for $Rec = 5$. The increase in conversion can be explained by the reduced temperature, which shifts the equilibrium towards the side of the products. For high recycle ratios the chemical equilibrium is not reached in the adiabatic reactor and the conversion is limited by the reaction rate. In other words, the reaction zone exceeds the reactor volume. The relative pressure drop increases with the recycle ratio but is still negligible (less than 1.2% for $Rec = 3$). Interestingly, the increasing recycle ratio accelerates the reactor to reach

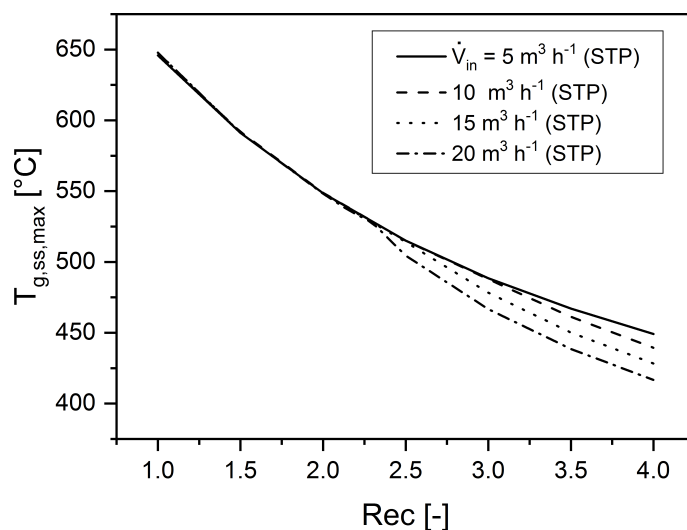


Figure 5.18: Sensitivity of the maximal gas temperature at steady state $T_{g,ss,max}$ for different recycle ratios Rec and volumetric flow rates \dot{V}_{in} in the adiabatic reactor.

the steady state (833 s for $Rec = 3$ and 1441 s for $Rec = 1$), because the steady state temperature level is lowered and thus less reaction heat is required.

The effect of the recycle ratio and the volumetric flow rate at the system inlet on the gas temperature is shown in Fig. 5.18. This figure highlights the cooling effect of the recycle ratio, which is almost independent of the volumetric flow rate at the system inlet. Moreover, the effect on the methane content in the product gas is shown in Fig. 5.19. Obviously, an optimum exists, which is achieved when the reaction zone is identical to the reactor volume. In other words, the chemical equilibrium is reached exactly at the reactor outlet. For lower recycle ratios, the temperature rise in the reactor is higher, and consequently, the equilibrium methane content is smaller. For higher recycle ratios the chemical equilibrium is not achieved and the gas composition is thus kinetically-limited for the chosen simulation parameters, in particular the activity factor and the reactor length.

The optimal recycle ratio with respect to methane content decreases with increasing volumetric flow rate at the system inlet. On the one hand, a high flow rate broadens and shifts the reaction zone towards the reactor outlet (cf. Figure 5.3), since the residence time decreases. On the other hand, the recycle stream cools the adiabatic fixed-bed reactor effectively, which elevates the equilibrium methane content and reduces the residence time even further (cf. Figure 5.17). Therefore, high volumetric flow rates at the system inlet can be compensated by a lower recycle ratio, in order to fully exploit the reactor volume.

For the cooled reactor the recycle ratio was varied between 0 and 5, which corresponds to an increase of the superficial velocity in the reactor from 0.75 to 4.50 m s^{-1} (Fig. 5.20). Simultaneously, the volumetric flow rate at the system inlet was set constant. The product gas recycle reduces the maximal value of the reaction rate from 0.57 without any product

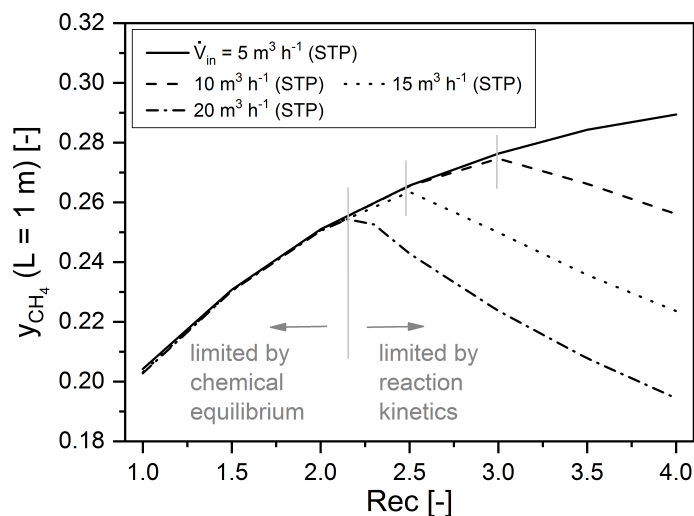


Figure 5.19: Methane content in the product gas y_{CH_4} at the reactor outlet for different recycle ratios Rec and volumetric flow rates at the system inlet \dot{V}_{in} for the adiabatic reactor.

recirculation to $0.09 \text{ mol kg}_{cat}^{-1} \text{ s}^{-1}$ for a recycle ratio of 5, since the inlet gas is diluted with product compounds. Therewith, the overall conversion of carbon dioxide is lowered from 73.7% ($Rec = 0$) to 45.8% ($Rec = 5$) and the hot-spot formation is less pronounced. The residence time is lowered with increasing recycle ratio, explaining the higher methane content of the kinetically-limited reactor without the recirculation of product gas. Thus for small recycle ratios the average temperature in the reactor is higher, while the outlet temperature is comparable.

The negative effect of recirculation on the performance of the cooled reactor in terms of the methane fraction is accompanied by an increase in the prevention of the hot-spot formation, especially for low volumetric inlet flow rates, as discussed in Fig. 5.7. Accordingly, in Figure 5.21 the maximum catalyst temperature is displayed for different recycle ratios and volumetric flow rates at the system inlet. Interestingly, while the sensitivity of the maximum catalyst temperature on the volumetric inlet flow rate is pronounced for recycle ratios smaller than 0.1, a negligible effect is observed for higher values. As an example, a decrease in inlet flow rate from 9.5 to $8.5 \text{ m}^3 \text{ h}^{-1}$ (STP) leads to a temperature increase at the catalyst of 180 K, accompanied by virtually no product recirculation ($Rec = 0.0001$), while it is negligible for a recycle ratio as low as 0.1. From a practical point-of-view, moderate catalyst temperatures can be reached with recycle ratios between 0.05 and 0.1, which help to avoid the thermal catalyst deactivation. For understanding the pronounced sensitivity towards the recycle ratio, the recycle was replaced by an additional feed stream with the same molar flow rate. The effect is shown in Fig. 5.21 for dilution with 10% of N_2 , CH_4 , or H_2O , which is comparable to a recycle ratio of 0.1 (for the example of $\dot{V}_{in} = 7.5 \text{ m}^3 \text{ h}^{-1}$ (STP)). Obviously, the maximum temperature can significantly be reduced

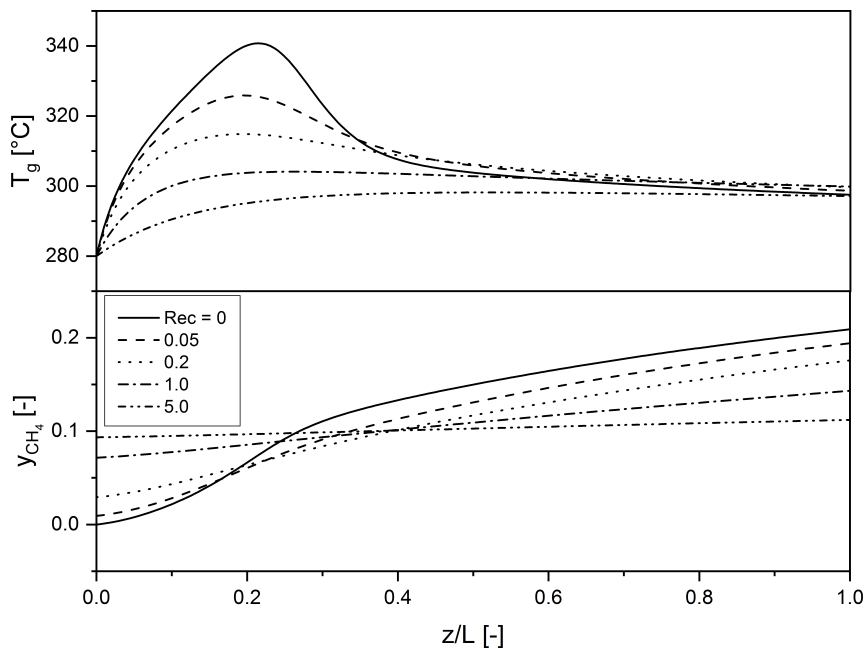


Figure 5.20: Steady-state axial profiles of the gas temperature T_g (top) and the methane content y_{CH_4} (bottom) in the cooled reactor for different recycle ratios Rec (superficial velocity increases from 0.75 to 4.50 m s^{-1} with increasing recycle ratio).

by the dilution, depending on the heat capacity of the dilution stream. Note, that for a high conversion the recycle gas consists of nearly 67% water and 33% methane if no water is separated. This explains the high cooling efficiency of the product recirculation. Consequently, the sensitivity of cooled fixed-bed reactors towards the volumetric inlet flow rate, induced by the fluctuating nature of renewable hydrogen, can be reduced significantly by the product recirculation. A suitable choice of the recycle ratio thus offers to expand the load range as well as the load flexibility. However, the economic impact of additional equipment for the product recycle has to be considered.

5.3.2 Control of dynamic operation

Focusing on the adiabatic reactor only, the volumetric flow rate of the inlet gas was halved to 5 $\text{m}^3 \text{h}^{-1}$ (STP) (corresponding to $u_s = 0.39 \rightarrow 0.19 \text{ m s}^{-1}$ at the reactor inlet) and doubled to 20 $\text{m}^3 \text{h}^{-1}$ (STP) ($u_s = 0.39 \rightarrow 0.77 \text{ m s}^{-1}$) during the operation of the load ramps, taking place within 1 and 600 s. Note, that the recycle ratio was held constant ($Rec = 1$) and no dilution of the inlet gas is required anymore. As an extreme case, the axial trends for the fastest ramp time ($t_{ramp} = 1 \text{ s}$) are shown in Fig. 5.22 ($L = 0.5 \text{ m}$).

In general, the transition between the two steady states is comparable to load ramps without product recirculation. However, with the product gas recycle an additional

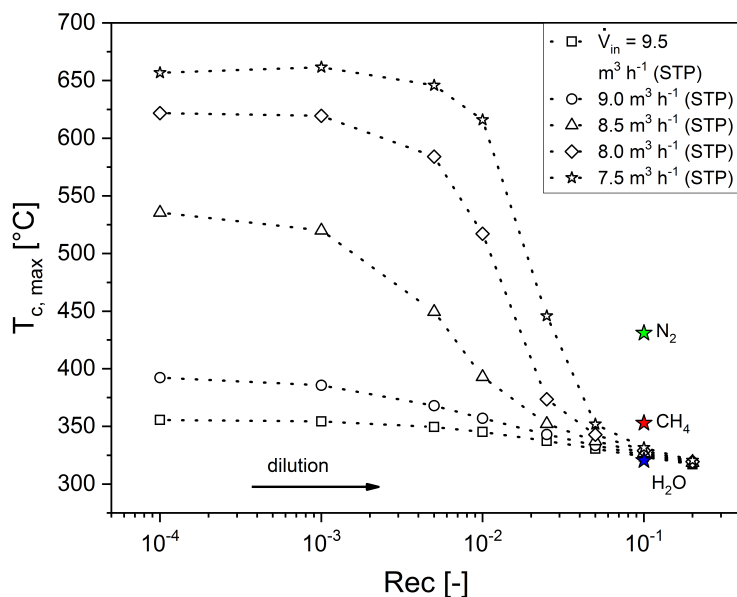


Figure 5.21: Maximum catalyst temperature $T_{c,max}$ for different recycle ratios Rec and volumetric flow rates at the system inlet \dot{V}_{in} of the cooled reactor ($T_a = 290$ °C) and effect of pure dilution streams on the maximum catalyst temperature for $\dot{V}_{in} = 7.5$ m³ h⁻¹ (STP) marked with coloured stars.

dynamic feedback for the methane content at the reactor inlet arises, due to the temporary change at the reactor outlet upon flow rate change. Note that the reactor outlet is directly connected to the inlet with respect to gas composition in the recycle. No sustained moving hot-spots exist (compared to Yakhnin et al. (2004)), because the global maximum decreases with time and a new steady state is reached. The amplitude of the methane content at the reactor inlet is lower compared to the outlet, due to the mixing of the recycle with fresh feed gas. No temperature feedback is observed, since the temperature at the reactor inlet is set constant. Thus, the constant inlet temperature stabilizes the reactor, if sufficient heat exchanger capacity is installed in the product recirculation. The methane content at the reactor inlet in both steady states is equal, since equilibrium is reached in the adiabatically-operated reactor, which defines the outlet temperature and composition from the overall input values.

Again, the global maxima are analysed, as shown in Fig. 5.23. The dynamic response is now influenced by the additional dynamic feedback. If the ramp time is increased up to 10 min, the intensity of the dynamic phenomena can be reduced significantly, which agrees well with the findings in Fig. 5.15. The more pronounced global maximum in methane content is caused by a temperature decrease of 103 K (Fig. 5.22, top-left), since the overall feed gas is not diluted with nitrogen, as in the case without a recycle. Interestingly, this transient minimum of the gas temperature is comparable to the diluted case (84.1 K), which underlines the benefits of a product gas recycle to avoid costly nitrogen separation.

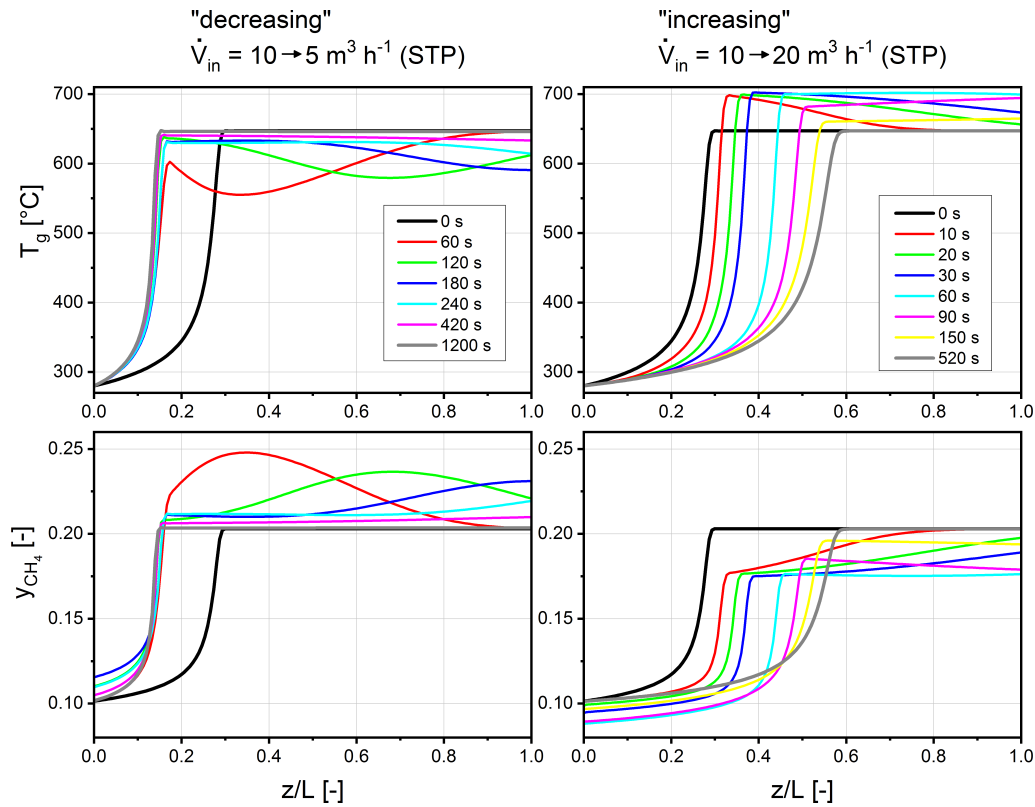


Figure 5.22: Axial profiles of the gas temperature T_g (top) and the methane content y_{CH_4} (bottom) in the adiabatic reactor ($Rec = 1$) since the step started (0 s), for positive (right) and negative (left) flow rate step ($t_{ramp} = 1$ s).

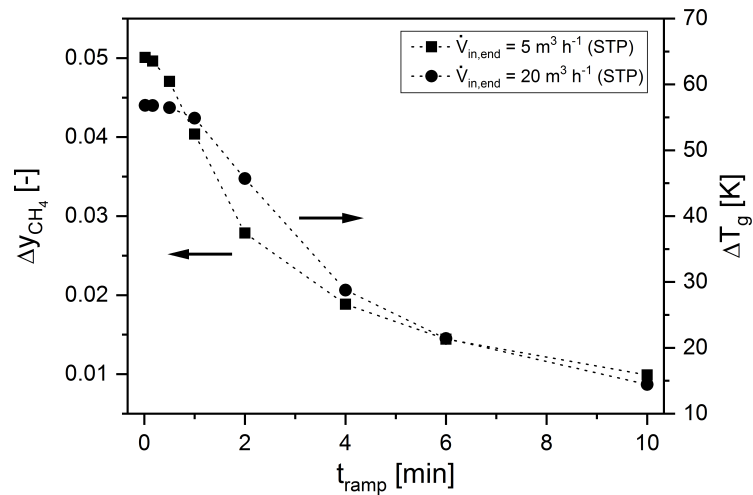


Figure 5.23: Global maxima in dependence of ramp time t_{ramp} for the reduction (Δy_{CH_4} , left y-axis) and for the increase of the volumetric flow rate (ΔT_g , right y-axis) in the adiabatic reactor ($Rec = 1$).

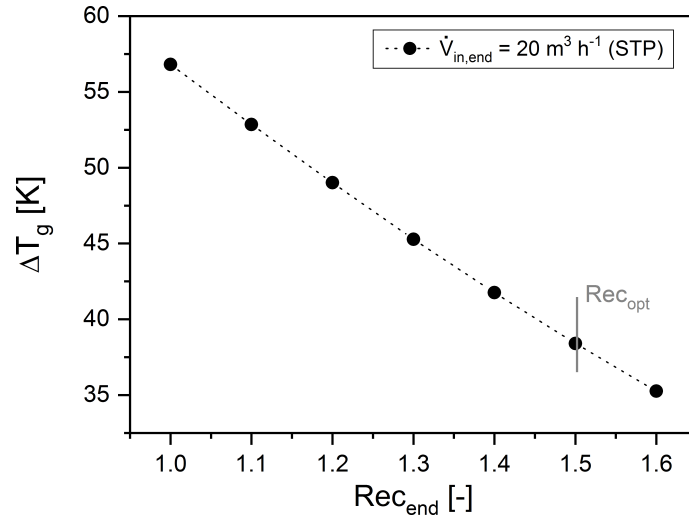


Figure 5.24: Global temperature maximum ΔT_g in the adiabatic reactor for different adaptations of the recycle ratios Rec_{end} (volumetric flow rate increase \dot{V}_{in} from 10 to $20 \text{ m}^3 \text{ h}^{-1}$ (STP), $t_{ramp} = 1 \text{ s}$, $Rec_{start} = 1$, $L = 0.5 \text{ m}$).

5.3.3 Adaptation of the recycle ratio

At next, the recycle ratio is adapted during the load ramp to determine the potential of the recycle as a physical feedback loop for reactor control. As an example, the global temperature maximum during the load increase up to $20 \text{ m}^3 \text{ h}^{-1}$ (STP) is investigated for the load step ($t_{ramp} = 1 \text{ s}$), because the highest value of the global maximum occurs in that case. Even though the adaptation of the recycle ratio during a load step is hardly feasible in real applications in comparison to load ramps, but it provides valuable insights towards the influenceability of the global maximum.

The value of the global maximum can be reduced by about 20 K, if the recycle ratio is raised by a factor of 1.5 from 1 to 1.5 during the step (Fig. 5.24). In comparison to the ramp time, the reduction of the global maximum is limited by the optimal recycle ratio (1.5 in the present case) with respect to the maximum methane content at the outlet, as discussed in subsection 5.3.1. In contrast, the ramp time has to increase by a factor 120 ($t_{ramp} = 120 \text{ s}$, cf. Fig. 5.23) to reach the same reduction of the global maximum, but a further reduction is possible (by about 42 K, if $t_{ramp} = 600 \text{ s}$). Therefore, the dynamic adaptation of the recycle ratio adds a further degree of freedom to smooth the transient reactor behaviour.

However, it has to be considered though, that the dynamic phenomena still occur, even if the recycle ratio is adapted (Fig. 5.25). This figure compares adaptation of the recycle ratio from $Rec = 1$ to 1.5 (grey lines) with a constant recycle ratio (black lines) during the load jump from 10 to $20 \text{ m}^3 \text{ h}^{-1}$ (STP). Additionally to the axial profile at the beginning (continuous line), the axial profiles at the time step of the global maximum occurrence

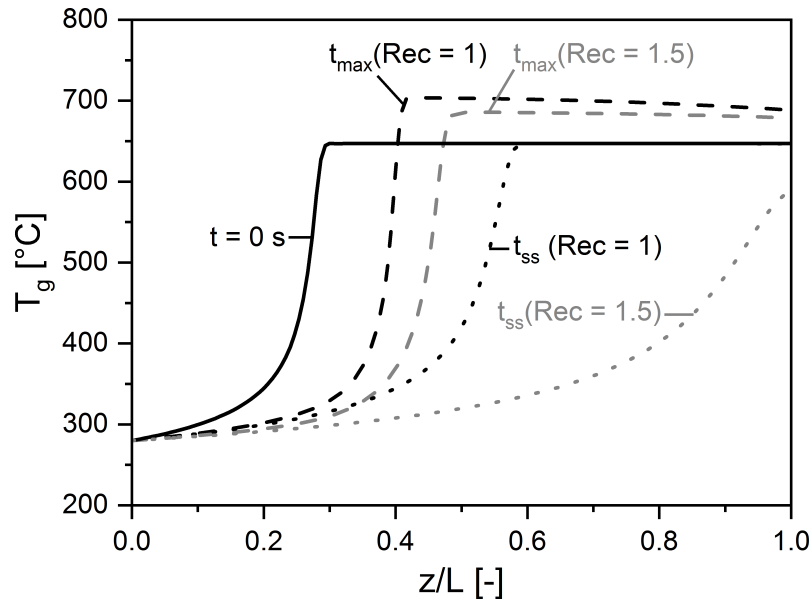


Figure 5.25: Axial profiles of the gas temperature T_g in the adiabatic reactor for different adaptations of the recycle ratio at the beginning ($t = 0$ s, continuous line), at the time step of the global maximum occurrence (t_{max} , dashed line), and at the new steady state (t_{ss} , dotted line) (volumetric flow rate increase \dot{V}_{in} from 10 to 20 m³ h⁻¹ (STP), $t_{ramp} = 1$ s, $Rec_{start} = 1$; $Rec_{end} = 1$ (black) and $Rec_{end} = 1.5$ (grey), respectively).

(dashed lines) and the new steady states (dotted lines) are plotted. For both cases, a global maximum occurs with a temperature maximum higher than the steady-state temperature maxima. But the global maximum of the gas temperature can be reduced by the adaptation of the recycle ratio.

6 Experimental verification

6.1 Load changes without product recirculation

The experimental verification was performed with two different synthesis plant settings as explained in detail in chapter 4 and section C.1. The slow load ramps, which were presented in subsection 6.1.1, were carried out with a short fixed-bed of the commercial Meth134 catalyst with an axial movable thermocouple in the centre, and a μ GC to analyse the gas composition. The continuous gas-analyser (EasyLine EL3020 from ABB) allowed for the increase in the load change velocity due to a shorter sampling time. Thus, fast load ramps (subsection 6.1.2) were researched with a longer fixed-bed with the multiple-thermocouple arrangement and the non-commercial 5 wt% Ni-catalyst facilitating the operation with undiluted inlet gas. In difference to the simulation results, it was not possible to measure the axial concentration profiles with the used gas analysis. The concentration of the dry product gas could be detected after the water separation only. For the results of this section, no product gas was recycled during the experiments ($Rec = 0$).

6.1.1 Slow load ramps

For the slow load ramps, the volumetric flow rate of the diluted inlet gas (70 vol% N_2) was increased by a ramp from 1.67 to 2.50 $L\ min^{-1}$ (STP) within four different ramp times (Fig. 6.1). The ramp times of 8, 20, 40 and 100 min resulted in a load change velocity between $v_V = 0.008\ L\ min^{-2}$ (STP) for 100 min and 0.104 $L\ min^{-1}$ (STP) for 8 min. The flow rate of 2.50 $L\ min^{-1}$ (STP) was held for approximately 60 min. For a ramp time of 100 min the holding time was reduced to 25 min to be able to conduct two experiments per day. Therefore, the data series ends at a normalized time (cf. Eq. 4.10) of 1.25 for this experiment. Fig. 6.2 shows the bed temperature at the end of the catalytic bed and the carbon dioxide conversion during the ramp, with different load change velocities. The steady-state results are marked with stars.

The influence of the volumetric flow rate ramp on the bed temperature is limited to a few Kelvin. The temporal behaviour of the temperature shows a characteristic trend for all studied load change velocities. The temperature increases by about 2 to 3 K first, passes a maximum, and decreases again. After the ramp ends, the bed temperature is in the range of the initial value but still unstable. As a result, the load change velocity barely affects the observed temperature increase as well as the temporal temperature development. The

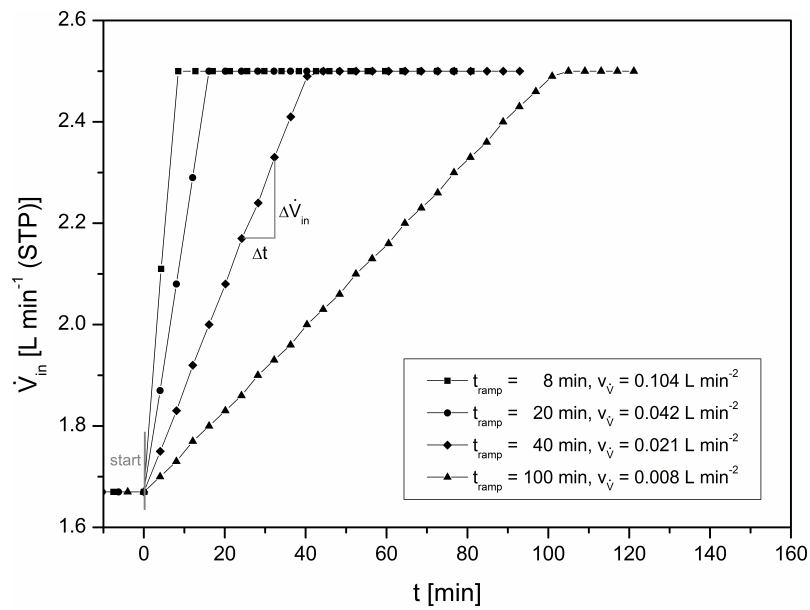


Figure 6.1: Ramps of the volumetric flow rate with different load change velocities v_V as a function of time t (\dot{V}_{in} from 1.67 to 2.5 L min⁻¹ (STP), $y_{N_2,in} = 70$ vol%, $(y_{H_2}/y_{CO_2})_{in} = 4$, $p_{in} = 1.8$ bar, $Rec = 0$, Meth134 catalyst).

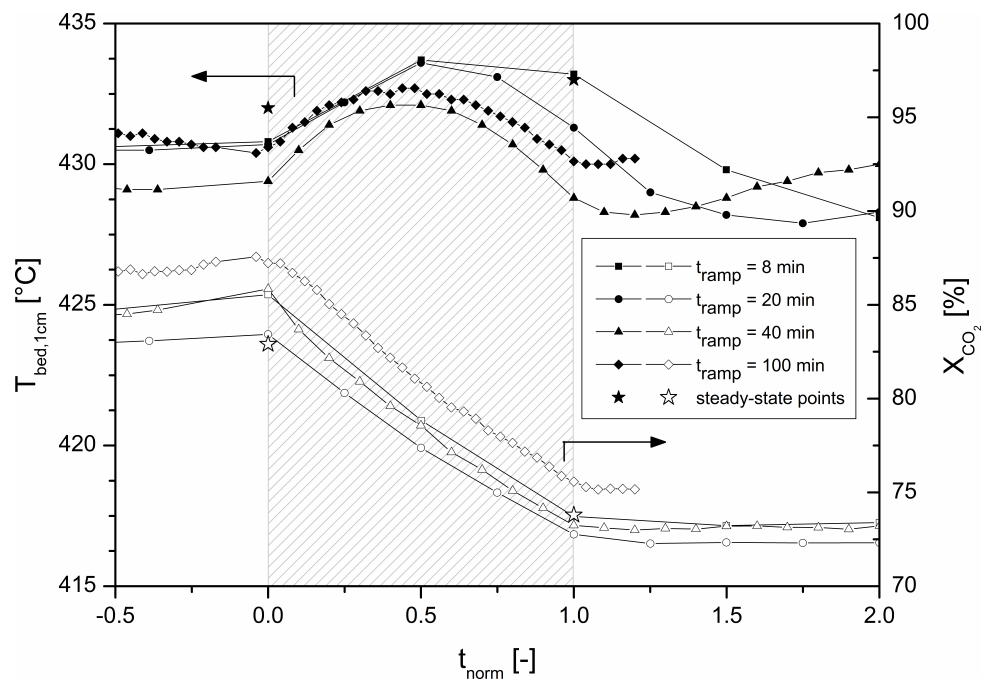


Figure 6.2: Bed temperature T_{bed} (left) and carbon dioxide conversion X_{CO_2} (right) as a function of normalized time t_{norm} for different load change velocities of volumetric flow rate v_V (conditions cf. Fig 6.1).

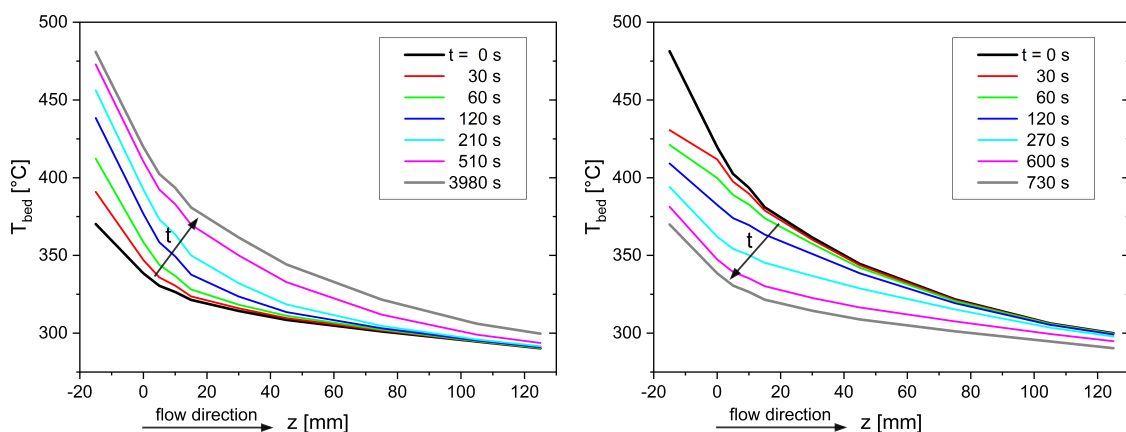


Figure 6.3: Time-dependent temperature profiles T_{bed} for a flow rate step \dot{V}_{in} from 0.5 to 1.25 L min⁻¹ (STP) (left) and from 1.25 to 0.5 L min⁻¹ (STP) (right) ($t_{ramp} = 1$ s, $y_{N_2,in} = 0$ vol%, $(y_{H_2}/y_{CO_2})_{in} = 4$, $p_{in} = 1$ bar, $Rec = 0$, 5 wt% Ni-catalyst).

relation between the carbon dioxide conversion and the normalized time is linear, and once again independent of the load change velocity. Furthermore, a stable steady state is immediately reached for the carbon dioxide conversion after the load change ends (at $t_{norm} = 1$). These results confirm the observations of Doesburg et al. (1976a) that the temperature response is slower than the concentration response. The temperature response is decelerated due to the heat storage of the catalytic bed and the reactor wall, whereas changes in concentration move approximately with the velocity of the gas flow.

For industrial methanation processes, a maximum and a minimum flow rate of the reactants should be determined, which could be handled by the reactor and the cooling system. As pointed out by Graf et al. (2014), load changes for fixed-bed reactors between 0.7 and 1 % min⁻¹ were recommended from a practical point-of-view.

6.1.2 Fast load ramps

For the fast load ramps, the volumetric flow rate of the undiluted inlet gas was increased by a ramp from 0.5 to 1.25 L min⁻¹ (STP) and decreased backwards after the steady state was reached. The ramp times of 1, 10, 30, 60, and 120 s that were applied resulted in a load change velocity between $v_{\dot{V}} = 0.375$ L min⁻² (STP) for 120 min, and 45 L min⁻¹ (STP) for 1 s.

The transition of the axial temperature profiles for the load step ($t_{ramp} = 1$ s) is shown in Fig. 6.3. Due to the axial dispersion of the catalyst bed and the thermocouple tube, the hottest measurement point was located upstream of the catalyst bed at $z = -15$ cm. Therefore, the global extrema (as detected by simulation) could not be measured. If the volumetric flow rate is increased, the temperature of the catalyst rose by about 80 K at $z = 0$ cm and vice versa. In accordance with the polytropic characteristic of the experimental

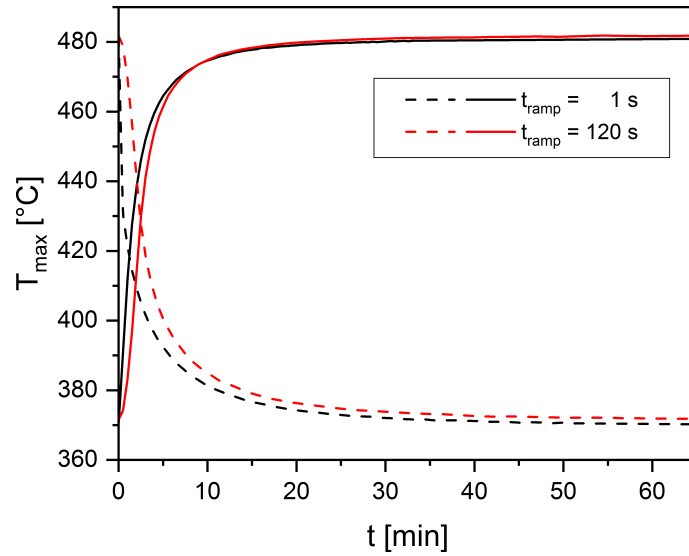


Figure 6.4: Temporal trend of the maximum gas temperature T_{max} at $z = -15$ cm in dependence of the ramp time t_{ramp} for flow rate ramps \dot{V}_{in} from 0.5 to 1.25 L min⁻¹ (STP) (continuous lines) and from 1.25 to 0.5 L min⁻¹ (STP) (dashed lines) ($y_{N_2,in} = 0$ vol%, $(y_{H_2}/y_{CO_2})_{in} = 4$, $p_{in} = 1$ bar, $Rec = 0$, 5 wt% Ni-catalyst).

reactor, the temperature increase is less pronounced at the end of the catalyst bed (12 K at $z = 105$ cm). The same axial temperature profile is reached after the backwards load step compared to initial steady state. The comparison of the maximal temperature between the fastest ($t_{ramp} = 1$ s) and slowest ramp ($t_{ramp} = 120$ s) in Fig. 6.4 shows that the heating up and cooling down, respectively, is slowed down by an increase of the ramp time, especially in the first 10 min. Afterwards, the trend of maximal temperature (at $z = -15$ cm) is rather similar and the steady states are almost independent of the ramp time. The thermal behaviour of the experimental reactor is not-idealised, and thus, the reactor dynamics is superimposed by axial dispersion and radial heat losses.

Additionally, the change of the methane content of the dry product gas in relation to the steady-state start value at 1.25 L min⁻¹ ($y_{CH_4} \approx 0.55$) is plotted in Fig. 6.5. If the volumetric flow rate is increased (left hand side), the methane content drops and converges asymptotically to the steady-state value. In contrast, if the inlet flow rate is decreased, the methane content drops, reaches a maximum, and converges asymptotically to the new steady state. If the ramp time is increased, the conversion drop (directly after the load step) can be reduced independently of the step direction, which can be used for process control. For the load decrease within 120 s (right hand side), the conversion drop is vanished. For very fast load changes up to $t_{ramp} = 30$ s, the response speed of the methane signal is similar, due to the dead time of the synthesis plant. It was proven during the result evaluation, that the change of the methane content is introduced by the load change of the volumetric flow rate and not caused by the technical equipment of the synthesis plant.

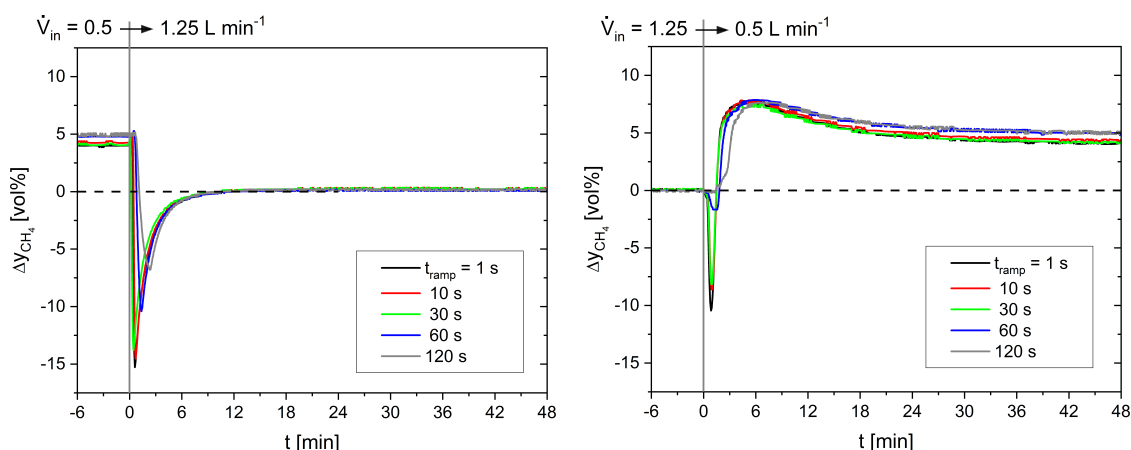


Figure 6.5: Temporal trend of the methane content changes Δy_{CH_4} (dry product gas, in comparison to the steady-state start value) in dependence of the ramp time t_{ramp} for flow rate ramps \dot{V}_{in} from 0.5 to 1.25 L min⁻¹ (STP) (left) and from 1.25 to 0.5 L min⁻¹ (STP) (right) ($y_{N_2,in} = 0$ vol%, $(y_{H_2}/y_{CO_2})_{in} = 4$, $p_{in} = 1$ bar, $Rec = 0$, 5 wt% Ni-catalyst).

In difference to the simulation results, the concentration of the dry product gas could be detected after the water separation only. Therefore, the measurement signal is already smoothed by dispersion in the reactor and upstream.

Based on simulations, the unsteady-state behaviour of the fixed-bed reactor was presented in the subsection 5.2.2. Load ramps of the volumetric flow rate led to global maxima in temperature and methane content during the transient period depending on whether the flow rate is increased or decreased. This dynamic phenomena is called a moving hot-spot. The temporal trend of the methane content changes Δy_{CH_4} in relation to the steady-state start value at the reactor outlet is plotted in Fig. 6.6. These are the simulation results of the adiabatic reactor without product recirculation at the reactor outlet ($z/L = 1$) for a positive and a negative flow rate step ($t_{ramp} = 1$ s, cf. Figure 5.13). As explained for the experimental results (Fig. 6.5), the simulation results show a local minimum if the volumetric flow rate is increased, and vice versa, a global extrema for a flow rate reduction at the reactor outlet. Furthermore, the simulations and the experiments show consistently that the local minimum of the methane content occurs faster than the global maximum. The idealised adiabatic reactor reaches the same steady-state value at the reactor outlet after the load change. However, the polytropic experimental reactor reaches another steady state (cf. subsection 5.1.2). The experimental verification with the fast load ramps cannot detect the temperature extrema due to dispersion processes in the fixed-bed and the non-adiabatic reactor. But after checking the methane content, it is expected that they occur in the catalyst bed.

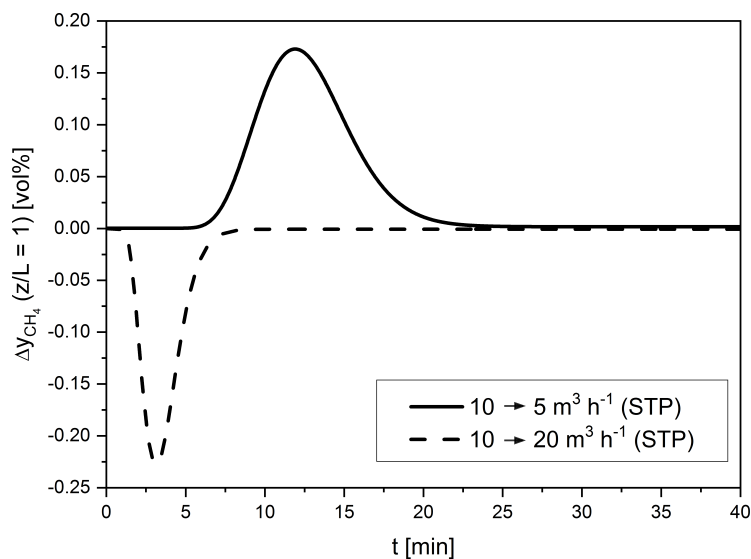


Figure 6.6: Temporal trend methane content changes Δy_{CH_4} (wet product gas, in comparison to the steady-state start value) in the adiabatic reactor ($Rec = 0$) for a positive and a negative flow rate step ($t_{ramp} = 1$ s). [Simulation results of Figure 5.13 in subsection 5.2.2]

Summary

Considering the unsteady-state behaviour without product recirculation, ramps of the volumetric flow rate with different load change velocities showed that the normalized reactor behaviour is independent of the load change velocity for slow load ramps. Thereby, the temperature response is significantly decelerated in contrast to the concentration response. Furthermore, the experiments with fast load ramps proved that moving hot-spots have to be considered, reaching the reactor outlet.

6.2 Product recirculation to control dynamic operation

At first, similar to the presentation of the simulation results with product recirculation, the influence on the steady-state behaviour is summarized in subsection 6.2.1. Then the control of the dynamic operation (by adapting the recycle ratio) is presented in subsection 6.2.2. All experimental results of this section except the last ones with the load steps (Fig. 6.9, second experimental series) were carried out with the short fixed-bed of the commercial Meth134 catalyst (first experimental series).

Table 6.1: Results of steady-state experiments and comparison with the chemical equilibrium (*italic*) for different recycle ratios Rec ($\dot{V}_{in} = 2.5 \text{ L min}^{-1}$ (STP), $y_{N_2,in} = 50 \text{ vol\%}$, $(y_{H_2}/y_{CO_2})_{in} = 4$, $p_{in} = 1.8 \text{ bar}$, Meth134 catalyst).

| Rec [-] | N ₂ | H ₂ | $y_{i,MR,out}$ [vol%] | | CO | H ₂ O | $\dot{n}_{out+H_2O,c}$ [10 ⁻⁵ mol s ⁻¹] | X_{CO_2} [%] | Y_{CH_4} [%] | $T_{bed,2cm}$ [°C] | $\bar{t}_{bed,eff}$ [s] |
|--------------|----------------|----------------|--------------------------|-----------------|------------|------------------|--|-------------------|-------------------|-----------------------|----------------------------|
| | | | CO ₂ | CH ₄ | | | | | | | |
| 0.5 | 56.9 | 19.4 | 2.7 | 6.8 | 0.7 | 13.5 | 162 | 72.4 | 69.1 | 493 | 0.013 |
| | <i>56.8</i> | <i>18.3</i> | <i>2.0</i> | <i>7.3</i> | <i>0.5</i> | <i>15.1</i> | <i>162</i> | | | | |
| 0.8 | 58.0 | 17.0 | 2.4 | 7.2 | 0.6 | 14.8 | 159 | 75.7 | 71.5 | 483 | 0.011 |
| | <i>57.1</i> | <i>17.5</i> | <i>1.9</i> | <i>7.6</i> | <i>0.4</i> | <i>15.6</i> | <i>161</i> | | | | |
| 1.6 | 58.1 | 16.6 | 2.3 | 7.4 | 0.6 | 15.0 | 159 | 77.0 | 73.4 | 437 | 0.008 |
| | <i>58.3</i> | <i>13.9</i> | <i>1.1</i> | <i>8.8</i> | <i>0.1</i> | <i>17.8</i> | <i>158</i> | | | | |

6.2.1 Influence on the steady-state behaviour

The recycle ratio Rec was varied between 0.5 and 1.6 at a constant volumetric flow rate of the diluted inlet gas of 2.50 L min^{-1} (STP) (Table 6.1). The chemical equilibrium can be reached for all analysed recycle ratios. Furthermore, the product separation by condensation shifts the thermodynamic equilibrium towards the products of the methanation reaction (CH₄, H₂O) (El-Sibai et al. 2015). For a constant inlet flow rate, an increase of the recycle ratio affects the reactor system in two ways: the residence time in the reactor is reduced and the feed gas is diluted by product prior to entering the reactor. Both effects result in a higher heat capacity flow rate in the reactor, a lower residence time, and an improved heat transfer between the packed-bed and reactor wall. Consequently, the bed temperature is significantly lowered (from 493 to 437 °C) with increasing recycle ratio from 0.5 to 1.6. The carbon dioxide conversion and the methane yield increase slightly by increasing the recycle ratio (cf. Table 6.1), since the positive effect of a lower temperature overcompensates the negative effect of a smaller residence time. However, the aforementioned effects of the product recirculation are influencing each other, especially in the selected polytropic reactor system.

6.2.2 Control of dynamic operation

In the next step, the inlet flow rate ramp and the product recirculation were analysed together to compare their contrary effect on the methanation reactor qualitatively. Thus, the same variation of the volumetric inlet flow rate from 1.67 to 2.5 L min^{-1} (STP) is used (cf. subsection 6.1.1). For a better interpretation of the results, a lower nitrogen dilution of 50 vol% was chosen. Two experimental settings with transient recycle ratios and different load change velocities were conducted (Table 6.2). In the first experiment, the volumetric flow rate of the product recirculation was set constant, leading to a decreasing recycle ratio

Table 6.2: Ramp time t_{ramp} and variation of the recycle ratio Rec for the unsteady-state experiments with product recirculation (\dot{V}_{in} from 1.67 to 2.5 L min⁻¹ (STP), $y_{N_2,in} = 50$ vol%, $(y_{H_2}/y_{CO_2})_{in} = 4$, $p = 1.8$ bar, Meth134 catalyst).

| Experiment | t_{ramp} [min] | Rec_{start} [-] | Rec_{end} [-] | ΔRec [-] |
|-------------------|---------------------|----------------------|--------------------|---------------------|
| # 1 | 40 | 0.80 | 0.30 | -0.05 |
| # 2 | 24 | 0.95 | 1.08 | 0.13 |

Rec from 0.8 to 0.3. In the second experiment, the recycle ratio was kept constant within the margin of 0.95 and 1.08.

The bed temperature at a position of 2 cm as well as the carbon dioxide conversion and the methane yield during these dynamic experiments are shown in Figs. 6.7 and 6.8, respectively. If the recycle flow rate stays constant (experiment # 1), the bed temperature rises about 32.2 K with increasing inlet flow rate and stays constant after the change period. In contrast, if the recycle ratio is almost constant (experiment # 2), the bed temperature increases only about 8 K during the ramp, passes a maximum, and falls again to a value slightly above the initial value.

Thus, the adaptation of the recycle flow rate stabilizes the temperature profile. Consequently, if a recycle reactor is applied, high load change velocities can be realized without approaching critical temperatures inside the methanation reactors. Most probably, the load change velocity can be further increased, if the recycle flow rate is adapted disproportionately, as done by the simulations in the subsection 5.3.3.

The carbon dioxide conversion as well as the methane yield decreased for the experimental settings. Both follow the trend of the steady-state parameter variation of the inlet flow rate without product recirculation (cf. Table 6.2). The comparison between both experiments shows that the decrease in conversion is stronger pronounced in the case of a decreasing recycle ratio (experiment # 1). This effect might be explained by the higher bed temperature and the related shift of the chemical equilibrium towards lower conversions. This observation is consistent with the results of the methane yield. Thus, cooling the reactor through the product recirculation is beneficial for a high carbon dioxide conversion and methane yield during flexible operation.

Finally, the adaptation of the product recirculation was verified with the continuous gas-analyser and the non-commercial 5 wt% Ni-catalyst. The volumetric flow rate jumped from 1.25 to 0.5 L min⁻¹ (STP) and backwards after the steady state was reached. In-between, the recycle ratio was adapted ($Rec = 1.9 \rightarrow 3.43$ and backwards, Figure 6.9). In comparison to the unsteady-state experiment without product recirculation the methane content shortly increases for the reduction of the volumetric flow rate and vice versa. The educt gases (H₂ and CO₂) show the opposite trend highlighting the changes of the conversion. By

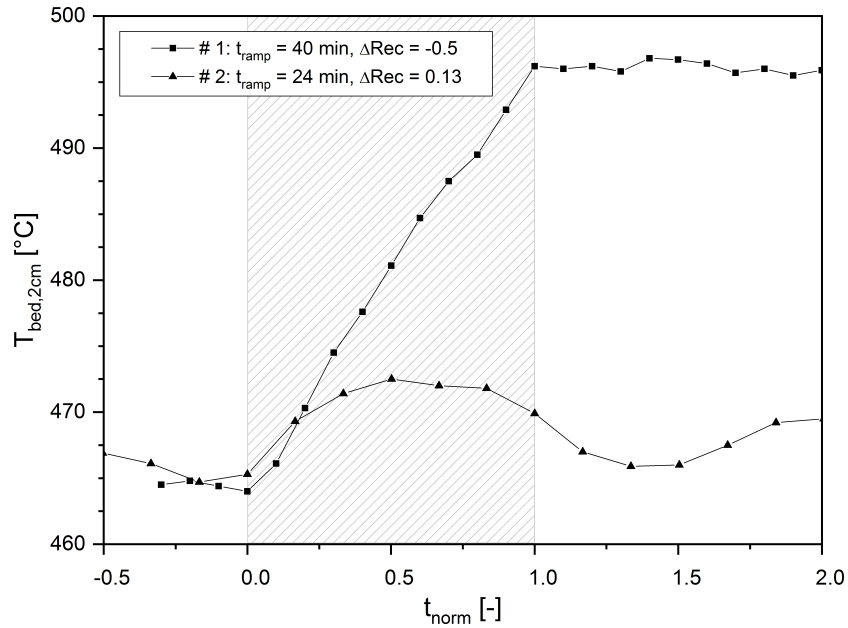


Figure 6.7: Bed temperature T_{bed} as a function of normalized time t_{norm} for the ramps of the volumetric flow rate with product recirculation (\dot{V}_{in} from 1.67 to 2.5 L min⁻¹ (STP), $y_{N_2,in} = 50$ vol%, $(y_{H_2}/y_{CO_2})_{in} = 4$, $p = 1.8$ bar, Meth134 catalyst).

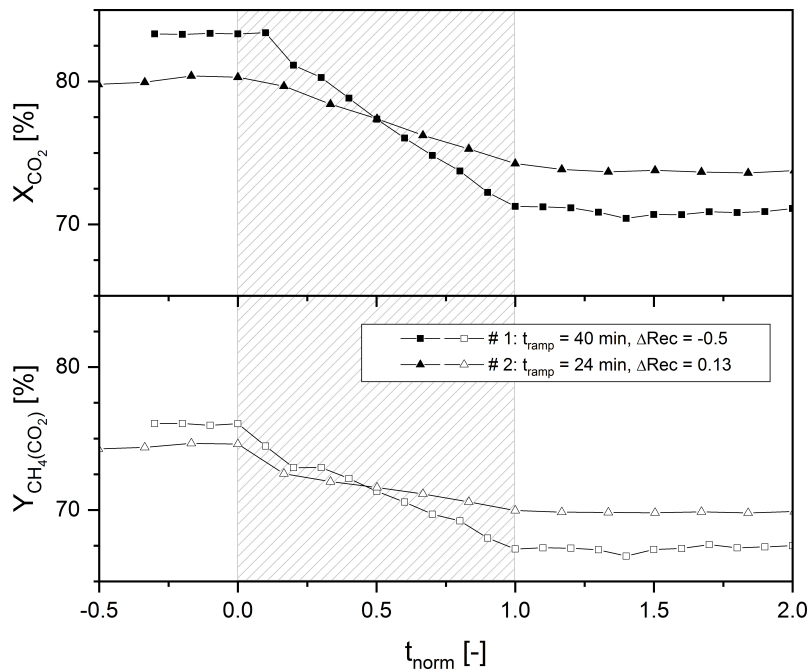


Figure 6.8: Carbon dioxide conversion X_{CO_2} (top) and methane yield Y_{CH_4} (bottom) as a function of normalized time t_{norm} for the ramps of the volumetric flow rate with product recirculation (conditions cf. Fig 6.7).

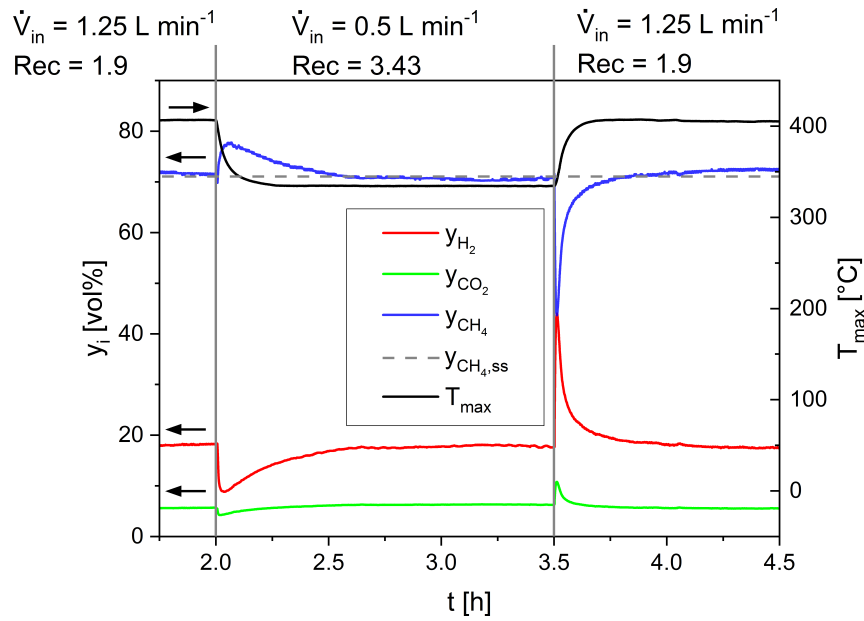


Figure 6.9: Temporal trend of the dry product gas y_i and the maximal bed temperature T_{max} for a flow rate step ($t_{ramp} = 1$ s) from $\dot{V}_{in} = 1.25$ to 0.5 L min^{-1} and backwards with an adaptation of the recycle ratio ($y_{N_2,in} = 0$ vol%, $(y_{H_2}/y_{CO_2})_{in} = 4$, $p_{in} = 1$ bar, 5 wt% Ni-catalyst).

adapting the recycle ratio, the steady-state values of the methane content can be held almost constant at 72 vol% (grey-dashed line) independently of the volumetric inlet flow rate. This shows that the recycle ratio can also be used to level concentration differences in short polytropic reactors.

Summary

It could be shown, that the combination of the flow rate ramps and the product recirculation enables the manipulation of the bed temperature and consequently the reactor stability during dynamic operation. To handle the variations of the inlet flow rate, the adaptation of the product recirculation is unavoidable for a high conversion of carbon dioxide. The recycle ratio can also be used to control the outlet concentration of short polytropic reactors at the steady state.

7 Conclusion for unsteady operation

The previously presented results in chapter 5 regarding simulations and in chapter 6 for experimental verification are now summarized with respect to the load flexibility (section 7.1), and the design criteria for the unsteady-state operation with emphasis on fixed-bed recycle reactors (section 7.2). Finally, operation and control strategies are derived in the section 7.3.

7.1 Load flexibility

This term quantifies the potential of processes or reactors for transient operation between different steady states in a wide operating-window without imperilling the process safety (cf. subsection 2.3.1). The four aspects of the load flexibility are the load range, the start-up and shutdown times, the load change velocity, and the limitations of load changes.

Methodology

The *load range* is primarily determined by the temperature borders of the reactor material, the cooling medium, and the catalyst (a lower limit for the ignition temperature and an upper limit for the stability of the catalyst). The load range can be determined by analysing the axial profile of the gas temperature at the steady state. The gas temperature is recommended, since it can be measured easier (e.g. by a multi-point thermocouple) in comparison to the axial profile of the methane content. However, due to the presence of dynamic phenomena as presented for the moving hot-spots (cf. sections 5.2 and 6.1), additional unsteady-state results are required, if the reactor has to deal with fast load changes or operates near the operation limits. Dynamic experiments are necessary to derive the *start-up time* and the *shutdown time* depending on the initial state. If simulation experiments are conducted, it is important that all parts of the reactor are included (e.g. the reactor wall or flanges), because the start-up and shutdown time are influenced by the reactor size (the existing thermal storage masses) and the steady-state temperature level as shown in the subsection 5.2.1. For a comprehensive analysis of the *load change velocity* the constraints of all plant components and materials (e.g. temperature gradients or limits) have to be taken into account, since there can be other limiting factors beside the chemical reactor. The results of this thesis focuses on the dynamically-operated reactor

only, and excludes, for example, the residence time of the product recirculation or the load change velocity of the recycle compressor.

Results

Regarding the *load range*, adiabatic reactors can operate well with partial and excess load because the chemical equilibrium is reached. Thus, the reaction zone is shorted or extended in the reactor by load changes, but the outlet temperature and composition of the product gas at steady state is not influenced. Nevertheless, the adiabatic temperature rise leads to high reactor temperatures and reactor cooling via the recirculation of product gas is necessary. For cooled reactors, the load range is limited, since they react very sensitively to changes of the inlet parameters, and have the tendency to form hot-spots. The product recirculation can be used to expand the load range of cooled reactors.

The *start-up time* and the *shutdown time*, respectively, depend on the steady-state temperature level. Thus, the start-up time of the cooled fixed-bed reactors is considerably faster compared to adiabatic reactors, because less energy has to be provided by the reaction to heat-up the reactor, and to reach the steady state. Moreover, the reactor dynamics are accelerated by the recirculation of product gas.

The experiments with temporally-varying inlet parameters have shown that dynamic phenomena have to be considered for the methanation in fixed-bed reactors and therefore for similar syntheses in Power-to-X processes as well. Exemplary for the variation of the inlet flow rate, its reduction leads to a drop of the temperature in the reactor, and a short-term maximum of the methane content. In contrast, an increase of the volumetric flow rate introduces a transient rise of the temperature and a reduction of the methane content. The global maxima can be explained by the axial shift of the reaction zone and the corresponding changes of the reaction rate being experimentally verified and in accordance with the literature. This dynamic phenomenon is called a moving hot-spot. The impact of load changes on the reactor dynamics is more pronounced for steep changes (steps), rather than for long ramp times – meaning that the *load change velocity* decreases.

7.2 Design criteria

The reactor design influences the load flexibility of methanation reactors significantly. Important design criteria cover the reactor dimension (diameter, length, and wall thickness), the catalyst (activity, size, and bed porosity), as well as the reactor cooling (heat exchange area, kind of coolant, and its flow rate), or the reactor isolation. In comparison to adiabatic reactors, cooled methanation reactors have to be longer in length and smaller in diameter, but they can reach higher conversions. Cooling concepts, which are applied in the industry for the methanation, are the water cooling or the molten-salt cooling (Rönsch et al. 2016b).

The counter-flow cooling enables a fast heat-up of the inlet stream in the reactor and therewith low inlet temperatures, as well as an intensive cooling at the reactor outlet. Nevertheless, cooled reactors show a high parametric sensitivity with the tendency to ignition and extinction phenomena and to a sharp hot-spot formation (cf. section 5.1). Adiabatic reactors can be designed as multi-bed reactors allowing the separation of water or the interstage cooling. One other option is to reduce the inlet temperature, leading to a reduction of the outlet temperature simultaneously, since the chemical equilibrium is reached. Moreover, reactor concepts with two stages are recommended for a methane content of the dry product gas above 99 % (Schollenberger et al. 2018). The heat utilisation concept can influence the reactor design as well, because it can be recovered on a higher temperature level for adiabatically-operating reactors in a downstream heat exchanger.

An optimal recycle ratio exists for adiabatic reactors. If the optimal recycle ratio is not adjusted, a disproportional adaptation of the recycle ratio is favoured for adiabatic reactors. During the unsteady-state operation, transient extrema reach the reactor outlet and influence the downstream process units leading to dynamic feedback if product gas is recycled. In other words, the product gas recycle represents a physical unsteady-state feedback loop between the reactor outlet and its inlet with respect to the gas composition, but no sustained moving hot-spots were detected for adiabatic reactors. The amplitude of the dynamic feedback at the reactor inlet is lower compared to the outlet, due to the mixing of the recycle with fresh feed gas. Depending on the specific design of the recycle, an additional temperature feedback may also occur, if insufficient heat exchanging capacity is installed. The impact of the feedback also depends on the residence time in the recycle line and the presence of a gas separation unit, which was neglected in this thesis. The recirculation of product gas helps to mitigate the dynamic phenomena by reducing the value of the global maximum. The dynamic adaptation of the recycle ratio adds a further degree of freedom in order to smooth the transient reactor behaviour.

7.3 Operation and control strategies

The results have highlighted the complexity of the unsteady-state operation introducing a challenging control task. Load ramps, especially of the volumetric flow rate, lead to a transition of the reaction zone inside the reactor. This should be considered, if the measurement point for the reactor control should be selected. In particular, cooled reactors form a narrow and sharp hot-spot, which might be overlooked if the outlet parameters were measured only. Furthermore, the high process sensitivity of cooled reactors can only be compensated by a fast and effective process control or the operation in a strong kinetically-limited region. In contrast, if the chemical equilibrium is reached in the reactor, being the case for adiabatic reactors, the outlet conditions can be easily predicted on the basis of thermodynamics with little effort in reactor-scale simulations.

Hereinafter, it shall be discussed if a quick-reacting and a slow-reacting reactor dynamics is favoured, respectively. The decision must be taken in coordination with the whole process design and the kind of fluctuations of the inlet parameters, which are economically-influenced by the power-to-gas process (Aicher et al. 2014). Slow-reacting reactors have usually larger reactor dimensions, and consequently longer start-up times. Additionally, they can be used as thermal storages, enabling the heat storage over several hours (Rönsch et al. 2017). Dynamic and quick-reacting reactors have lower thermal masses and shorter start-up times indicating that they are available faster. Furthermore, a fast reactor control is required, but they can better react to variations of the inlet parameters.

As described above, the product recirculation is an important control parameter for fixed-bed reactors during the steady-state and the unsteady-state operation. The presented proportional adaptation of the recycle ratio with respect to the flow rate ramp can be easily realized by a proportional controller providing stable behaviour of the control loop. For further investigations, an impulse-like adaptation of the recycle ratio during the global maximum, the implementation of a PID controller for the recycle flow rate, or the utilization of model-predictive control (MPC) approaches would be highly interesting for future research. Especially the latter option requires a sophisticated understanding of the occurring dynamic behaviour in order to derive an appropriate model simplification as basis for MPC (Rhein et al. 2014), which can be solved faster and with a higher accuracy with the determination of the hot-spot temperature.

As shown in the literature by Eigenberger et al. (2007), the understanding of the dynamic phenomena is important for the process control. For example, if the wrong-way behaviour occurs for a reduction of the inlet temperature, the process control system might reduce the inlet temperature even further to reduce the introduced hot-spot. But this accelerates the hot-spot formation in the reactor. Therefore, suitable control strategy can be the adaptation of the recycle ratio for a short-time in the opposite direction compared to the flow rate. This will probably counteract the transition of the reaction zone and thereby the formation of the global extrema.

7.4 Application of the results

The main results based on the conclusion of this chapter and their possible applications are:

- The term **load flexibility** was defined and a methodology was suggested for how the different aspects (load range, start-up/ shutdown time, and load change velocity) can be derived. The load flexibility of adiabatic and cooled fixed-bed recycle reactors was determined on the basis of steady and unsteady state experiments. All aspects of the load flexibility have to be considered. Thus, a weighting between the different aspects cannot be given in general, since it depends on the required specifications.

The derived methodology can be used subsequently to compare the load flexibility of different reactor types, for example fluidized-bed with fixed-bed reactors.

- The sensitivity analysis shows, that the **reactor design** influences the load flexibility significantly and that the product recirculation is an important control parameter for fixed-bed reactors in the steady-state as well as the unsteady-state operation. These results give fundamental hints about the selection of the reactor type and the reactor design for industrial applications of dynamic operating synthesis reactions.
- In context of **operation and control strategies**, the unsteady-state operation introduces a challenging control task, whereat the understanding of the dynamic phenomena is important for the development of the process control. Moreover, it was discussed in which cases a quick-reacting and a slow-reacting reactor dynamics is favoured, respectively. The adaptation of the product recirculation during load changes can be fulfilled in a more sophisticated manner by process controllers, for example by a model-predictive controller.

8 Summary and outlook

8.1 General conclusion

The aim of this thesis was to investigate the unsteady-state operation of a fixed-bed recycle reactor for the methanation of carbon dioxide. Therefore, simulation experiments based on a dynamic (multiphase, 1D) reactor model and physical experiments at a lab-scale synthesis plant were conducted. In the first step, a system characterisation and a validation took place, based on experiments with temporally constant inlet parameters. Reactor cooling, the recycle ratio, and inlet parameters were varied. In the second step, the dynamic behaviour was analysed in dependence of inlet load ramps without product recirculation. Finally, it was proven how the product recirculation influences the dynamics of a fixed-bed reactor. The main observations of these experiments are:

- The reactor design and cooling influence the load flexibility of methanation reactors significantly. For example, on the one hand, the start-up time (until the steady state is reached) is influenced by the reactor sizes and the existing thermal storage masses. On the other hand, the lower the steady-state temperature level, the lower the start-up time is. Thus, the start-up time of the cooled fixed-bed reactor is considerably faster compared to adiabatic reactors, because less energy has to be provided by reaction enthalpy to heat-up the reactor and to reach the steady state.
- Regarding the variation of inlet parameters, cooled reactors have a very high process sensitivity, which limits the load range and which can only be compensated by a fast and effective process control. Adiabatic reactors can be operated well with partial and excess load, because chemical equilibrium is reached by short reactor lengths. But they reach a high adiabatic temperature level and therefore have to be cooled by the recirculation of product gas.
- The experiments with temporally varying inlet parameters have shown that dynamic phenomena have to be considered for the methanation in fixed-bed reactors and consequently for similar syntheses in Power-to-X processes as well. Exemplary for the variation of the inlet flow rate, a reduction leads to a drop of the temperature in the reactor and a short-term maximum of the methane content. In contrast, an increase of the volumetric flow rate introduces a transient rise of the temperature and a reduction of the methane content. The intensity of dynamic phenomena can be reduced if the gradient of the load change is decreased.

- The experimental validation has shown that the normalized reactor behaviour is independent of the load change velocity for slow load ramps. The experiments with fast load ramps proved that moving hot-spots and dynamic phenomena in general have to be considered.
- For adiabatic reactors, an optimal recycle ratio exists. Even though the product recirculation influences the conversion in cooled reactors negatively, it reduces the process sensitivity and thus the load range can be expanded. Moreover, the experimental validation has shown that the recycle ratio can also be used to control the outlet concentration of short polytropic reactors at the steady state.
- For unsteady operating adiabatic reactors, the transient extrema reach the reactor outlet. Therefore, the product recirculation leads to a dynamic feedback. By increasing the recycle ratio to the optimal value during the load ramp, the transient extrema can be lowered.

Hence, the product recirculation is an important control parameter for fixed-bed reactors during the steady-state and the unsteady-state operation. Additionally, this work summarised design criteria for methanation reactors in the PtG process and derived operation strategies under dynamic conditions as the basis of controller development.

8.2 Future work

Based on the dynamic analysis of the fixed-bed recycle reactor from a reactor point-of-view, this thesis highlights the complexity of the unsteady-state operation and in many ways provides the starting point for further investigations. Some of the future research challenges will be described in detail.

The dynamic simulation model can be extended by the axial dispersion for mass and heat to improve the comparability with the experimental results and to analyse how dynamic phenomena are covered and possibly reduced in practice. Furthermore, a transient kinetics can be integrated, which includes the adsorption at the catalytic surface and the changes in activity under dynamic conditions. But a transient kinetics for the methanation is not published in the literature thus far. Even there is no general methodology for determining a transient kinetic model. Furthermore, the presented reactor model can be integrated in a dynamic flow sheet simulation of a whole power-to-gas process chain with ancillary units like the gas mixing or the downstream gas conditioning. This would allow analysing the consequences of the reactor dynamics and controlling on the process dynamics. Moreover, the flow sheet simulation can be used for an economic evaluation of the unsteady-state operation including investment and operation costs, in comparison to the plant design for the steady-state operation. An economic evaluation can be quantified the financial benefits and drawbacks of the unsteady-state operation.

Additionally, the presented simulation results can be extended. The analysis of the load range for the adiabatic and the cooled reactor was conducted exemplary for a pilot scale. A specific reactor in industrial scale can be simulated to gain results for the industrial practice. The methodology can be transferred to other reactor types as well to select the reactor which is the best suited for the dynamic requirements of the process. Furthermore, the principle analysis of the dynamic behaviour in the adiabatic reactor can be enlarged to other inlet variations beside linear ramps and beside the variation of the volumetric flow rate. For example, sinusoidal or stochastic variation of any inlet parameter (volumetric flow rate, temperature, pressure, and composition) can help to understand the fundamental principles of the reactor dynamics and the influence of the fluctuating hydrogen supply in the PtG process, respectively. Similarly, the product recirculation can be adapted in a more sophisticated manner, e. g. by a process controller.

The reactor with the split-tube furnace in the lab-scale test facility was a compromise solution, which was easy to construct and fillable with catalyst. However, the undefined polytropic characteristic has limited the expressiveness of the results. On the one hand, the reactor construction can be changed to an almost adiabatic or a wall-cooled reactor. On the other hand, the experimental validation can be extended to an industrial reactor design without external heating. The lab-scale test facility was sufficient enough for a principle analysis of the reactor dynamics in a fixed-bed reactor, but it was not designed for an optimized conversion near the requirements of the natural gas grid.

A Fundamentals

A.1 Calculation of equilibrium composition

The equilibrium composition was calculated with a simplified equilibrium model implemented in GNU Octave. The equilibrium model is based on the element balances (Eqs. A.1 – A.3) and the equilibrium constants of the water-gas shift (WGS) $K_{eq,WGS}$ and steam methane reforming (SMR) $K_{eq,SMR}$ being the reverse reaction of the carbon monoxide methanation (Eqs. A.4 – A.5, Hiller et al. 2006, p. 14f.). The temperature dependence of the equilibrium constants is determined by a polynomial equation (Eq. A.6 and Table A.1).

$$\dot{n}_C = \dot{n}_{CO_2} + \dot{n}_{CO} + \dot{n}_{CH_4} = const. \quad (A.1)$$

$$\dot{n}_H = 2 \dot{n}_{H_2O} + 2 \dot{n}_{H_2} + 4 \dot{n}_{CH_4} = const. \quad (A.2)$$

$$\dot{n}_O = 2 \dot{n}_{CO_2} + \dot{n}_{CO} + \dot{n}_{H_2O} = const. \quad (A.3)$$

$$K_{eq,SMR} = \frac{p_{CO} p_{H_2}^3}{p_{CH_4} p_{H_2O}} = \frac{y_{CO} y_{H_2}^3}{y_{CH_4} y_{H_2O}} p^2 \quad [\text{bar}^2] \quad (A.4)$$

$$K_{eq,WGS} = \frac{p_{CO_2} p_{H_2}}{p_{CO} p_{H_2O}} = \frac{y_{CO_2} y_{H_2}}{y_{CO} y_{H_2O}} \quad [-] \quad (A.5)$$

$$\log K_{eq,j} = A + B T^{-1} + C \log T + D T + E T^2 \quad \text{with } T \text{ in [K]} \quad (A.6)$$

Table A.1: Polynomial constants of the equilibrium constants for steam methane reforming $K_{eq,SMR}$ and water-gas shift $K_{eq,WGS}$ (Hiller et al. 2006, p. 15).

| Equation | $K_{eq,SMR}$ | $K_{eq,WGS}$ |
|----------|---------------------------|----------------------------|
| A | -18.98177 | -8.000980 |
| B | -9520.569 | 2456.620 |
| C | 10.91012 | 1.984098 |
| D | $-0.319556 \cdot 10^{-2}$ | $-0.3329441 \cdot 10^{-3}$ |
| E | $0.3631894 \cdot 10^{-6}$ | $0.563315 \cdot 10^{-7}$ |

A.2 Model selection

Pseudohomogeneous or heterogeneous model

External transport limitation for the mass – Mears criterion I (Mears 1971)

$$\left| \frac{r_{eff} \rho_c d_c}{c_{g,i} k} \right| < \frac{0.3}{n} \quad (\text{A.7})$$

with n – reaction order

External transfer limitation for the heat – Mears criterion I (Mears 1971)

$$\left| \frac{-\Delta H_R r_{eff} \rho_c d_c}{T_g h_{gc}} \right| \cdot Ar < 0.3 \quad (\text{A.8})$$

with Ar – Arrhenius number

$$Ar = \frac{E_A}{R T_g} = \frac{\text{activation energy}}{\text{potential energy}} \quad (\text{A.9})$$

Internal transfer limitation for the mass – Weisz-Prater criterion (Weisz et al. 1954)

$$Da_{II} < \frac{1}{|n|} \quad (\text{A.10})$$

with Da_{II} – second Damköhler number

$$Da_{II} = \frac{r_{eff} \rho_c d_c^2}{4 D_{m,eff} c_{c,sur}} = \frac{\text{chemical reaction rate}}{\text{molar diffusion rate}} \quad (\text{A.11})$$

Internal transfer limitation for the heat – Anderson criterion (Anderson 1963)

$$\left| \frac{-\Delta H_R r_{eff} \rho_c d_c^2}{4 \lambda_{eff} T_{c,sur}} \right| \cdot Ar < 0.75 \quad (\text{A.12})$$

Axial dispersion

Mears criterion II (Mears 1976)

$$\left| \frac{n Da_I}{Pe_{ax,mass}} - \frac{Ar Da_{III}}{Pe_{ax,heat}} \right| < 0.05 \quad (\text{A.13})$$

with Da_I and Da_{III} – first and third Damköhler number

$$Da_I = \frac{r_{eff} \rho_c d_c}{u_s c_{g,i}} = \frac{\text{chemical reaction rate}}{\text{bulk mass flow rate}} \quad (\text{A.14})$$

$$Da_{III} = \frac{-\Delta H_R r_{eff} \rho_c d_c}{u_s \rho_g c_{p,g} T_w} = \frac{\text{liberated heat}}{\text{bulk transport of heat}} \quad (\text{A.15})$$

and with $Pe_{ax, mass}$ and $Pe_{ax, heat}$ – axial Peclet numbers

$$Pe_{ax, mass} = \frac{u_s d_c}{D_{e, ax}} \quad (\text{A.16})$$

$$Pe_{ax, heat} = \frac{\rho_g u_s c_{p,g} d_c}{\lambda_{e, ax}} \quad (\text{A.17})$$

$$Pe = \frac{\text{advective transport rate}}{\text{diffusive transport rate}}$$

Radial dispersion

Chu criterion (Chu et al. 1989)

$$\frac{d_r}{d_c} > 8 \quad (\text{A.18})$$

B Modelling and simulation

B.1 Derivative of the velocity

The convection term of the fixed-bed reactor model can be simplified, if the derivative of the superficial velocity is independent of the spatial coordinate (Eq. B.17). This simplification is derived on the basis of the material derivative of the density, the continuum equation, and the assumption of an incompressible flow in the following.

$$\frac{\partial u_s}{\partial z} = 0 \quad (\text{B.1})$$

Material derivative of the density

The material derivative of the density (Eq. B.2) consists of the partial derivative of the density representing the local rate-of-change (first term) and the convective rate-of-change (second term) (Toro 2009).

$$\frac{d\rho}{dt} = \frac{\partial\rho}{\partial t} + \underline{u} \cdot \nabla\rho \quad (\text{B.2})$$

Continuum equation

The mass $m(t)$ in a material fluid volume is conserved (Eq. B.3).

$$\frac{dm}{dt} = \frac{d}{dt} \int_{\tilde{V}} \rho(\underline{x}, t) dV = 0 \quad (\text{B.3})$$

Next, the Reynolds transport theorem for a fixed control volume is applied (Eq. B.4) and the resulting equation is transformed with the Gauss's theorem (divergence theorem) (Eq. B.5).

$$\frac{dm}{dt} = \int_V \frac{\partial\rho}{\partial t} dV + \int_A \rho \underline{u} \cdot \underline{n} dA = 0 \quad (\text{B.4})$$

$$\frac{dm}{dt} = \int_V \left(\frac{\partial\rho}{\partial t} + \nabla \cdot (\rho \underline{u}) \right) dV = 0 \quad (\text{B.5})$$

The validity of Eq. B.5 has to be fulfilled independent of the chosen volume and thus, it can be simplified to Eq. B.6.

$$\frac{\partial \rho}{\partial t} + \nabla \cdot (\rho \underline{u}) = 0 \quad (\text{B.6})$$

Combination of the material derivative of the density and the continuum equation

The material derivative of the density (Eq. B.2) and the continuity equation (Eq. B.6) are equalled and the chain rule (Eq. B.8) is applied.

$$\frac{d\rho}{dt} - \underline{u} \cdot \nabla \rho + \nabla \cdot (\rho \underline{u}) = 0 \quad (\text{B.7})$$

$$\nabla \cdot (\rho \underline{u}) = \underline{u} \cdot \nabla \rho + \rho \cdot \nabla \underline{u} \quad (\text{B.8})$$

$$\frac{d\rho}{dt} + \rho \cdot \nabla \underline{u} = 0 \quad (\text{B.9})$$

Assumption of an incompressible flow

An incompressible flow “occurs when the density of each infinitesimal mass of fluid does not change during motion[, which] [...] does not imply that the density is constant throughout the entire flow field, but only that the density of each mass element does not change as its motion proceeds” (Johnson 1998). In this case, the material derivative of the density of a volume element is equal to zero (Eq. B.10).

$$\frac{d\rho}{dt} = 0 \quad (\text{B.10})$$

The assumption of an incompressible flow can be applied for gases, if:

- the Mach number Ma is small ($Ma < 0.3$)¹. More precisely, the fluid velocity u should be smaller than 30 % of the sound velocity c .
- the pressure loss is small $\left(\frac{\Delta p}{p_0} \ll 1\right)$.
- the relative change of the velocity is very low $\left(\frac{\Delta \rho}{\rho_0} \ll 1\right)$.²

¹http://www.aiaa.rwth-aachen.de/vlueb/vl/technische_stroemungslehre/assign/uebung13.pdf (accessed 15.10.2017)

²http://www.mb.fh-stralsund.de/fss/pages/pg_lehre/FLM%20I/FLM%20I%20Grundlagen%20Ver%20WS2012-13.pdf (accessed 15.10.2017)

The Mach number Ma and the speed of sound for gases c were calculated to prove the validity of these assumptions.

$$Ma = u/c \quad (\text{B.11})$$

$$c = \sqrt{\kappa \tilde{R} T} \quad (\text{B.12})$$

with

$$\tilde{R} = \frac{R}{M_{mix}} \quad (\text{B.13})$$

$$\kappa = \frac{c_p}{c_v} = \frac{c_p}{c_p - \tilde{R}} \quad \text{for ideal gases} \quad (\text{B.14})$$

The estimation was conducted for the stoichiometric educt gas ($M_m = 10.4 \text{ g mol}^{-1}$) and three-atomic gases ($\kappa = 1.33$), whereby the heat capacity ratio has a very low pressure and temperature dependence. The sound velocity is 81 m s^{-1} for $300 \text{ }^\circ\text{C}$ and 907 m s^{-1} for $500 \text{ }^\circ\text{C}$, respectively. The fluid velocity is in the range of 1 m s^{-1} for the methanation in fixed-bed reactors and therefore, far below one-third of the sound velocity. Hence, the assumption of an incompressible fluid flow is satisfied.

Inserting the assumption of an incompressible flow (Eq. B.10) in the resulting continuity equation (Eq. B.9) leads to Eq. B.15.

$$\rho \cdot \nabla \underline{u} = 0 \quad (\text{B.15})$$

The density ρ of the fluid flow is unequal to zero, therefore $\nabla \underline{u}$ has to be zero (Eq. B.16).

$$0 = \nabla \underline{u} = \frac{\partial u_x}{\partial x} + \frac{\partial u_y}{\partial y} + \frac{\partial u_z}{\partial z} \quad (\text{B.16})$$

For a one-dimensional flow in the z direction, Eq. B.16 can be rewritten to:

$$\frac{\partial u_z}{\partial z} = 0 \quad (\text{B.17})$$

Due to the one-dimensional approach, fast velocity changes in the consequence of load changes cannot be compensated in all three spatial directions. Therefore, numerical phenomena can occur, which was shown by Güttel (2013).

B.2 Model parameters

The heat transfer coefficient h_g was determined by the Nusselt number for the fluid flow in packed-beds Nu_g (Eqs. B.18–B.21 Verein Deutscher Ingenieure 2006, Gj 1), which is valid for Reynolds numbers Re between $10^{-1} - 10^4$ and Prandtl numbers Pr in the range of $0.6 - 10^4$.

$$Nu_g = \frac{h_g d_c}{\lambda_g} \quad (\text{B.18})$$

$$Nu_g = [1 + 1.5 (1 - \varepsilon_{bed})] \cdot \left[2 + \sqrt{Nu_{lam}^2 + Nu_{turb}^2} \right] \quad (\text{B.19})$$

with

$$Nu_{lam} = 0.664 \sqrt{Re} \sqrt[3]{Pr} \quad (\text{B.20})$$

$$Nu_{turb} = \frac{0.037 Re^{0.8} Pr}{1 + 2.443 Re^{-0.1} (Pr^{2/3} - 1)} \quad (\text{B.21})$$

The heat capacity, viscosity and heat transfer coefficient of the gas mixture was calculated by polynomial equations (Eqs. B.22–B.24, coefficients $A - E$), the mixing rules of Wilke for the viscosity (Eq. B.25) and of Wassilijev for the heat transfer coefficient (Eq. B.26, Verein Deutscher Ingenieure 2006, Da and Dca), respectively.

$$c_{p,i} = A + B T + C T^2 + D T^3 + E T^{-2} \quad [\text{J kg}^{-1} \text{K}^{-1}] \quad (\text{B.22})$$

$$\eta_i = A + B T + C T^2 + D T^3 + E T^4 \quad [\text{Pa s}] \quad (\text{B.23})$$

$$\lambda_i = A + B T + C T^2 + D T^3 + E T^4 \quad [\text{W m}^{-1} \text{K}^{-1}] \quad (\text{B.24})$$

$$\eta_{g,mix} = \sum_{i_1} \frac{y_{i_1} \eta_{i_1}}{\sum_{i_2} y_{i_2} F_{i_1 i_2}} \quad \text{with } F_{i_1 i_2} = \frac{[1 + (\eta_{i_1}/\eta_{i_2})^{1/2} (M_{i_2}/M_{i_1})^{1/4}]^2}{\sqrt{8} (1 + M_{i_1}/M_{i_2})} \quad (\text{B.25})$$

$$\lambda_{g,mix} = \sum_{i_1} \frac{y_{i_1} \lambda_{i_1}}{\sum_{i_2} y_{i_2} F_{i_1 i_2}} \quad (\text{B.26})$$

Furthermore, the temperature dependency of the reaction enthalpy was considered by the Kirchhoff's law (Eq. B.27). Due to the high reaction temperature, the phase transition of water can be neglected. The integral of the Kirchhoff's law was solved according to Eqs. B.28–B.30 with $T_0 = 298 \text{ K}$ and the results for the methanation of carbon dioxide are presented in Figure B.1.

$$\Delta H_{R,j}(T) = \Delta H_{R,j}(T = 298 \text{ K}) + \int_{T=298\text{K}}^T \left[\sum_{i=1}^N \nu_i c_{p,i} \right] dT \quad (\text{B.27})$$

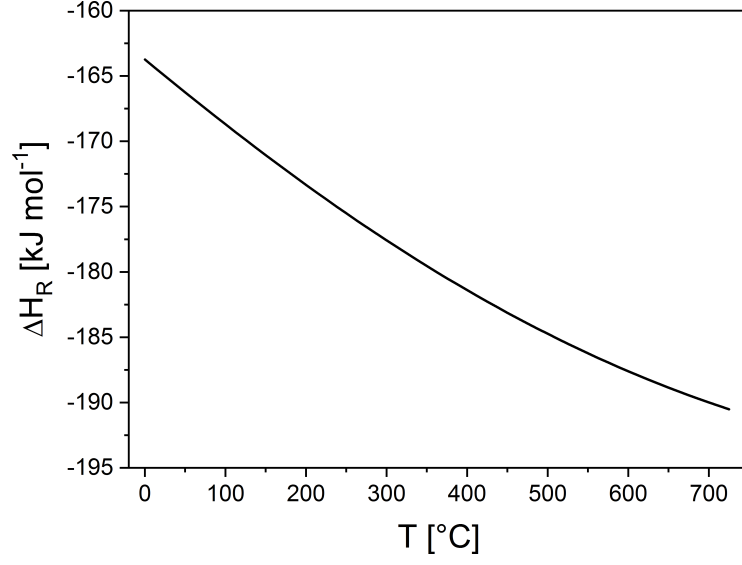


Figure B.1: Temperature dependence T of the reaction enthalpy ΔH_R for the CO_2 methanation.

$$\int_{T_0}^T \sum_{i=1}^N \nu_i \cdot c_{p,i} dT = \int_{T_0}^T \left[\left(\sum_{i=1}^N \nu_i \cdot A_i \right) + \left(\sum_{i=1}^N \nu_i \cdot B_i \right) \cdot T + \left(\sum_{i=1}^N \nu_i \cdot C_i \right) \cdot T^2 + \left(\sum_{i=1}^N \nu_i \cdot D_i \right) \cdot T^3 + \left(\sum_{i=1}^N \nu_i \cdot E_i \right) \cdot T^{-2} \right] dT \quad (\text{B.28})$$

$$\text{with } \sum_{i=1}^N \nu_i \cdot A_i = A^* \text{ for all coefficients} \quad (\text{B.29})$$

$$\begin{aligned} \int_{T_0}^T \sum_{i=1}^N \nu_i \cdot c_{p,i} dT &= \int_{T_0}^T (A^* + B^* \cdot T + C^* \cdot T^2 + D^* \cdot T^3 + E^* \cdot T^{-2}) dT \\ &= \left(A^* \cdot T + \frac{B^*}{2} \cdot T^2 + \frac{C^*}{3} \cdot T^3 + \frac{D^*}{4} \cdot T^4 - E^* \cdot T^{-1} \right) \Big|_{T_0}^T \quad (\text{B.30}) \\ &= A^* \cdot (T - T_0) + \frac{B^*}{2} \cdot (T^2 - T_0^2) + \frac{C^*}{3} \cdot (T^3 - T_0^3) \\ &\quad + \frac{D^*}{4} \cdot (T^4 - T_0^4) - E^* \cdot (T^{-1} - T_0^{-1}) \end{aligned}$$

Table B.1: Parametrisation of a and b for the friction factor f .

| Name | Parameter a | Parameter b | Valid for $\frac{Re_c}{1-\varepsilon_{bed}}$ |
|-------------------|---|---|--|
| Ergun | 150 | 1.75 | < 500 |
| Handley and Heggs | 368 | 1.24 | 1000 – 5000 |
| Tallmadge | 150 | $4.2 \left(\frac{1-\varepsilon_{bed}}{Re_c} \right)^{\frac{1}{6}}$ | 0.1 – 10^5 |
| Hicks | $f = 6.8 \frac{(1-\varepsilon_{bed})^{1.2}}{\varepsilon_{bed}^3} Re_c^{-0.2}$ | | 300 – 60 000 |

The pressure loss was described by the Ergun equation (Eq. B.31, Ergun 1952). For the friction factor the parametrisation of Ergun (1952), Handley et al. (1968), Tallmadge (1970), and Hicks (1970) were compared (Table B.1). The first two were neglected due to their small range of validity. The comparison between the latter two showed that the parameters of Hicks lead to a higher precision (Figure B.2).

$$p(z) = p_0 - \underbrace{\left[6.8 \frac{(1 - \varepsilon_{bed})^{1.2}}{\varepsilon_{bed}^3} Re_c^{-0.2} \right]}_f \frac{\rho_g u_s^2}{d_c} z \quad (\text{B.31})$$

with

$$Re_c = \frac{\rho_{g,mix} u_s d_c}{\eta_{g,mix}} \quad (\text{B.32})$$

$$f = \frac{1 - \varepsilon_{bed}}{\varepsilon_{bed}^3} \left(a \frac{1 - \varepsilon_{bed}}{Re_c} + b \right) = \frac{(1 - \varepsilon_{bed})^2}{\varepsilon_{bed}^3 Re_c} f_\nu \quad (\text{B.33})$$

$$f_\nu = a + b \frac{Re_c}{1 - \varepsilon_{bed}} \quad (\text{B.34})$$

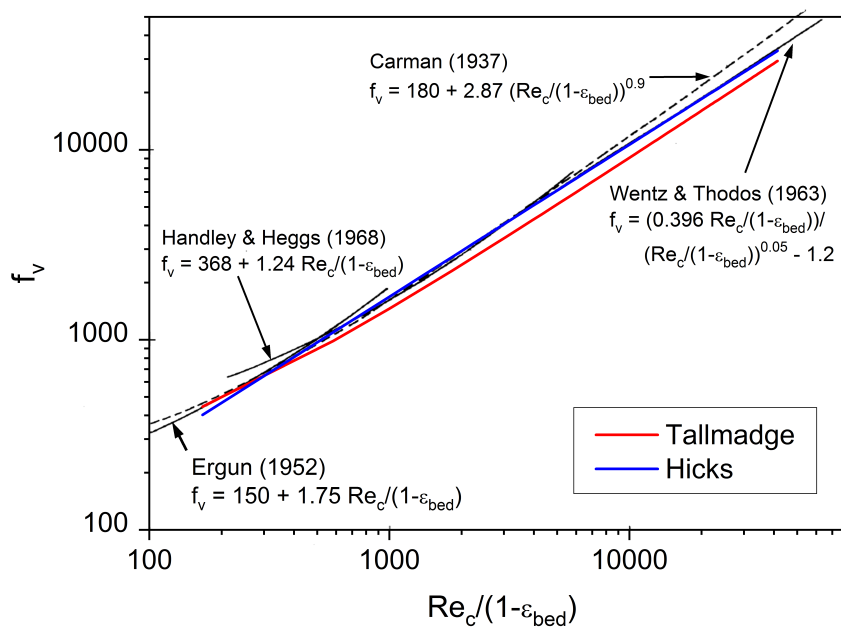


Figure B.2: Comparison of the parametrisation of viscous friction factor f_v calculated for $\varepsilon_{bed} = 0.4$; background figure from Hicks (1970).

B.3 Validation of the process sensitivity for cooled reactors

Schlereth et al. (2014) used amongst others an 1D pseudo-homogeneous, plug-flow reactor model and applied the kinetics of Xu et al. (1989a) being considerably less active compared to the kinetics of Koschany et al. (2016). For the validation, the parameters of Schlereth were integrated in the dynamic model described in chapter 3. The resulting Figure B.3 shows that the parametric sensitivity of the cooled fixed-bed reactor is representable by the simulation model and comparable to the results presented in literature.

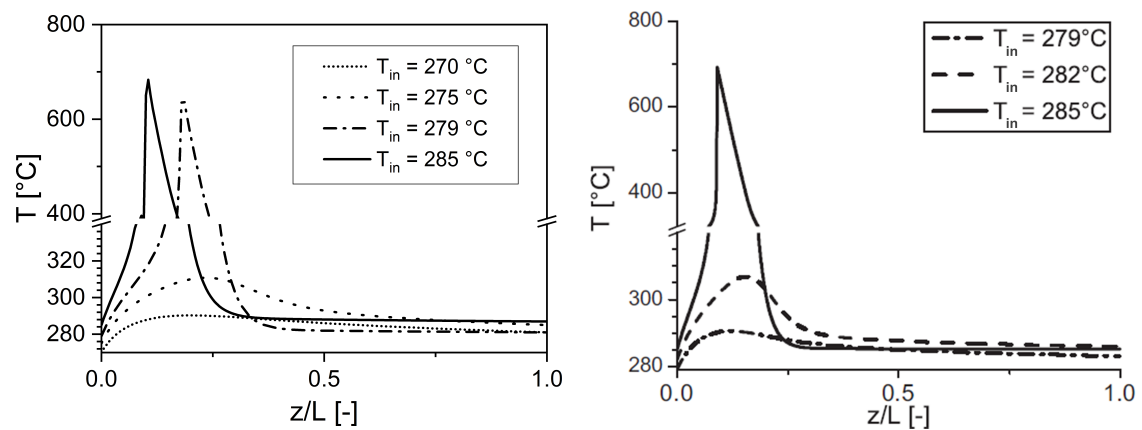


Figure B.3: Steady-state axial profiles of the gas temperature T for different inlet and reactor temperatures ($T_{in} = T_{cool}$) for the cooled reactor; parameters deviating from Table 3.2: $d_r = 2 \cdot 10^{-2}$ m, $\eta = 0.25$, $\dot{V}_{in} = 10.9$ m³ h⁻¹, $p_{in} = 10$ bar; original figure by Schlereth et al. (2014) (right).

B.4 Comparison of effectiveness and activity factor

The effectiveness factor of the catalyst pellet describes the intraparticle transport limitation. According to Baerns et al. (2006), the effectiveness factor was calculated with the Thiele modulus ϕ for spherical catalyst pellets (Eq. B.35). The Thiele modulus was determined by Eq. B.36, assuming first-order reaction kinetics for the limiting component carbon dioxide (comparable with Kiewidt et al. (2015)).

$$\eta(\phi) = \frac{3}{\phi} \left(\frac{\phi}{\tanh \phi} - \frac{1}{\phi} \right) \quad (\text{B.35})$$

$$\phi = \frac{d_c}{2} \sqrt{\frac{M_{CO_2} r_{v,CO_2}}{D_{eff,CO_2} \rho_{CO_2}}} \quad (\text{B.36})$$

The effective diffusivity D_{eff,CO_2} (Eq. B.37) considers the molecule-wall interactions (Knudsen diffusion D_{Kn} , Eq. B.38) and the molecular-molecular interactions (molecular diffusion D_m) (Krishna et al. 2012). The binary diffusion coefficients $D_{i_1 i_2}$ were calculated according to the empirical correlation of Fuller, Schettler and Giddings (Eq. B.39, Verein Deutscher Ingenieure 2006, Da27) and were used to predict the effective molecular diffusivity of carbon dioxide in the gas mixture according to Wilke's equation (Eq. B.40, EUROKIN 2011).

$$\frac{1}{D_{eff,CO_2}} = \frac{1}{D_{Kn,eff,CO_2}} + \frac{1}{D_{m,eff,CO_2}} \quad (\text{B.37})$$

$$D_{Kn,eff,CO_2} = \frac{\varepsilon_c}{\tau_c} \frac{d_c}{3} \sqrt{\frac{8 R T_g}{\pi M_{CO_2}}} \quad (\text{B.38})$$

$$\frac{D_{i_1 i_2}}{[\text{m}^2 \text{ s}^{-1}]} = \frac{3.2 \cdot 10^{-11} T^{1.75} [M_{i_1}^{-1} + M_{i_2}^{-1}]^{1/2}}{p \cdot 10^{-3} \left[\left(\sum \Delta v_{i_1} \right)^{1/3} + \left(\sum \Delta v_{i_2} \right)^{1/3} \right]^2} \quad (\text{B.39})$$

$$D_{m,eff,CO_2} = \frac{\varepsilon_c}{\tau_c} (1 - y_{CO_2}) \cdot \left(\sum_{i=1(i \neq CO_2)}^N \frac{y_i}{D_{CO_2,i}} \right)^{-1} \quad (\text{B.40})$$

with the diffusion volumes Δv_i [$10^{-6} \text{ m}^3 \text{ mol}^{-1}$]

(Verein Deutscher Ingenieure 2006, Da28)

| | | | | | |
|------------------|-----------------|-------------------|-------------------|-------------------|------------------|
| Δv_{H_2} | Δv_{CO} | Δv_{CO_2} | Δv_{CH_4} | Δv_{H_2O} | Δv_{N_2} |
| 6.12 | 18.0 | 26.9 | 25.14 | 13.1 | 18.5 |

A tortuosity $\tau_c = 3.54$ was taken from literature (Xu et al. 1989b) and a catalyst porosity of 0.37 was calculated for a commercial catalyst Meth134. For the simulation parameters

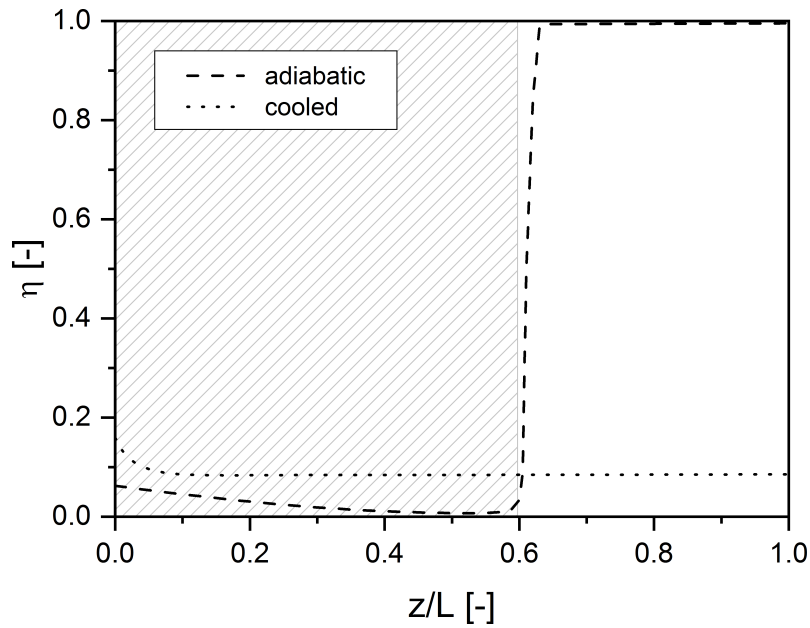


Figure B.4: Temperature- and pressure-dependent effectiveness factor η over the dimensionless reactor length for both reactor types (adiabatic reactor with the grey-marked reaction zone).

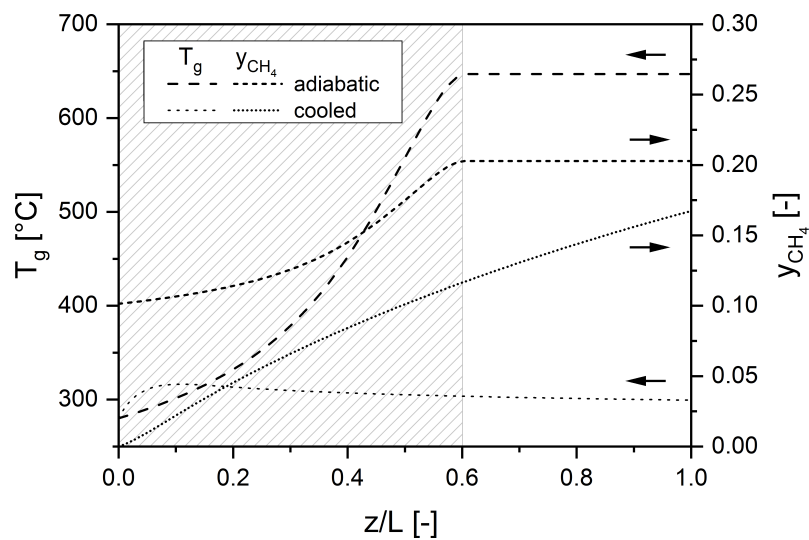


Figure B.5: Steady-state axial profiles of the gas temperature T_g and the methane content y_{CH_4} for both reactor types, considering the effectiveness factor of Figure B.4 (dashed: adiabatic reactor with the grey-marked reaction zone, dotted: cooled reactor).

presented in Table 3.2, the effectiveness factors over the reactor length for the adiabatic as well as the cooled reactor are shown in Fig. B.4. This more detailed calculation proves the estimation of a constant activity factor of 0.1, because the effectiveness factor, especially in the cooled reactor, is nearly constant over the whole reactor length. The effectiveness factor in the adiabatic reactor increases strongly, if the chemical equilibrium is reached. This increase of the effectiveness factor has almost no influence on the composition, because the reaction rate is close to zero downstream of the reaction zone (after the equilibrium is reached). Fig. B.5 presents the effect of the temperature- and pressure-dependent effectiveness factor on the gas temperature and the methane content. The comparison between Fig. 5.1 ($\eta = \text{const.}$) and this figure shows the extension of the reaction zone of the adiabatic reactor up to two-thirds of the reactor length. For the cooled reactor, the temperature maximum is reduced by 24.4 K compared to the simulation with a constant activity factor and the methane content decreases simultaneously.

C Experimental methods

C.1 Synthesis test facility

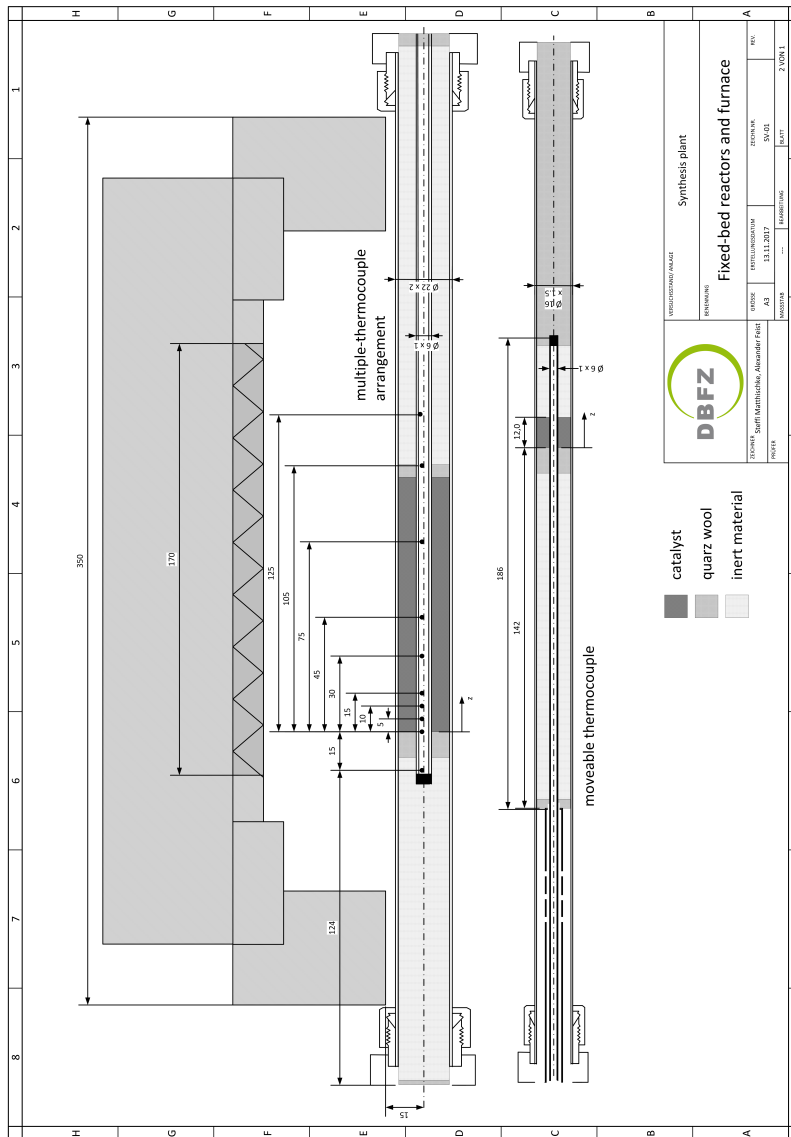


Figure C.1: Technical drawing of the fixed-bed reactors and the furnace.

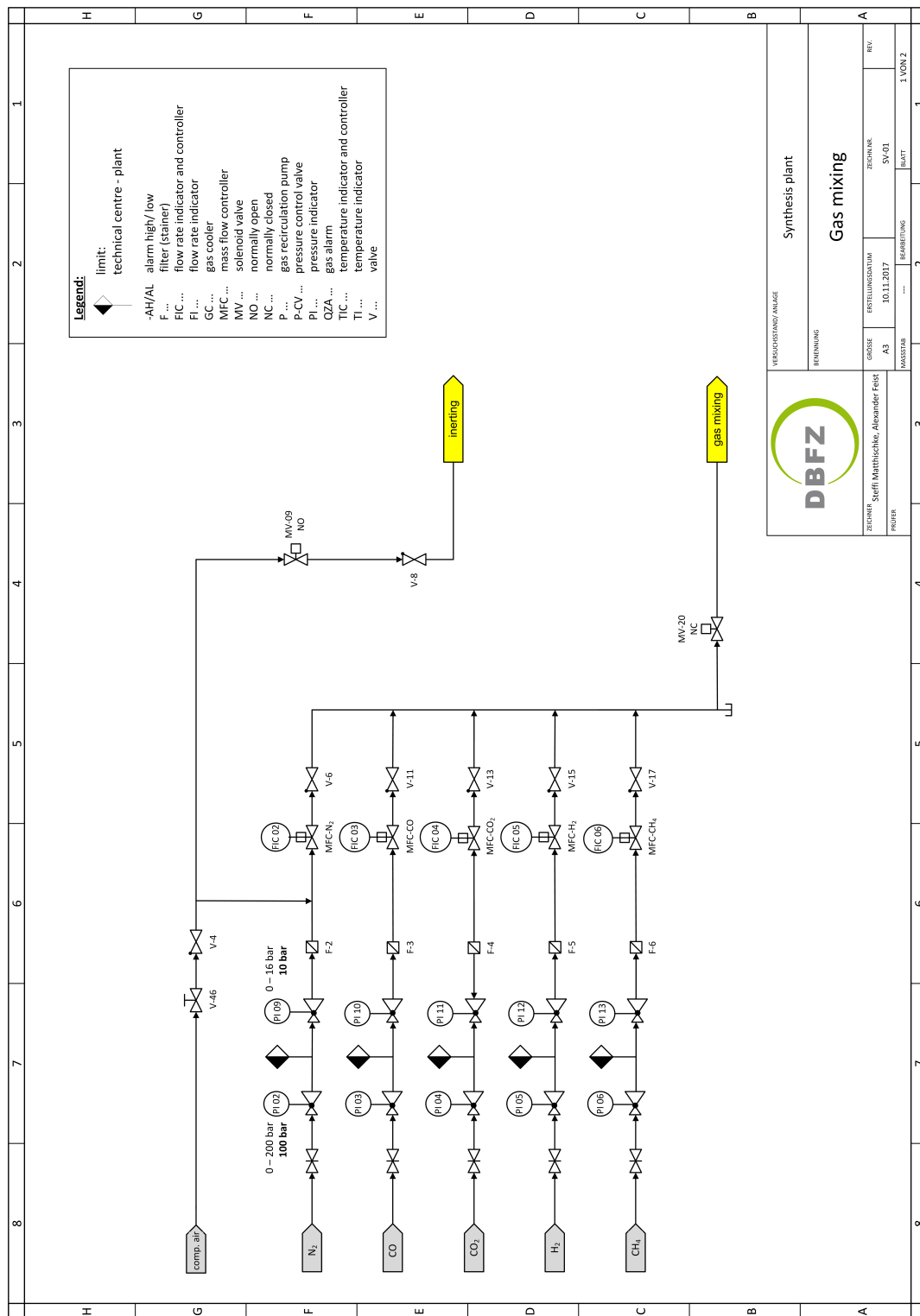


Figure C.2: Piping and instrumentation diagram of the lab-scale test facility – gas supply.

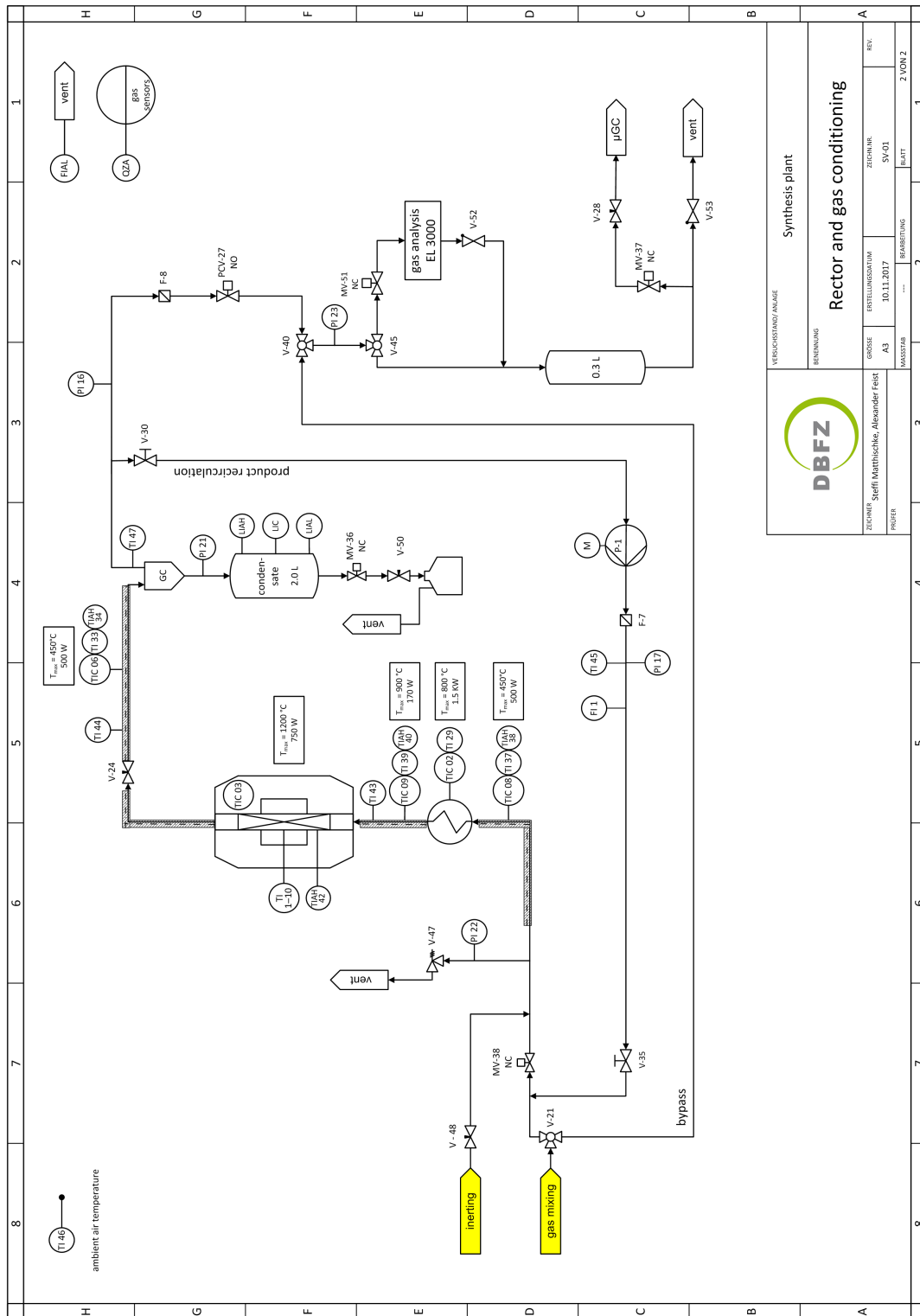


Figure C.3: Piping and instrumentation diagram of the lab-scale test facility – reactor section.

C.2 Catalyst preparation

The 5 wt% Ni-catalyst was produced by Jens Friedland at Ulm University according to the following preparation procedure:

1. 37.6 g Nickel(II) nitrate hexahydrate (Merck, analysis quality, CAS: 13478-00-7) was mixed with fully deionised water (55.0 g) in a glass beaker. This solution was heated-up till the nitrate salt was completely dissolved.
2. 142.5 g of 0.8/160 sieved alumina spheres (Sasol, Spec: 610115/KA548) were put in a lid of a 500 mL screwed glass. The alumina spheres had a specific surface area of $166 \text{ m}^2 \text{ g}^{-1}$ and an average diameter of $820 \text{ }\mu\text{m}$.
3. The hot Ni solution of the first step was slowly added whilst stirring constantly with a glass rod until all components were completely mixed.
4. Afterwards, the mixture was shaken several times, hermetically sealed, and homogenised in a thermal-oil bath at $65 \text{ }^\circ\text{C}$ for 5 hours. The mixture was shaken again every 1.5 hours.
5. After 8 hours, the screwed glass was opened thereby allowing the water to evaporate overnight. Here, a slight demixing occurred via the condensation of water in the upper part of the glass, which was detected by lighter catalyst particles.
6. On the next day, the dewatered raw catalyst was calcined in an inert nitrogen atmosphere (500 L h^{-1}). Thereby, the temperature was increased by 1 K min^{-1} until $300 \text{ }^\circ\text{C}$ was reached, held constant over 16 hours, and reduced afterwards to $50 \text{ }^\circ\text{C}$.
7. At last, the catalyst was taken out of the oven and packaged.

C.3 Balance of the experimental results – theory of key components

During a chemical reaction in a closed system, the number of atoms for each element in the total reaction mixture stays constant. This can be described by the element balance (Eq. C.1), where β_{hi} are the coefficients of the element h in the molecular formula of the component i . The element balance is transferred to matrices (Eq. C.2) and the element-component-matrix \underline{B} is split to key components (index 1) and non-key components (index 2). The changes of the number of moles for the non-key components $\Delta\dot{n}_2$ can be then calculated according to Eq. C.3.

$$\sum_{i=1}^N \beta_{hi} \Delta\dot{n}_i = 0 \quad \text{with} \quad \Delta\dot{n}_i = \dot{n}_i - \dot{n}_{i,in} \quad (\text{C.1})$$

$$\underline{B} \Delta\dot{n} = 0 = (\underline{B}_1 \quad \underline{B}_2) \begin{pmatrix} \Delta\dot{n}_1 \\ \Delta\dot{n}_2 \end{pmatrix} \quad (\text{C.2})$$

$$\Delta\dot{n}_2 = -\underline{B}_2^{-1} \underline{B}_1 \Delta\dot{n}_1 \quad (\text{C.3})$$

Before the theory of key components is applied for the methanation experiments, it is assumed that no carbon deposits and no adsorbed species accumulate on the catalyst surface, and that no side-reactions occur. The resulting element-component-matrix is then:

$$\underline{B} = \begin{matrix} & \begin{matrix} H_2 & CO & CO_2 & CH_4 & H_2O \end{matrix} \\ \begin{matrix} C \\ H \\ O \end{matrix} & \begin{pmatrix} 0 & 1 & 1 & 1 & 0 \\ 2 & 0 & 0 & 4 & 2 \\ 0 & 1 & 2 & 0 & 1 \end{pmatrix} \end{matrix} \quad (\text{C.4})$$

The rank of the element-component-matrix determines the number of the non-key components. In the case of methanation, the rank of \underline{B} is three – meaning that two key components have to be selected. Similarly, Kangas et al. (2017) have derived that two independent reactions within the methanation are presented. For the selection of key and non-key components, it is recommended that the conversion of a key component should be comparably high and that the non-key components should contain at least $rank(\underline{B})$ different elements. Therefore, H_2 and CO_2 are selected as key components leading to the following system of equations according to Eq. C.3.

$$\begin{bmatrix} \Delta \dot{n}_{CO} \\ \Delta \dot{n}_{CH_4} \\ \Delta \dot{n}_{H_2O} \end{bmatrix} = - \underbrace{\begin{bmatrix} 2/3 & -1/6 & 1/3 \\ 1/3 & 1/6 & -1/3 \\ -2/3 & 1/6 & 2/3 \end{bmatrix}}_{\underline{B}_2^{-1}} \underbrace{\begin{bmatrix} 0 & 1 \\ 2 & 0 \\ 0 & 2 \end{bmatrix}}_{\underline{B}_1} \begin{bmatrix} \Delta \dot{n}_{H_2} \\ \Delta \dot{n}_{CO_2} \end{bmatrix} \quad (C.5)$$

$$\begin{bmatrix} \Delta \dot{n}_{CO} \\ \Delta \dot{n}_{CH_4} \\ \Delta \dot{n}_{H_2O} \end{bmatrix} = \underbrace{\begin{bmatrix} 1/3 & -4/3 \\ -1/3 & 1/3 \\ -1/3 & -2/3 \end{bmatrix}}_{\underline{B}^*} \begin{bmatrix} \Delta \dot{n}_{H_2} \\ \Delta \dot{n}_{CO_2} \end{bmatrix} \quad (C.6)$$

Before the system of equations (Eq. C.6) is converted to molar fractions, volume-reduction factors are defined (Eqs. C.7–C.8). Thereby, $\dot{n}_{out,wet}$ is the molar flow rate directly after the reactor outlet, and $\dot{n}_{out,dry}$ is the molar flow rate of the product gas downstream the condensation trap. The molar flow rates of carbon monoxide, methane, and water at the systems inlet are zero, meaning that no product component is supplied. Moreover, it is assumed that the total amount of water can be separated in the condensation trap.

$$VF' = \frac{\dot{n}_{out,wet}}{\dot{n}_{in}} \quad (C.7)$$

$$VF = \frac{\dot{n}_{out,dry}}{\dot{n}_{in}} \quad (C.8)$$

$$\begin{bmatrix} y_{CO,out,wet} \\ y_{CH_4,out,wet} \\ y_{H_2O,out,wet} \end{bmatrix} = \underline{B}^* \begin{bmatrix} y_{H_2,out,wet} - y_{H_2,in} \frac{1}{VF'} \\ y_{CO_2,out,wet} - y_{CO_2,in} \frac{1}{VF'} \end{bmatrix} \quad (C.9)$$

$$\begin{bmatrix} y_{CO,out,dry} \\ y_{CH_4,out,dry} \\ \frac{y_{H_2O,out,wet}}{(1-y_{H_2O,out,wet})} \end{bmatrix} = \underline{B}^* \begin{bmatrix} y_{H_2,out,dry} - y_{H_2,in} \frac{1}{VF} \\ y_{CO_2,out,dry} - y_{CO_2,in} \frac{1}{VF} \end{bmatrix} \quad (C.10)$$

If the first two lines of the resulting system of equations (Eq. C.10) are added up, the volume-reduction factor VF can be calculated by Eq. C.11.

$$VF = \frac{y_{CO_2,in}}{y_{CH_4,out,dry} + y_{CO,out,dry} + y_{CO_2,out,dry}} \quad (C.11)$$

Nomenclature

Latin symbols

| | | |
|-----------------|--|--|
| A | $[\text{m}^2]$ | area |
| A_{BET} | $[\text{m}^2 \text{g}^{-1}]$ | BET surface (= Brunauer–Emmett–Teller) |
| a and b | $[-]$ | parameters of Ergun's equation |
| $A - E$ | [diff.] | polynomial coefficients |
| Ar | $[-]$ | Arrhenius number |
| a_v | $[\text{m}^2 \text{m}^{-3}]$ | volume specific area |
| \underline{B} | $[-]$ | element-component-matrix |
| c | $[\text{mol m}^{-3}]$ | concentration |
| c | $[\text{m s}^{-1}]$ | speed of sound |
| CF | $[-]$ | correction factor |
| c_p | $[\text{J kg}^{-1} \text{K}^{-1}]$ | isobaric heat capacity |
| c_v | $[\text{J kg}^{-1} \text{K}^{-1}]$ | isochoric heat capacity |
| D | $[\text{m}^2 \text{s}^{-1}]$ | diffusion coefficient |
| d | $[\text{m}]$ | diameter |
| Da | $[-]$ | Damköhler number (index = order) |
| D_e | $[\text{m}^2 \text{s}^{-1}]$ | dispersion coefficient of mass |
| E_A | $[\text{J mol}^{-1}]$ | activation energy |
| f | $[-]$ | friction factor |
| $F_{i_1 i_2}$ | $[-]$ | mixture factor |
| f_ν | $[-]$ | viscous friction factor |
| h | $[\text{W m}^{-2} \text{K}^{-1}]$ | heat transfer coefficient |
| k | $[\text{m s}^{-1}]$ | mass transfer coefficient |
| $K_{eq,j}$ | [diff.] | equilibrium constant |
| K_i | $[\text{bar}^{-0.5}]$ | adsorption constant |
| k_j | $[\text{mol bar}^{-1} \text{kg}_{cat}^{-1} \text{s}^{-1}]$ | reaction rate constant |
| L | $[\text{m}]$ | length of the reactor |
| M | $[\text{kg mol}^{-1}]$ | molar mass |
| m | $[-]$ | number of axial discretization points |
| m | $[\text{kg}]$ | mass |
| Ma | $[-]$ | Mach number |
| n | $[-]$ | reaction order |

Greek symbols

| | | |
|---------------|--|---|
| \dot{n} | [mol s ⁻¹] | molar flow rate |
| Nu | [-] | Nusselt number |
| p | [Pa] | pressure |
| p_i | [Pa] | partial pressure |
| Pe | [-] | Peclet number |
| Pr | [-] | Prandtl number |
| R | [J mol ⁻¹ K ⁻¹] | universal gas constant ($R = 8.3145$ J mol ⁻¹ K ⁻¹) |
| \tilde{R} | [J kg ⁻¹ K ⁻¹] | specific gas constant |
| r | [m] | radial coordinate |
| Re | [-] | Reynolds number |
| Rec | [-] | recycle ratio |
| r_j | [mol s ⁻¹ kg _{cat} ⁻¹] | rate of the reaction j |
| s | [m] | thickness of the reactor wall |
| Se | [-] | Semenov number |
| T | [°C or K] | temperature |
| t | [s] | time |
| \bar{t} | [s] | residence time |
| t_d | [s] | dead time |
| t_{norm} | [-] | normalized time |
| u | [m s ⁻¹] | velocity |
| U_{comp} | [V] | pump voltage |
| V | [m ³] | volume |
| \dot{V} | [m ³ s ⁻¹ (STP)] | volumetric flow rate |
| VF | [-] | volume-reduction factor |
| $v_{\dot{V}}$ | [m ³ s ⁻²] | load change velocity of the volumetric flow rate |
| X | [-] | conversion |
| Y | [-] | yield |
| y_i | [vol%] | volume fraction |
| z | [m] | axial coordinate [0, L] |

Greek symbols

| | | |
|------------------|-------------------------------------|---|
| β_{hi} | [-] | coefficients of the element h in the molecular formula of the component i |
| Δ | [-] | difference |
| ΔH_{Ads} | [J mol ⁻¹] | adsorption enthalpy |
| ΔH_R | [J mol ⁻¹] | reaction enthalpy, reference value for $T = 298$ K |
| Δv_i | [m ³ mol ⁻¹] | diffusion volume |
| ε | [-] | porosity (volume ratio) |
| η | [Pa s] | dynamic viscosity |
| η | [-] | activity or effectiveness factor |

| | | |
|-------------|--------------------------------------|---|
| κ | [-] | isentropic exponent (heat capacity ratio) |
| λ | [W m ⁻¹ K ⁻¹] | thermal conduction coefficient |
| λ_e | [W m ⁻¹ K ⁻¹] | dispersion coefficient of heat |
| ν_i | [-] | stoichiometric coefficient |
| ξ | [m] | direction coordinate in the catalyst pellet |
| ρ | [kg m ⁻³] | density |
| τ | [-] | tortuosity |
| ϕ | [-] | Thiele modulus |
| φ | [diff.] | balance variable |

Subscripts

| | |
|-------------|--|
| 0 | reference conditions |
| <i>a</i> | ambient |
| <i>act</i> | actual |
| <i>ad</i> | adiabatic |
| <i>Ads</i> | adsorption |
| <i>ax</i> | axial |
| <i>bed</i> | fixed-bed |
| <i>c</i> | catalyst |
| <i>comp</i> | recycle compressor |
| <i>cool</i> | coolant |
| <i>det</i> | detected |
| <i>dil</i> | dilution |
| <i>dry</i> | dry |
| <i>ed</i> | educt |
| <i>eff</i> | efficient |
| <i>end</i> | value at the end of the unsteady ramp ($t = t_{ramp}$) |
| <i>eq</i> | equilibrium |
| <i>g</i> | gas phase |
| <i>heat</i> | heat |
| <i>i</i> | chemical components ($i = \text{H}_2, \text{CO}_2, \text{CO}, \text{CH}_4, \text{H}_2\text{O}, \text{N}_2$), [1, <i>N</i>] |
| <i>in</i> | inlet stream |
| <i>int</i> | internal |
| <i>j</i> | reactions, $j = \text{CO}_2$ methanation (CO ₂ -Meth. = 1), CO methanation (CO-Meth. = 2), reverse water-gas shift (rWGS = 3) |
| <i>Kn</i> | Knudsen |
| <i>lam</i> | laminar |
| <i>m</i> | molecular |
| <i>mass</i> | mass based |
| <i>max</i> | maximum |

Abbreviations

| | |
|--------------|---|
| <i>mix</i> | mixed stream |
| <i>MR</i> | methanation reactor |
| <i>nom</i> | nominal |
| <i>norm</i> | normalized |
| <i>out</i> | outlet stream |
| <i>p</i> | pore |
| <i>r</i> | reactor |
| <i>rad</i> | radial |
| <i>ramp</i> | ramp |
| <i>rct</i> | reaction |
| <i>rec</i> | recycle |
| <i>ref</i> | reference |
| <i>s</i> | superficial |
| <i>start</i> | value at the start of the unsteady ramp ($t = 0$ min) |
| <i>sur</i> | surface |
| <i>th</i> | thermal |
| <i>total</i> | total |
| <i>turb</i> | turbulent |
| <i>v</i> | volume specific |
| <i>void</i> | void |
| <i>w</i> | reactor wall (<i>wi</i> – wall inside, <i>wa</i> – wall outside) |
| <i>wet</i> | wet |

Abbreviations

| | |
|--------|---|
| AEL | alkaline electrolysis |
| CFD | computational fluid dynamics |
| DAC | direct air capture |
| DIFI | differential flow instability |
| FBR | fixed-bed reactor |
| FBRR | fixed-bed recycle reactor |
| GHSV | gas hourly space velocity |
| LCOE | levelised cost of electricity |
| MOL | method of lines |
| MPC | model-predictive control |
| PDE | partial differential equation |
| PEM-EL | polymer electrolyte membrane electrolysis |
| PHES | pumped hydroelectric energy storage |
| PtG | power-to-gas |
| PtX | power-to-X |

| | |
|------|-------------------------------|
| RDS | rate-determining step |
| RES | renewable energy sources |
| SMR | steam methane reforming |
| SNG | synthetic natural gas |
| TRL | technology readiness level |
| VSVO | variable-step, variable-order |
| WGS | water-gas shift |

Bibliography

- Abrol, S. and C. M. Hilton (2012). Modeling, simulation and advanced control of methanol production from variable synthesis gas feed. *Computers & Chemical Engineering* 40, pp. 117–131. DOI: 10.1016/j.compchemeng.2012.02.005.
- Adler, R. (2000a). Stand der Simulation von heterogen-gaskatalytischen Reaktionsabläufen in Festbettrohrreaktoren – Teil 1. *Chemie Ingenieur Technik* 72(6), pp. 555–564. DOI: 10.1002/1522-2640(200006)72:6<555::AID-CITE555>3.0.CO;2-#.
- Adler, R. (2000b). Stand der Simulation von heterogen-gaskatalytischen Reaktionsabläufen in Festbettrohrreaktoren – Teil 2. *Chemie Ingenieur Technik* 72(7), pp. 688–699. DOI: 10.1002/1522-2640(200007)72:7<688::AID-CITE688>3.0.CO;2-4.
- Agricola, A.-C. and A. Moser (2012). Integration der erneuerbaren Energien in den deutsch-europäischen Strommarkt (kurz: Integration EE). Final report. Deutsche Energie-Agentur GmbH.
- Aicher, T., M. Iglesias González and M. Götz (2014). Betrachtungen des Gesamtsystems im Hinblick auf Dynamik und Prozessintegration. *Energie/ Wasser-Praxis* 65(11), pp. 51–55.
- Aldana, P. A. U., F. Ocampo, K. Kobl, B. Louis, F. Thibault-Starzyk, M. Daturi, P. Bazin, S. Thomas and A. C. Roger (2013). Catalytic CO₂ valorization into CH₄ on Ni-based ceria-zirconia. Reaction mechanism by operando IR spectroscopy. *Catalysis Today* 215, pp. 201–207. DOI: 10.1016/j.cattod.2013.02.019.
- Anderson, J. B. (1963). A criterion for isothermal behaviour of a catalyst pellet. *Chemical Engineering Science* 18(2), pp. 147–148.
- Andrigo, P., R. Bagatin and G. Pagani (1999). Fixed bed reactors. *Catalysis Today* 52(2–3), pp. 197–221. DOI: 10.1016/S0920-5861(99)00076-0.
- Aparicio, L. M. (1997). Transient isotopic studies and microkinetic modeling of methane reforming over nickel catalysts. *Journal of Catalysis* 165(2), pp. 262–274. DOI: 10.1006/jcat.1997.1468.
- Araki, M. and V. Ponc (1976). Methanation of carbon monoxide on nickel and nickel-copper alloys. *Journal of Catalysis* 44(3), pp. 439–448. DOI: 10.1016/0021-9517(76)90421-8.

- Ausfelder, F., C. Beilmann, M. Bertau, S. Bräuninger, A. Heinzl, R. Hoer, W. Koch, F. Mahlendorf, A. Metzeltin, M. Peuckert, L. Plass, K. Räuchle, M. Reuter, G. Schaub, S. Schiebahn, E. Schwab, F. Schüth, D. Stolten, G. Teßmer, K. Wagemann and K.-F. Ziegahn (2017). Energy storage as part of a secure energy supply. *ChemBioEng Reviews* 4(3), pp. 144–210. DOI: 10.1002/cben.201700004.
- Baerns, M., A. Behr, A. Brehm, J. Gmehling, H. Hofmann, U. Onken and A. Renken (2006). Technische Chemie. Wiley-VCH.
- Bailera, M., S. Espatolero, P. Lisbona and L. M. Romeo (2017a). Power to gas-electrochemical industry hybrid systems: A case study. *Applied Energy* 202, pp. 435–446. DOI: 10.1016/j.apenergy.2017.05.177.
- Bailera, M., P. Lisbona, L. M. Romeo and S. Espatolero (2017b). Power to gas projects review: Lab, pilot and demo plants for storing renewable energy and CO₂. *Renewable and Sustainable Energy Reviews* 69, pp. 292–312. DOI: 10.1016/j.rser.2016.11.130.
- Bajohr, S., M. Götz, F. Graf and F. Ortloff (2011). Speicherung von regenerativ erzeugter elektrischer Energie in der Erdgasinfrastruktur. *gwf-Gas/ Erdgas* 152(4), pp. 200–210.
- Baraj, E., S. Vagaský, T. Hlinčík, K. Ciahotný and V. Tekáč (2016). Reaction mechanisms of carbon dioxide methanation. *Chemical Papers* 70(4), pp. 395–403. DOI: 10.1515/chempap-2015-0216.
- Beck, H.-P., B. Engel, L. Hofmann, R. Menges, T. Turek and H. Weyer (2013). Eignung von Speichertechnologien zum Erhalt der Systemsicherheit. Final report. Energie-Forschungszentrum Niedersachsen.
- Belderbos, A., E. Delarue and W. D'haeseleer (2015). Possible role of power-to-gas in future energy systems. *12th International Conference on the European Energy Market (EEM)*. DOI: 10.1109/EEM.2015.7216744.
- Belimov, M., D. Metzger and P. Pfeifer (2017). On the temperature control in a microstructured packed bed reactor for methanation of CO/CO₂ mixtures. *AIChE Journal* 63(1), pp. 120–129. DOI: 10.1002/aic.15461.
- Bengaouer, A., J. Ducamp, I. Champon and R. Try (2018). Performance evaluation of fixed-bed, millistructured, and metallic foam reactor channels for CO₂ methanation. *The Canadian Journal of Chemical Engineering* 96(9), pp. 1937–1945. DOI: 10.1002/cjce.23140.
- Bertau, M., H. Offermanns, L. Plass, F. Schmidt and H.-J. Wernicke (2014). Methanol: The Basic Chemical and Energy Feedstock of the Future – Asinger's Vision Today. Springer-Verlag. DOI: 10.1007/978-3-642-39709-7.

-
- Biegger, P., F. Kirchbacher, A. R. Medved, M. Miltner, M. Lehner and M. Harasek (2018). Development of honeycomb methanation catalyst and its application in power to gas systems. *Energies* 11(7), pp. 1–17. DOI: 10.3390/en11071679.
- Boer, H. S. de, L. Grond, H. Moll and R. Benders (2014). The application of power-to-gas, pumped hydro storage and compressed air energy storage in an electricity system at different wind power penetration levels. *Energy* 72, pp. 360–370. DOI: 10.1016/j.energy.2014.05.047.
- Boreskov, G. K. and Y. S. Matros (1983). Unsteady-state performance of heterogeneous catalytic reactions. *Catalysis Reviews* 25(4), pp. 551–590. DOI: 10.1080/01614948308078056.
- Bremer, J., K. H. G. Rätze and K. Sundmacher (2017). CO₂ methanation: Optimal start-up control of a fixed-bed reactor for power-to-gas applications. *AIChE Journal* 63(1), pp. 23–31. DOI: 10.1002/aic.15496.
- Bundesministerium für Wirtschaft und Technologie (BMWi) (2010). Energiekonzept für eine umweltschonende, zuverlässige und bezahlbare Energieversorgung.
- Bunimovich, G. A., P. L. Silverston and Y. S. Matros (2008). Unsteady-state reactor operation. *Handbook of Heterogeneous Catalysis*. Ed. by G. Ertl, H. Knözinger, F. Schüth and J. Weitkamp. 2nd edition. Wiley-VCH Verlag GmbH & Co. KGaA. Chap. 10.4, pp. 2156–2174. DOI: 10.1002/9783527610044.hetcat0114.
- Buttler, A. and H. Spliethoff (2018). Current status of water electrolysis for energy storage, grid balancing and sector coupling via power-to-gas and power-to-liquids: A review. *Renewable and Sustainable Energy Reviews* 82, pp. 2440–2454. DOI: 10.1016/j.rser.2017.09.003.
- Chu, C. F. and K. M. Ng (1989). Flow in packed tubes with a small tube to particle diameter ratio. *AIChE Journal* 35(1), pp. 148–158. DOI: 10.1002/aic.690350116.
- Dissinger, G. R., S. H. Johnson and F. P. Stein (1980). Dynamic simulation of methanation reactors, interstage heat exchangers, and controllers. *Chemical Engineering Communications* 4(4–5), pp. 577–591. DOI: 10.1080/00986448008935933.
- Doesburg, H. V. and W. A. D. Jong (1976a). Transient behaviour of an adiabatic fixed-bed methanator – I: experiments with binary feeds of CO or CO₂ in hydrogen. *Chemical Engineering Science* 31(1), pp. 45–51. DOI: 10.1016/0009-2509(76)85007-5.
- Doesburg, H. V. and W. A. D. Jong (1976b). Transient behaviour of an adiabatic fixed-bed methanator – II: methanation of mixtures of carbon monoxide and carbon dioxide. *Chemical Engineering Science* 31(1), pp. 53–58. DOI: 10.1016/0009-2509(76)85008-7.

- Duduković, M. P., F. Larachi and P. L. Mills (2002). Multiphase catalytic reactors: a perspective on current knowledge and future trends. *Catalysis Reviews* 44(1), pp. 123–246. DOI: 10.1081/CR-120001460.
- Effenberger, H. (2000). Dampferzeugung. Springer-Verlag.
- Eigenberger, G., G. Kolios and U. Nieken (2007). Thermal pattern formation and process intensification in chemical reaction engineering. *Chemical Engineering Science* 62(18). 19th International Symposium on Chemical Reaction Engineering – From Science to Innovative Engineering, pp. 4825–4841. DOI: 10.1016/j.ces.2007.02.039.
- Eigenberger, G. and W. Ruppel (2012). Catalytic fixed-bed reactors. *Ullmann's Encyclopedia of Industrial Chemistry*. 7th edition. Vol. 15. Wiley-VCH Verlag GmbH & Co. KGaA, pp. 1–66. DOI: 10.1002/14356007.b04_199.pub2.
- Emig, G. (1986). Reaktormodelle für heterogen katalysierte Gasphasenreaktionen. *Berichte der Bunsengesellschaft für physikalische Chemie* 90(11), pp. 968–976. DOI: 10.1002/bbpc.19860901109.
- Engelbrecht, N., S. Chiuta, R. C. Everson, H. W. J. P. Neomagus and D. G. Bessarabov (2017). Experimentation and CFD modelling of a microchannel reactor for carbon dioxide methanation. *Chemical Engineering Journal* 313, pp. 847–857. DOI: 10.1016/j.cej.2016.10.131.
- Ergun, S. (1952). Fluid flow through packed columns. *Chemical Engineering Progress* 48, pp. 89–94.
- Ess, F., L. Haefke, J. Hobohm, F. Peter and M. Wünsch (2012). The significance of international hydropower storage for the energy transition. Report. Prognos AG.
- EUROKIN (2011). EUROKIN spreadsheet on requirements for measurement of intrinsic kinetics in the gas-solid fixed-bed reactor. Web address: http://eurokin.org/?page_id=571 (last access: 06.02.2018).
- European Commission (2014a). A policy framework for climate and energy in the period from 2020 to 2030. Communication from the commission to the European parliament, the council, the European economic and social committee and the committee of the regions. COM(2014) 15.
- European Commission (2014b). Energy Roadmap 2050. Booklet. COM(2011) 885.
- Frank, E., J. Gorre, F. Ruoss and M. J. Friedl (2018). Calculation and analysis of efficiencies and annual performances of power-to-gas systems. *Applied Energy* 218, pp. 217–231. DOI: 10.1016/j.apenergy.2018.02.105.

-
- Frey, M., T. Romero, A.-C. Roger and D. Edouard (2016). Open cell foam catalysts for CO₂ methanation: Presentation of coating procedures and in situ exothermicity reaction study by infrared thermography. *Catalysis Today* 273. 5th International Conference on Structured Catalysts and Reactors (ICOSCAR-5), pp. 83–90. DOI: 10.1016/j.cattod.2016.03.016.
- Friedland, J., T. Turek and R. Güttel (2016). Investigations on the low temperature methanation with pulse reaction of CO. *Chemie Ingenieur Technik* 88(11), pp. 1833–1838. DOI: 10.1002/cite.201600056.
- Friedland, J., T. Turek and R. Güttel (2017). Experimental investigations on the pulsed CO methanation. *Annual Meeting on Reaction Engineering*. Presentation.
- Froment, G. F. (1974). Fixed bed catalytic reactors. Technological and fundamental design aspects. *Chemie Ingenieur Technik* 46(9), pp. 374–386. DOI: 10.1002/cite.330460903.
- Frontera, P., A. Macario, M. Ferraro and P. Antonucci (2017). Supported catalysts for CO₂ methanation: A review. *Catalysts* 7(2). DOI: 10.3390/catal7020059.
- Gahleitner, G. (2013). Hydrogen from renewable electricity: An international review of power-to-gas pilot plants for stationary applications. *International Journal of Hydrogen Energy* 38(5), pp. 2039–2061. DOI: 10.1016/j.ijhydene.2012.12.010.
- Gao, J., Q. Liu, F. Gu, B. Liu, Z. Zhong and F. Su (2015). Recent advances in methanation catalysts for the production of synthetic natural gas. *RSC Advances* 5(29), pp. 22759–22776. DOI: 10.1039/C4RA16114A.
- Gao, J., Y. Wang, Y. Ping, D. Hu, G. Xu, F. Gu and F. Su (2012). A thermodynamic analysis of methanation reactions of carbon oxides for the production of synthetic natural gas. *RSC Advances* 2(6), pp. 2358–2368. DOI: 10.1039/C2RA00632D.
- Ghaib, K. (2016). Numerische Simulationen der katalytischen Methanisierung von CO₂ in einem pseudo-homogenen Strömungsrohr. *Chemie Ingenieur Technik* 88(8), pp. 1102–1108. DOI: 10.1002/cite.201500180.
- Ghaib, K. and F.-Z. Ben-Fares (2018). Power-to-methane: A state-of-the-art review. *Renewable and Sustainable Energy Reviews* 81(Part 1), pp. 433–446. DOI: 10.1016/j.rser.2017.08.004.
- Ghaib, K., K. Nitz and F.-Z. Ben-Fares (2016). Chemical methanation of CO₂: A review. *ChemBioEng Reviews* 3(6), pp. 266–275. DOI: 10.1002/cben.201600022.
- Gilles, E. D. (1968). Das dynamische Verhalten chemischer Reaktoren. Eine Übersicht. *Chemie Ingenieur Technik* 40(9–10), pp. 469–477. DOI: 10.1002/cite.330400911.

- Gilles, E. D. (1977). Dynamisches Verhalten von Festbettreaktoren. *Chemie Ingenieur Technik* 49(2), pp. 142–149. DOI: 10.1002/cite.330490211.
- Götz, M., S. Bajohr, F. Graf, R. Reimert and T. Kolb (2013). Application of a slurry bubble column reactor for the production of substitute natural gas. *Chemie Ingenieur Technik* 85(7), pp. 1146–1151. DOI: 10.1002/cite.201200212.
- Götz, M., J. Lefebvre, F. Mörs, A. M. Koch, F. Graf, S. Bajohr, R. Reimert and T. Kolb (2016). Renewable power-to-gas: A technological and economic review. *Renewable Energy* 85, pp. 1371–1390. DOI: 10.1016/j.renene.2015.07.066.
- Graf, F., M. Götz, M. Henel, T. Schaaf and R. Tichler (2014). Technoökonomische Studie von Power-to-Gas-Konzepten. Final report. DVGW Deutscher Verein des Gas- und Wasserfaches e.V.
- Gruber, M., C. Wieland, P. Habisreuther, D. Trimis, D. Schollenberger, S. Bajohr, O. von Morstein and S. Schirrmeister (2018). Modeling and design of a catalytic wall reactor for the methanation of carbon dioxide. *Chemie Ingenieur Technik* 90(5), pp. 615–624. DOI: 10.1002/cite.201700160.
- Güttel, R. (2013). Study of unsteady-state operation of methanation by modeling and simulation. *Chemical Engineering & Technology* 36(10), pp. 1675–1682. DOI: 10.1002/ceat.201300223.
- Hack, N., S. Unz, C. Pieper and M. Beckmann (2013). Stand der Technik und innovative Verfahrenskonzepte zur Umwandlung und Speicherung elektrischer Energie. *Kraftwerkstechnik – Sichere und nachhaltige Energieversorgung*. Ed. by M. Beckmann and A. Hurtado. Vol. 5. TK Verlag Karl Thomé-Kozmiensky, pp. 822–857.
- Handley, D. and P. J. Heggs (1968). Momentum and heat transfer mechanisms in regular shaped packings. *Transactions of the Institution of Chemical Engineers* 46(9), pp. 251–254.
- Harms, H., B. Höhle and A. Skov (1980). Methanisierung kohlenmonoxidreicher Gase beim Energie-Transport. *Chemie Ingenieur Technik* 52(6), pp. 504–515. DOI: 10.1002/cite.330520605.
- Hashimoto, K., M. Yamasaki, K. Fujimura, T. Matsui, K. Izumiya, M. Komori, A. A. El-Moneim, E. Akiyama, H. Habazaki, N. Kumagai, A. Kawashima and K. Asami (1999). Global CO₂ recycling – novel materials and prospect for prevention of global warming and abundant energy supply. *Materials Science and Engineering: A* 267(2), pp. 200–206. DOI: [https://doi.org/10.1016/S0921-5093\(99\)00092-1](https://doi.org/10.1016/S0921-5093(99)00092-1).

-
- Hicks, R. E. (1970). Pressure drop in packed beds of spheres. *Industrial & Engineering Chemistry Fundamentals* 9(3), pp. 500–502. DOI: 10.1021/i160035a032.
- Hiller, H., R. Reimert, F. Marschner, H.-J. Renner, W. Boll, E. Supp, M. Brejc, W. Liebner, G. Schaub, G. Hochgesand et al. (2006). Gas production. *Ullmann's Encyclopedia of Industrial Chemistry*. Wiley-VCH Verlag GmbH & Co. KGaA, pp. 1–169. DOI: 10.1002/14356007.a12_169.pub2.
- Iaquaniello, G., S. Setini, A. Salladini and M. D. Falco (2018). CO₂ valorization through direct methanation of flue gas and renewable hydrogen: A technical and economic assessment. *International Journal of Hydrogen Energy* 43(36), pp. 17069–17081. DOI: 10.1016/j.ijhydene.2018.07.099.
- Iglesias González, M., H. Eilers and G. Schaub (2016a). Flexible operation of fixed-bed reactors for a catalytic fuel synthesis – CO₂ hydrogenation as example reaction. *Energy Technology* 4(1), pp. 90–103. DOI: 10.1002/ente.201500259.
- Iglesias González, M. and G. Schaub (2016b). Gaseous hydrocarbon syngases from renewable electricity via H₂/CO₂-flexibility of fixed-bed catalytic reactors. *International Journal of Chemical Reactor Engineering* 14(5), pp. 1089–1099. DOI: 10.1515/ijcre-2014-0135.
- Il'in, A. and D. Luss (1992). Wrong-way behavior of packed-bed reactors: influence of reactant adsorption on support. *AIChE Journal* 38(10), pp. 1609–1617. DOI: 10.1002/aic.690381011.
- Iordanidi, A. (2002). ‘Mathematical modeling of catalytic fixed bed reactors’. PhD thesis. University of Twente.
- Jakobsen, H. A. (2014). *Chemical Reactor Modelling*. 2nd edition. Springer. DOI: 10.1007/978-3-540-68622-4_11.
- Johnson, R. W. (1998). *Handbook of Fluid Dynamics*. Handbook Series for Mechanical Engineering. Taylor & Francis.
- Jones, W. E. and J. A. Wilson (1998). An introduction to process flexibility: Part 2. Recycle loop with reactor. *Chemical Engineering Education* 32, pp. 224–229.
- Jürgensen, L., E. A. Ehimen, J. Born and J. B. Holm-Nielsen (2015). Dynamic biogas upgrading based on the Sabatier process: Thermodynamic and dynamic process simulation. *Bioresource Technology* 178, pp. 323–329. DOI: 10.1016/j.biortech.2014.10.069.
- Kalz, K. F., R. Kraehnert, M. Dvoyashkin, R. Dittmeyer, R. Gläser, U. Krewer, K. Reuter and J.-D. Grunwaldt (2017). Future challenges in heterogeneous catalysis: understanding

- catalysts under dynamic reaction conditions. *ChemCatChem* 9(1), pp. 17–29. DOI: 10.1002/cctc.201600996.
- Kangas, P., F. V. Vázquez, J. Savolainen, R. Pajarre and P. Koukkari (2017). Thermodynamic modelling of the methanation process with affinity constraints. *Fuel* 197, pp. 217–225. DOI: 10.1016/j.fuel.2017.02.029.
- Katoufa, M., E. Giglio, D. Katsourinis, G. Vourliotakis, S. Bensaid, F. Deorsola, R. Pirone, G. Saracco and M. Founti (2015). CO₂ methanation under atmospheric pressure conditions on a Ni catalyst: Experiments and kinetic modeling. *5th European PEFC & H₂ Forum*, pp. 1–10.
- Kiewidt, L. (2017). ‘Solid sponges as support for heterogeneous catalysts in gas-phase reactions’. PhD thesis. University of Bremen.
- Kiewidt, L. and J. Thöming (2015). Predicting optimal temperature profiles in single-stage fixed-bed reactors for CO₂-methanation. *Chemical Engineering Science* 132, pp. 59–71. DOI: 10.1016/j.ces.2015.03.068.
- Klose, J. and M. Baerns (1984). Kinetics of the methanation of carbon monoxide on an alumina-supported nickel catalyst. *Journal of Catalysis* 85(1), pp. 105–116. DOI: 10.1016/0021-9517(84)90114-3.
- Klusáček, K. and V. Stuchlý (1995). Increasing of carbon monoxide methanation rate by forced feed composition cycling. *Catalysis Today* 25(2), pp. 169–174. DOI: 10.1016/0920-5861(95)00106-P.
- Kopyscinski, J. (2010). ‘Production of synthetic natural gas in a fluidized bed reactor’. PhD thesis. ETH Zurich.
- Kopyscinski, J., T. J. Schildhauer and S. M. A. Biollaz (2010). Production of synthetic natural gas (SNG) from coal and dry biomass – A technology review from 1950 to 2009. *Fuel* 89(8), pp. 1763–1783. DOI: 10.1016/j.fuel.2010.01.027.
- Koschany, F., D. Schlereth and O. Hinrichsen (2016). On the kinetics of the methanation of carbon dioxide on coprecipitated NiAl(O)_x. *Applied Catalysis B: Environmental* 181, pp. 504–516. DOI: 10.1016/j.apcatb.2015.07.026.
- Kötter, E., L. Schneider, F. Sehnke, K. Ohnmeiss and R. Schröer (2016). The future electric power system: Impact of power-to-gas by interacting with other renewable energy components. *Journal of Energy Storage* 5, pp. 113–119. DOI: 10.1016/j.est.2015.11.012.

-
- Koytsoumpa, E. I. and S. Karellas (2018). Equilibrium and kinetic aspects for catalytic methanation focusing on CO₂ derived Substitute Natural Gas (SNG). *Renewable and Sustainable Energy Reviews* 94, pp. 536–550. DOI: <https://doi.org/10.1016/j.rser.2018.06.051>.
- Kreitz, B., G. Wehinger and T. Turek (2018). Dynamic methanation of CO₂ – Effect of concentration forcing. *Annual Meeting on Reaction Engineering*. Presentation.
- Krishna, R. and J. M. van Baten (2012). Investigating the validity of the Bosanquet formula for estimation of diffusivities in mesopores. *Chemical Engineering Science* 69(1), pp. 684–688. DOI: [10.1016/j.ces.2011.11.026](https://doi.org/10.1016/j.ces.2011.11.026).
- Kulkarni, M. S. and M. P. Duduković (1996). Dynamics of gas phase and solid phase reactions in fixed bed reactors. *Chemical Engineering Science* 51(11), pp. 3083–3088. DOI: [10.1016/0009-2509\(96\)00201-1](https://doi.org/10.1016/0009-2509(96)00201-1).
- Kumar, S., R. A. Kumar, P. Munshi and A. Khanna (2012). Gas hold-up in three phase co-current bubble columns. *Procedia Engineering* 42. CHISA 2012, pp. 782–794. DOI: [10.1016/j.proeng.2012.07.470](https://doi.org/10.1016/j.proeng.2012.07.470).
- Kuznecova, I. and J. Gusca (2017). Property based ranking of CO and CO₂ methanation catalysts. *Energy Procedia* 128. International Scientific Conference ‘Environmental and Climate Technologies’ (CONNECT), pp. 255–260. DOI: [10.1016/j.egypro.2017.09.068](https://doi.org/10.1016/j.egypro.2017.09.068).
- Lazdans, A., E. Dace and J. Gusca (2016). Development of the experimental scheme for methanation process. *Energy Procedia* 95. International Scientific Conference ‘Environmental and Climate Technologies’ (CONNECT), pp. 540–545. DOI: [10.1016/j.egypro.2016.09.082](https://doi.org/10.1016/j.egypro.2016.09.082).
- Lee, J. P., V. Balakotaiah and D. Luss (1987). Thermoflow multiplicity in a packed-bed reactor Part I: Adiabatic case. *AIChE Journal* 33(7), pp. 1136–1154. DOI: [10.1002/aic.690330709](https://doi.org/10.1002/aic.690330709).
- Lefebvre, J., M. Götz, S. Bajohr, R. Reimert and T. Kolb (2015). Improvement of three-phase methanation reactor performance for steady-state and transient operation. *Fuel Processing Technology* 132, pp. 83–90. DOI: [10.1016/j.fuproc.2014.10.040](https://doi.org/10.1016/j.fuproc.2014.10.040).
- Lefebvre, J., N. Trudel, S. Bajohr and T. Kolb (2018). A study on three-phase CO₂ methanation reaction kinetics in a continuous stirred-tank slurry reactor. *Fuel* 217, pp. 151–159. DOI: [10.1016/j.fuel.2017.12.082](https://doi.org/10.1016/j.fuel.2017.12.082).
- Lehner, M., P. Biegger and A. R. Medved (2017). Power-to-Gas: Die Rolle der chemischen Speicherung in einem Energiesystem mit hohen Anteilen an erneuerbarer Energie. *e & i Elektrotechnik und Informationstechnik*, pp. 1–6. DOI: [10.1007/s00502-017-0502-6](https://doi.org/10.1007/s00502-017-0502-6).

- Lehner, M., R. Tichler, H. Steinmüller and M. Koppe (2014). Power-to-Gas: Technology and Business Models. Springer.
- Li, W., H. Wang, X. Jiang, J. Zhu, Z. Liu, X. Guo and C. Song (2018). A short review of recent advances in CO₂ hydrogenation to hydrocarbons over heterogeneous catalysts. *RSC Advances* 8(14), pp. 7651–7669. DOI: 10.1039/C7RA13546G.
- Li, X., B. Yang and Y. Zhang (2013). Dynamics and control study on the low temperature methanation reactor with mass and heat recycle. *Journal of Process Control* 23(10), pp. 1360–1370. DOI: 10.1016/j.jprocont.2013.09.003.
- Lim, J. Y., J. McGregor, A. J. Sederman and J. S. Dennis (2016). Kinetic studies of CO₂ methanation over a Ni/ γ -Al₂O₃ catalyst using a batch reactor. *Chemical Engineering Science* 141, pp. 28–45. DOI: 10.1016/j.ces.2015.10.026.
- Little, M., M. Thomson and D. Infield (2007). Electrical integration of renewable energy into stand-alone power supplies incorporating hydrogen storage. *International Journal of Hydrogen Energy* 32(10), pp. 1582–1588. DOI: 10.1016/j.ijhydene.2006.10.035.
- Lunde, P. J. (1974). Modeling, simulation, and operation of a Sabatier reactor. *Industrial & Engineering Chemistry Process Design and Development* 13(3), pp. 226–233. DOI: 10.1021/i260051a007.
- Luss, D. (1997). Temperature fronts and patterns in catalytic systems. *Industrial & Engineering Chemistry Research* 36(8), pp. 2931–2944. DOI: 10.1021/ie960597k.
- Marwood, M., R. Doepper, M. Prairie and A. Renken (1994a). Transient drift spectroscopy for the determination of the surface reaction kinetics of CO₂ methanation. *Chemical Engineering Science* 49(24), pp. 4801–4809. DOI: 10.1016/S0009-2509(05)80060-0.
- Marwood, M., R. Doepper and A. Renken (1996). Modeling of surface intermediates under forced periodic conditions applied to CO₂ methanation. *The Canadian Journal of Chemical Engineering* 74(5), pp. 660–663. DOI: 10.1002/cjce.5450740516.
- Marwood, M., R. Doepper and A. Renken (1997). In-situ surface and gas phase analysis for kinetic studies under transient conditions – The catalytic hydrogenation of CO₂. *Applied Catalysis A: General* 151(1), pp. 223–246. DOI: 10.1016/S0926-860X(96)00267-0.
- Marwood, M., F. V. Vyve, R. Doepper and A. Renken (1994b). Periodic operation applied to the kinetic study of CO₂ methanation. *Catalysis Today* 20(3), pp. 437–448. DOI: 10.1016/0920-5861(94)80137-1.

-
- Mears, D. E. (1971). Tests for transport limitations in experimental catalytic reactors. *Industrial & Engineering Chemistry Process Design and Development* 10(4), pp. 541–547. DOI: 10.1021/i260040a020.
- Mears, D. E. (1976). On criteria for axial dispersion in nonisothermal packed-bed catalytic reactors. *Industrial & Engineering Chemistry Fundamentals* 15(1), pp. 20–23. DOI: 10.1021/i160057a004.
- Mederos, F. S., I. Elizalde and J. Ancheyta (2009). Steady-state and dynamic reactor models for hydrotreatment of oil fractions: A review. *Catalysis Reviews* 51(4), pp. 485–607. DOI: 10.1080/01614940903048612.
- Menzinger, M., V. Yakhnin, A. Jaree, P. L. Silveston and R. R. Hudgins (2004). Dynamic responses of packed bed reactors. *Chemical Engineering Science* 59(19), pp. 4011–4022. DOI: 10.1016/j.ces.2004.05.031.
- Menzinger, M. and A. B. Rovinsky (1995). The differential flow instabilities. *Chemical Waves and Patterns*. Ed. by R. Kapral and K. Showalter. Springer. Chap. 11, pp. 365–397. DOI: 10.1007/978-94-011-1156-0_11.
- Meyer, D., J. Friedland, T. Kohn and R. Güttel (2017). Transfer functions for periodic reactor operation: Fundamental methodology for simple reaction networks. *Chemical Engineering & Technology* 40(11), pp. 2096–2103. DOI: 10.1002/ceat.201700122.
- Miao, B., S. S. K. Ma, X. Wang, H. Su and S. H. Chan (2016). Catalysis mechanisms of CO₂ and CO methanation. *Catalysis Science & Technology* 6(12), pp. 4048–4058. DOI: 10.1039/C6CY00478D.
- Milanzi, S., C. Spiller, B. Grosse, L. Hermann, J. Kochems and J. Müller-Kirchenbauer (2018). Technischer Stand und Flexibilität des Power-to-Gas-Verfahrens. Tech. rep. Department of Energy and Resources Management, TU Berlin.
- Mills, G. A. and F. W. Steffgen (1974). Catalytic methanation. *Catalysis Reviews* 8(1), pp. 159–210. DOI: 10.1080/01614947408071860.
- Molina, M. M., K. Christoph and J. Andreas (2016). Catalytic hydrogenation of carbon dioxide to methane in wall-cooled fixed-bed reactors[‡]. *Chemical Engineering & Technology* 39(12), pp. 2404–2415. DOI: 10.1002/ceat.201500614.
- Morbideilli, M. and A. Varma (1986). Parametric sensitivity and runaway in fixed-bed catalytic reactors. *Chemical Engineering Science* 41(4), pp. 1063–1071. DOI: 10.1016/0009-2509(86)87193-7.

- Müller, K., M. Fleige, F. Rachow and D. Schmeißer (2013). Sabatier based CO₂-methanation of flue gas emitted by conventional power plants. *Energy Procedia* 40, pp. 240–248. DOI: 10.1016/j.egypro.2013.08.028.
- Muroyama, H., Y. Tsuda, T. Asakoshi, H. Masitah, T. Okanishi, T. Matsui and K. Eguchi (2016). Carbon dioxide methanation over Ni catalysts supported on various metal oxides. *Journal of Catalysis* 343, pp. 178–184. DOI: 10.1016/j.jcat.2016.07.018.
- Mutz, B., H. W. P. Carvalho, W. Kleist and J.-D. Grunwaldt (2016). Dynamic transformation of small Ni particles during methanation of CO₂ under fluctuating reaction conditions monitored by operando X-ray absorption spectroscopy. *Journal of Physics: Conference Series* 712(1). 16th International Conference on X-ray Absorption Fine Structure (XAFS16), pp. 1–4. DOI: 10.1088/1742-6596/712/1/012050.
- Mutz, B., H. W. P. Carvalho, S. Mangold, W. Kleist and J.-D. Grunwaldt (2015). Methanation of CO₂: Structural response of a Ni-based catalyst under fluctuating reaction conditions unraveled by operando spectroscopy. *Journal of Catalysis* 327, pp. 48–53. DOI: 10.1016/j.jcat.2015.04.006.
- Mutz, B., A. M. Gänzler, M. Nachtegaal, O. Müller, R. Frahm, W. Kleist and J.-D. Grunwaldt (2017). Surface oxidation of supported Ni particles and its impact on the catalytic performance during dynamically operated methanation of CO₂. *Catalysts* 7(9), pp. 1–18. DOI: 10.3390/catal7090279.
- Mutz, B., P. Sprenger, W. Wang, D. Wang, W. Kleist and J.-D. Grunwaldt (2018). Operando Raman spectroscopy on CO₂ methanation over alumina-supported Ni, Ni₃Fe and NiRh_{0.1} catalysts: Role of carbon formation as possible deactivation pathway. *Applied Catalysis A: General* 556, pp. 160–171. DOI: 10.1016/j.apcata.2018.01.026.
- Neubert, M., A. Hauser, B. Pourhossein, M. Dillig and J. Karl (2018). Experimental evaluation of a heat pipe cooled structured reactor as part of a two-stage catalytic methanation process in power-to-gas applications. *Applied Energy* 229, pp. 289–298. DOI: 10.1016/j.apenergy.2018.08.002.
- Oliveira, E. L. G., C. A. Grande and A. E. Rodrigues (2010). Methane steam reforming in large pore catalyst. *Chemical Engineering Science* 65(5), pp. 1539–1550. DOI: 10.1016/j.ces.2009.10.018.
- Pan, Q., J. Peng, S. Wang and S. Wang (2014). In situ FTIR spectroscopic study of the CO₂ methanation mechanism on Ni/Ce_{0.5}Zr_{0.5}O₂. *Catalysis Science & Technology* 4(2), pp. 502–509. DOI: 10.1039/C3CY00868A.

-
- Park, J.-N. and E. W. McFarland (2009). A highly dispersed Pd-Mg/SiO₂ catalyst active for methanation of CO₂. *Journal of Catalysis* 266(1), pp. 92–97. DOI: 10.1016/j.jcat.2009.05.018.
- Parlikkad, N. R., S. Chambrey, P. Fongarland, N. Fatah, A. Khodakov, S. Capela and O. Guerrini (2013). Modeling of fixed bed methanation reactor for syngas production: Operating window and performance characteristics. *Fuel* 107, pp. 254–260. DOI: 10.1016/j.fuel.2013.01.024.
- Peebles, D. E., D. W. Goodman and J. M. White (1983). Methanation of carbon dioxide on nickel(100) and the effects of surface modifiers. *The Journal of Physical Chemistry* 87(22), pp. 4378–4387. DOI: 10.1021/j100245a014.
- Pregger, J. N. T., T. Naegler, D. Heide, D. L. de Tena, F. Trieb, Y. Scholz, K. Nienhaus, N. Gerhardt, M. Sterner, T. Trost, A. von Oehsen, R. Schwinn, C. Pape, H. Hahn, M. Wickert and B. Wenzel (2012). Langfristszenarien und Strategien für den Ausbau der erneuerbaren Energien in Deutschland bei Berücksichtigung der Entwicklung in Europa und global. Final report. German Aerospace Center (DLR).
- Puszyński, J., D. Šnita, V. Hlaváček and H. Hofmann (1981). A revision of multiplicity and parametric sensitivity concepts in nonisothermal nonadiabatic packed bed chemical reactors. *Chemical Engineering Science* 36(10), pp. 1605–1609. DOI: 10.1016/0009-2509(81)80004-8.
- Rachow, F. (2017). ‘Prozessoptimierung für die Methanisierung von CO₂ – vom Labor zum Technikum’. PhD thesis. Brandenburg University of Technology Cottbus - Senftenberg.
- Er-Rbib, H. and C. Bouallou (2014). Modeling and simulation of CO methanation process for renewable electricity storage. *Energy* 75, pp. 81–88. DOI: 10.1016/j.energy.2014.05.115.
- Rhein, S., T. Utz and K. Graichen (2014). Ertragsmaximierung eines katalytischen Festbettreaktors mit Hilfe eines modellprädiktiven Reglers und Zustandsschätzers. *Automatisierungstechnik* 62(2), pp. 92–103. DOI: 10.1515/auto-2014-1017.
- Rönsch, S., J. Köchermann, J. Schneider and S. Matthischke (2016a). Global reaction kinetics of CO and CO₂ methanation for dynamic process modeling. *Chemical Engineering & Technology* 39(2), pp. 208–218. DOI: 10.1002/ceat.201500327.
- Rönsch, S., S. Matthischke, M. Müller and P. Eichler (2014). Dynamische Simulation von Reaktoren zur Festbettmethanisierung. *Chemie Ingenieur Technik* 86(8), pp. 1198–1204. DOI: 10.1002/cite.201300046.

- Rönsch, S. and A. Ortwein (2011). Methanisierung von Synthesegasen – Grundlagen und Verfahrensentwicklungen. *Chemie Ingenieur Technik* 83(8), pp. 1200–1208. DOI: 10.1002/cite.201100013.
- Rönsch, S., A. Ortwein and S. Dietrich (2017). Start-and-stop operation of fixed-bed methanation reactors – Results from modeling and simulation. *Chemical Engineering & Technology* 40(12), pp. 2314–2321. DOI: 10.1002/ceat.201700229.
- Rönsch, S., J. Schneider, S. Matthischke, M. Schlüter, M. Götz, J. Lefebvre, P. Prabhakaran and S. Bajohr (2016b). Review on methanation – From fundamentals to current projects. *Fuel* 166, pp. 276–296. DOI: 10.1016/j.fuel.2015.10.111.
- Rovinsky, A. B. and M. Menzinger (1992). Chemical instability induced by a differential flow. *Physical Review Letters* 69(8), pp. 1193–1196. DOI: 10.1103/PhysRevLett.69.1193.
- Sabatier, P. and J.-B. Senderens (1902a). Hydrogenation of CO over nickel to produce methane. *Journal of the Society of Chemical Industry* 21, p. 504.
- Sabatier, P. and J.-B. Senderens (1902b). Nouvelles synthèses du méthane. *Comptes Rendus de l'Académie des Sciences* 134. Series IIC – Chemistry, pp. 514–516.
- Sahebdehfar, S. and M. T. Ravanchi (2015). Carbon dioxide utilization for methane production: A thermodynamic analysis. *Journal of Petroleum Science and Engineering* 134, pp. 14–22. DOI: 10.1016/j.petro1.2015.07.015.
- Schaaf, T., J. Grünig, M. R. Schuster, T. Rothenfluh and A. Orth (2014). Methanation of CO₂ – storage of renewable energy in a gas distribution system. *Energy, Sustainability and Society* 4(1), pp. 2–14. DOI: 10.1186/s13705-014-0029-1.
- Schiebahn, S., T. Grube, M. Robinius, V. Tietze, B. Kumar and D. Stolten (2015). Power to gas: Technological overview, systems analysis and economic assessment for a case study in Germany. *International Journal of Hydrogen Energy* 40(12), pp. 4285–4294. DOI: 10.1016/j.ijhydene.2015.01.123.
- Schiesser, W. E. (1991). *The Numerical Method of Lines*. Academic Press.
- Schildhauer, T. J. and S. M. A. Biollaz (2015). Reactors for catalytic methanation in the conversion of biomass to synthetic natural gas (SNG). *Chimia* 69(10), pp. 603–607. DOI: 10.2533/chimia.2015.603.
- Schildhauer, T. J. and S. M. A. Biollaz (2016). Fluidized bed methanation for SNG production – process development at the Paul-Scherrer Institute. *Synthetic Natural Gas from Coal, Dry Biomass, and Power-to-Gas Applications*. Ed. by T. J. Schildhauer and

-
- S. M. A. Biollaz. Wiley-Blackwell. Chap. 8, pp. 221–230. DOI: 10.1002/9781119191339.ch8.
- Schlereth, D. and O. Hinrichsen (2014). A fixed-bed reactor modeling study on the methanation of CO₂. *Chemical Engineering Research and Design* 92(4), pp. 702–712. DOI: 10.1016/j.cherd.2013.11.014.
- Schlüter, M., M. Albrecht, M. Sündermann and S. Rönsch (2017). Low temperature CO-methanation in oil-tempered plate reactors by the optimization of catalyst activation conditions. *Chemical Engineering & Technology* 40(9), pp. 1685–1692. DOI: 10.1002/ceat.201600440.
- Schmidt, M., S. Schwarz, B. Stürmer, L. Wagener and U. Zuberbühler (2018). Technologiebericht 4.2a Power-to-gas (Methanisierung chemisch-katalytisch). Tech. rep. Wuppertal Institut, ISI, IZES.
- Schollenberger, D., S. Bajohr, M. Gruber, R. Reimert and T. Kolb (2018). Scale-up of innovative honeycomb reactors for power-to-gas applications – The project Store&Go. *Chemie Ingenieur Technik* 90(5), pp. 696–702. DOI: 10.1002/cite.201700139.
- Schöß, M. A., A. Redenius, T. Turek and R. Güttel (2014). Chemische Speicherung regenerativer elektrischer Energie durch Methanisierung von Prozessgasen aus der Stahlindustrie. *Chemie Ingenieur Technik* 86(5), pp. 734–739. DOI: 10.1002/cite.201300086.
- Shahrokhi, M. and G. R. Baghmisheh (2005). Modeling, simulation and control of a methanol synthesis fixed-bed reactor. *Chemical Engineering Science* 60(15), pp. 4275–4286. DOI: 10.1016/j.ces.2004.12.051.
- Sheintuch, M. and O. Nekhamkina (2004). Comparison of flow-reversal, internal-recirculation and loop reactors. *Chemical Engineering Science* 59(19), pp. 4065–4072. DOI: 10.1016/j.ces.2004.04.037.
- El-Sibai, A., L. Rihko-Struckmann and K. Sundmacher (2015). Synthetic methane from CO₂: Dynamic optimization of the Sabatier process for power-to-gas applications. *Computer Aided Chemical Engineering* 37. 12th International Symposium on Process System Engineering (PSE) and 25th European Symposium on Computer Aided Process Engineering (ESCAPE), pp. 1157–1162. DOI: 10.1016/B978-0-444-63577-8.50038-3.
- El-Sibai, A., L. K. Rihko-Struckmann and K. Sundmacher (2017). Model-based optimal Sabatier reactor design for power-to-gas applications. *Energy Technology* 5(6), pp. 911–921. DOI: 10.1002/ente.201600600.
- Specht, M., J. Brellocks, V. Frick, B. Stürmer and U. Zuberbühler (2016). Synthetic Natural Gas from Coal, Dry Biomass, and Power-to-Gas Applications. *Synthetic Natural Gas from*

- Coal, Dry Biomass, and Power-to-Gas Applications*. Ed. by T. J. Schildhauer and S. M. A. Biollaz. Wiley-Blackwell. Chap. 7, pp. 191–220. DOI: 10.1002/9781119191339.ch8.
- Stankiewicz, A. I. and M. Kuczynski (1995). An industrial view on the dynamic operation of chemical converters. *Chemical Engineering and Processing: Process Intensification* 34(4), pp. 367–377. DOI: 10.1016/0255-2701(95)00537-4.
- Sterner, M. and I. Stadler (2017). *Energiespeicher – Bedarf, Technologien, Integration*. 2nd edition. Springer Vieweg. DOI: 10.1007/978-3-662-48893-5.
- Stuchly, V. and K. Klusacek (1993). Unsteady-state carbon monoxide methanation on an Ni/SiO₂ catalyst. *Journal of Catalysis* 139(1), pp. 62–71. DOI: 10.1006/jcat.1993.1007.
- Su, X., J. Xu, B. Liang, H. Duan, B. Hou and Y. Huang (2016). Catalytic carbon dioxide hydrogenation to methane: A review of recent studies. *Journal of Energy Chemistry* 25(4), pp. 553–565. DOI: 10.1016/j.jechem.2016.03.009.
- Sun, D., F. M. Khan and D. S. A. Simakov (2017a). Heat removal and catalyst deactivation in a Sabatier reactor for chemical fixation of CO₂: Simulation-based analysis. *Chemical Engineering Journal* 329. XXII International conference on Chemical Reactors (CHEMREACTOR-22), pp. 165–177. DOI: 10.1016/j.cej.2017.06.160.
- Sun, D. and D. S. A. Simakov (2017b). Thermal management of a Sabatier reactor for CO₂ conversion into CH₄: Simulation-based analysis. *Journal of CO₂ Utilization* 21, pp. 368–382. DOI: 10.1016/j.jcou.2017.07.015.
- Tallmadge, J. A. (1970). Packed bed pressure drop – an extension to higher Reynolds numbers. *AIChE Journal* 16(6), pp. 1092–1093. DOI: 10.1002/aic.690160639.
- Thema, M., M. Sterner, T. Lenck and P. Götz (2016). Necessity and impact of power-to-gas on energy transition in Germany. *Energy Procedia* 99. 10th International Renewable Energy Storage Conference (IRES), pp. 392–400. DOI: 10.1016/j.egypro.2016.10.129.
- Tonkovich, A. Y., S. Perry, Y. Wang, D. Qiu, T. LaPlante and W. A. Rogers (2004). Microchannel process technology for compact methane steam reforming. *Chemical Engineering Science* 59(22). ISCRE18, pp. 4819–4824. DOI: 10.1016/j.ces.2004.07.098.
- Toro, E. F. (2009). *Riemann Solvers and Numerical Methods for Fluid Dynamics: A Practical Introduction*. 3rd edition. Springer.
- Try, R., A. Bengaouer, P. Baurens and C. Jallut (2018). Dynamic modeling and simulations of the behavior of a fixed-bed reactor-exchanger used for CO₂ methanation. *AIChE Journal* 64(2), pp. 468–480. DOI: 10.1002/aic.15874.

-
- Türks, D., H. Mena, U. Armbruster and A. Martin (2017). Methanation of CO₂ on Ni/Al₂O₃ in a structured fixed-bed reactor – A scale-up study. *Catalysts* 7(5), p. 152. DOI: 10.3390/catal7050152.
- Ulleberg, Ø., T. Nakken and A. Eté (2010). The wind/hydrogen demonstration system at Utsira in Norway: Evaluation of system performance using operational data and updated hydrogen energy system modeling tools. *International Journal of Hydrogen Energy* 35(5), pp. 1841–1852. DOI: 10.1016/j.ijhydene.2009.10.077.
- United Nations (2016). Paris Agreement. Convention on Climate Change.
- Vance, C. K. and C. H. Bartholomew (1983). Hydrogenation of carbon dioxide on group viii metals: III, Effects of support on activity/selectivity and adsorption properties of nickel. *Applied Catalysis* 7(2), pp. 169–177. DOI: 10.1016/0166-9834(83)80005-0.
- Vande Wouwer, A., P. Saucez and W. E. Schiesser (2004). Simulation of distributed parameter systems using a Matlab-based method of lines toolbox: Chemical engineering applications. *Industrial & Engineering Chemistry Research* 43(14), pp. 3469–3477. DOI: 10.1021/ie0302894.
- Vande Wouwer, A., P. Saucez, W. E. Schiesser and S. Thompson (2005). A MATLAB implementation of upwind finite differences and adaptive grids in the method of lines. *Journal of Computational and Applied Mathematics* 183(2), pp. 245–258. DOI: 10.1016/j.cam.2004.12.030.
- Vannice, M. A. (1976). The catalytic synthesis of hydrocarbons from carbon monoxide and hydrogen. *Catalysis Reviews* 14(1), pp. 153–191. DOI: 10.1080/03602457608073410.
- Vázquez, F. V., J. Kihlman, A. Mylvaganam, P. Simell, M.-L. Koskinen-Soivi and V. Alopaeus (2018). Modeling of nickel-based hydrotalcite catalyst coated on heat exchanger reactors for CO₂ methanation. *Chemical Engineering Journal* 349, pp. 694–707. DOI: 10.1016/j.cej.2018.05.119.
- Verein Deutscher Ingenieure (2006). VDI-Wärmeatlas. Ed. by H. Martin, V. Gnielinski, S. Kabelac, M. Kind, D. Mewes, K. Schaber and P. Stephan. 10th edition. Springer-Verlag. DOI: 10.1007/978-3-642-19981-3.
- Watson, G. H. (1980). Methanation Catalysts. IEA Coal Research.
- Weatherbee, G. D. and C. H. Bartholomew (1981). Hydrogenation of CO₂ on group VIII metals: I. Specific activity of Ni/SiO₂. *Journal of Catalysis* 68(1), pp. 67–76. DOI: 10.1016/0021-9517(81)90040-3.

- Weatherbee, G. D. and C. H. Bartholomew (1982). Hydrogenation of CO₂ on group VIII metals: II. Kinetics and mechanism of CO₂ hydrogenation on nickel. *Journal of Catalysis* 77(2), pp. 460–472. DOI: 10.1016/0021-9517(82)90186-5.
- Weatherbee, G. D. and C. H. Bartholomew (1984). Hydrogenation of CO₂ on group VIII metals: IV. Specific activities and selectivities of silica-supported Co, Fe, and Ru. *Journal of Catalysis* 87(2), pp. 352–362. DOI: 10.1016/0021-9517(84)90196-9.
- Wehinger, G. D., F. Klippel and M. Kraume (2017a). Modeling pore processes for particle-resolved CFD simulations of catalytic fixed-bed reactors. *Computers & Chemical Engineering* 101, pp. 11–22. DOI: 10.1016/j.compchemeng.2017.02.029.
- Wehinger, G. D. and M. Kraume (2017b). CFD als Designtool für Festbettreaktoren mit kleinem Rohr-zu-Pelletdurchmesser-Verhältnis: Heute oder in Zukunft? *Chemie Ingenieur Technik* 89(4), pp. 447–453. DOI: 10.1002/cite.201600155.
- Weisz, P. B. and C. D. Prater (1954). Interpretation of measurements in experimental catalysis. *Advances in Catalysis*. Advances in Catalysis 6, pp. 143–196. DOI: 10.1016/S0360-0564(08)60390-9.
- Wesenberg, M. H. and H. F. Svendsen (2007). Mass and heat transfer limitations in a heterogeneous model of a gas-heated steam reformer. *Industrial & Engineering Chemistry Research* 46(3), pp. 667–676. DOI: 10.1021/ie060324h.
- Westermann, A., B. Azambre, M. C. Bacariza, I. Graça, M. F. Ribeiro, J. M. Lopes and C. Henriques (2015). Insight into CO₂ methanation mechanism over NiUSY zeolites: An operando IR study. *Applied Catalysis B: Environmental* 174–175, pp. 120–125. DOI: 10.1016/j.apcatb.2015.02.026.
- Xu, J. and G. F. Froment (1989a). Methane steam reforming, methanation and water-gas shift: I. Intrinsic kinetics. *AIChE Journal* 35(1), pp. 88–96. DOI: 10.1002/aic.690350109.
- Xu, J. and G. F. Froment (1989b). Methane steam reforming: II. Diffusional limitations and reactor simulation. *AIChE Journal* 35(1), pp. 97–103. DOI: 10.1002/aic.690350110.
- Yakhnin, V. and M. Menzinger (2004). High-temperature transients in catalytic fixed-bed reactors. *Reviews in Chemical Engineering* 20(3–4), pp. 175–224. DOI: 10.1515/REVCE.2004.20.3-4.175.
- Yakhnin, V., S. Rattanayotsakun, A. Jaree and M. Menzinger (2015). The parameter domain of convective instability of the adiabatic packed-bed reactor. *The Canadian Journal of Chemical Engineering* 93(11), pp. 1975–1989. DOI: 10.1002/cjce.22296.

-
- Yakhnin, V., A. B. Rovinsky and M. Menzinger (1995a). Absolute instability of a tubular packed-bed reactor with recycling. *Chemical Engineering Science* 50(10), pp. 1591–1593. DOI: 10.1016/0009-2509(95)00007-R.
- Yakhnin, V., A. B. Rovinsky and M. Menzinger (1995b). Convective instability induced by differential transport in the tubular packed-bed reactor. *Chemical Engineering Science* 50(18), pp. 2853–2859. DOI: 10.1016/0009-2509(95)00114-K.
- Zapf, M. (2017). Stromspeicher und Power-to-Gas im deutschen Energiesystem – Rahmenbedingungen, Bedarf und Einsatzmöglichkeiten. Springer Vieweg. DOI: 10.1007/978-3-658-15073-0.
- Zhang, J., N. Fatah, S. Capela, Y. Kara, O. Guerrini and A. Y. Khodakov (2013). Kinetic investigation of carbon monoxide hydrogenation under realistic conditions of methanation of biomass derived syngas. *Fuel* 111, pp. 845–854. DOI: 10.1016/j.fuel.2013.04.057.
- Zhilyaeva, N. A., E. A. Volnina, M. A. Kukina and V. M. Frolov (2002). Carbon dioxide hydrogenation catalysts (a review). *Petroleum Chemistry* 42(6), pp. 367–386.

List of publications

Peer-reviewed articles

Matthischke, S., S. Rönsch and R. Güttel (2019). Transient flow rate ramps for methanation of carbon dioxide in an adiabatic fixed-bed recycle reactor. submitted.

Matthischke, S., S. Roensch and R. Güttel (2018). Start-up time and load range for the methanation of carbon dioxide in a fixed-bed recycle reactor. *Industrial & Engineering Chemistry Research* 57(18), pp. 6391–6400.

Matthischke, S., R. Krüger, S. Rönsch and R. Güttel (2016). Unsteady-state methanation of carbon dioxide in a fixed-bed recycle reactor – Experimental results for transient flow rate ramps. *Fuel Processing Technology* 153, pp. 87–93.

Rönsch, S., J. Schneider, S. Matthischke, M. Schlüter, M. Götz, J. Lefebvre, P. Prabhakaran and S. Bajohr (2016). Review on methanation – From fundamentals to current projects. *Fuel* 166, pp. 276–296.

Rönsch, S., J. Köchermann, J. Schneider and S. Matthischke (2016). Global reaction kinetics of CO and CO₂ methanation for dynamic process modeling. *Chemical Engineering & Technology* 39(2), pp. 208–218.

Köchermann, J., J. Schneider, S. Matthischke and S. Rönsch (2015). Sorptive H₂S removal by impregnated activated carbons for the production of SNG. *Fuel Processing Technology* 138, pp. 37–41.

Rönsch, S., S. Matthischke, M. Müller and P. Eichler (2014). Dynamische Simulation von Reaktoren zur Festbettmethanisierung. *Chemie Ingenieur Technik* 86(8), pp. 1198–1204.

Oral presentations

Matthischke, S., S. Rönsch and R. Güttel (2018). The recirculation of product gas to enhance the unsteady operation window of fixed-bed reactors. Jahrestreffen der ProcessNet Fachgruppe Reaktionstechnik, Würzburg.

Matthischke, S., S. Rönsch and R. Güttel (2015). Instationärer Betrieb der Methanisierung in Festbettreaktoren. Jahrestreffen der ProcessNet Fachgruppe Energieverfahrenstechnik, Bonn.

Rönsch, S., S. Dietrich and S. Matthischke (2015). Festbettmethanisierung – Simulation und Versuche zum lastflexiblen Verhalten. Jahrestreffen der ProcessNet Fachgruppe Hochtemperaturtechnik, Rheinfelden.

Matthischke, S., S. Rönsch (2013). Dynamic simulation of fixed-bed methanation for SNG production. 4th International Conference on Polygeneration Strategies, Vienna/ Austria.

Rönsch, S., S. Matthischke (2013). Dynamische Simulation von Reaktoren zur Festbettmethanisierung. Jahrestreffen der ProcessNet Fachgruppe Energieverfahrenstechnik, Würzburg.

Poster presentations

Matthischke, S., S. Rönsch and R. Güttel (2018). Power-to-Methan: Lastflexibilität und Reaktordesign von Festbettreaktoren für den instationären Betrieb. Jahrestreffen der ProcessNet Fachgruppe Energieverfahrenstechnik, Frankfurt a.M.

Matthischke, S., S. Rönsch and R. Güttel (2015). Modelling and simulation of unsteady-state operation of the methanation reaction in fixed-bed reactors. European Symposium on Chemical Reaction Engineering (ESCRE), Fürstfeldbruck.

Matthischke, S., S. Rönsch (2014). Lastflexibilität der Festbettmethanisierung zur kombinierten SNG-Produktion. DGMK-Fachbereichstagung ‘Konversion von Biomasse’, Rothenburg an der Fulda.

Matthischke, S., S. Rönsch (2014). Notwendigkeit der Methanisierungskinetik von Kohlenstoffmonoxid. Jahrestreffen der ProcessNet Fachgruppe Reaktionstechnik, Würzburg.

Schneider, J., S. Matthischke, D. Hirsch, U. Trommler, S. Rönsch, S. (2013). Charakterisierung von Katalysatoren für die Umwandlung von Synthesegas aus Biomasse in Methan. Jahrestreffen der ProcessNet Fachgruppe Reaktionstechnik, Würzburg.

Aiouache, F., S. Matthischke, K. Chen (2012). Enhancing biomass gasification properties using embedded waste water derived catalysts. World Bioenergy Conference and World Pellets, Jönköping/ Sweden.

Book chapters and monographies

Ortwein, A., A. Krautz, N. Szarka, J. Braun, M. Dotzauer, K. Wurdinger, S. Rönsch, S. Matthischke, V. Lenz, M. Trommler, J. Postel, F. Jacobi (2014). Kurzstudie zum Einsatz von Biomasse zur bedarfsgerechten Energieerzeugung. Fachagentur Nachwachsende Rohstoffe e. V. (FNR), Gülzow-Prüzen, ISBN 978-3-942147-16-3.

Copyright notice

Parts of this thesis were published already in peer-reviewed articles:

1. Sections 3.1, 3.2, 3.3, 5.1, 5.2.1, and 5.3.1, which partly comprise additional passages in the text in this thesis, in Matthischke, S., S. Roensch and R. Güttel (2018). Start-up time and load range for the methanation of carbon dioxide in a fixed-bed recycle reactor. *Industrial & Engineering Chemistry Research* 57(18), pp. 6391–6400.
2. Sections 6.1.1, 6.2.1, and the first half of 6.2.2 in Matthischke, S., R. Krüger, S. Rönsch and R. Güttel (2016). Unsteady-state methanation of carbon dioxide in a fixed-bed recycle reactor – Experimental results for transient flow rate ramps. *Fuel Processing Technology* 153, pp. 87–93.